SCUOLA DI DOTTORATO
UNIVERSITÀ DEGLI STUDI DI MILANO-BICOCCA

Dipartimento di / Department of

Fisica “Giuseppe Occhialini”

Dottorato di Ricerca in / PhD program Physics and Astronomy Ciclo / Cycle XXXVI

Curriculum in (se presente / if it is) _____

MORPHOLOGY AND KINEMATICS OF COSMIC WEB FILAMENTS

Cognome / Surname de Beer Nome / Name Stephanie

Matricola / Registration number 868732

Tutore / Tutor: Monica Colpi

Cotutore / Co-tutor: _____
(se presente / if there is one)

Supervisor: Sebastiano Cantalupo
(se presente / if there is one)

Coordinatore / Coordinator: Stefano Ragazzi

ANNO ACCADEMICO / ACADEMIC YEAR 2022/2023

Summary

Due to the web-like distribution of matter in the Universe predicted by the standard theory of structure formation, haloes and the galaxies they host are expected to be embedded in diffuse gas structures which constitute the circumgalactic medium (CGM) and intergalactic medium (IGM). The characterisation of this gas is an important step in understanding the formation and evolution of galaxies, as it is this accreting gas which provides the fuel for star formation activity in the galaxies. While these gaseous structures have been studied extensively with pencil beam absorption studies, their diffuse nature severely hampers their detection as extended emission and thus the characterisation of their large scale properties. The almost ubiquitous detection of Lyα emission from the CGM and IGM of bright quasars at $z > 2$ provides the opportunity to directly study the physical characteristics of the gas through the emission powered by ionising radiation from the quasars. However, this is contingent upon knowledge of the quasar halo host mass. Unfortunately, existing constraints on quasar host halo masses from clustering studies, exhibit significant discrepancies around redshift $z \sim 3$, where the majority of Lyα nebulae have been observed.

In the first part of this research, I introduce a novel method to constrain quasar halo masses by analyzing the line-of-sight velocity dispersion maps of Lyα nebulae. Using MUSE-like mock observations from cosmological hydrodynamic simulations, I demonstrate that the kinematics of the Lyα emitting gas is dominated by the gravitational potential of the host halo and that the velocity dispersion profiles of Lyα emitting gas exhibit self-similarity with respect to halo mass when appropriately rescaled by the virial radius of their host haloes. I further show that radiative transfer effects do not alter the shape but only the normalization of these profiles. Applying this method to 37 observed quasar Lyα nebulae at $3 < z < 4.7$, I find that associated quasars are typically hosted by $\sim 10^{12.16\pm0.14}\mathrm{M}_{\odot}$ haloes, independent of redshift, aligning with clustering and cross-correlation results.

In the second part, I extend the analysis by comparing the surface brightness values of the 37 Lyα nebulae to mock observations generated from cosmological simulations under the assumption of maximal fluorescence. Confining the simulated nebulae to the specific halo mass range derived from the Lyα kinematics in the first part, I constrain the density of Lyα emitting gas. The analysis reveals that the cold CGM must reach densities of 1 - 10 cm^{-3} with a broad distribution to explain observed surface brightness values. I propose mechanisms, including compressive flows, Kelvin Helmholtz instabilities, and turbulence-induced thermal instabilities, to account for the formation of cold, high-density clouds. While theoretical con-

sideration imply that the surface brightness values of the nebulae should increase with redshift, I show that the observed surface brightness values in fact exhibit no discernible redshift evolution. This implies an increase in the width the cold gas's density distribution with time. As turbulence is a potential driver of the broadness of the density distribution, this suggests an enhancement of the turbulence in the cold CGM of bright quasars from $z \sim 4$ to $z \sim 3$.

Sommario

La teoria standard della formazione delle strutture cosmiche, prevede che le galassie e gli aloni che le ospitano siano distribuiti in strutture a rete di gas diffuso che costituiscono il mezzo circumgalattico (CGM) e intergalattico (IGM). Questo gas, accrescendo sulle galassie, alimenta la formazione stellare e, pertanto, la sua caratterizzazione è fondamentale al fine di comprendere la formazione ed evoluzione delle galassie. La rilevazione dell'emissione estesa da parte di queste strutture di gas è estremamente difficile per via della loro natura diffusa, pertanto, la caratterizzazione delle loro proprietà su larga scala avviene principalmente attraverso studi in assorbimento. La radiazione ionizzante in prossimità di quasars brillanti a $z > 2$ alimenta l'emissione in riga Lyα da parte del CGM/IGM, permettendo così di studiare le caratteristiche fisiche di questo gas in maniera diretta. Tuttavia, è necessaria la conoscenza della massa dell'alone che ospita il quasar. Sfortunatamente, le stime esistenti sulle masse degli aloni ospiti di quasars derivanti da studi di clustering, mostrano discrepanze significative attorno a $z \sim 3$ dove sono state osservate la maggior parte delle nebule Lyα.

Nella prima parte di questa ricerca, introduco un metodo innovativo per stimare le masse degli aloni dall'analisi delle mappe di dispersione di velocità lungo la linea di vista delle nebule Lyα. Utilizzando osservazioni MUSE simulate ottenute da simulazioni cosmologiche idrodinamiche, mostro come la cinematica del gas che emette Lyα è dominata dal potenziale gravitazionale dell'alone e che la velocità di dispersione del gas, riscalata opportunamente per il raggio viriale dell'alone, mostra un auto-similarità rispetto alla massa dell'alone. Inoltre, mostro come gli effetti di trasporto radiativo non alterano la forma dei profili di dispersione di velocità ma solo la loro normalizzazione. Applicando questo metodo a 37 osservazioni di nebule Lyα a $3 < z < 4.7$, trovo che i quasars sono tipicamente ospitati in aloni di massa $\sim 10^{12.16 \pm 0.14} \mathrm{M}_{\odot}$, indipendentemente dal redshift, in accordo con i risultati provenienti da studi di clustering e di correlazione incrociata.

Nella seconda parte della ricerca, estendo l'analisi confrontando i valori di brillanza superficiale delle 37 nebule Lyα con osservazioni simulate ottenute da simulazioni cosmologiche nell'assunzione di massima fluorescenza. Limitando le nebule simulate nell'intervallo di masse derivato nella prima parte attraverso la cinematica del gas, pongo dei vincoli sulla densità del gas che emette Lyα. Quest'analisi rivela che per spiegare i valori osservati di brillanza superficiale della Lyα, il CGM freddo deve raggiungere densità dell'ordine di 1 - 10 cm^{-3} ed avere una distribuzione larga. Fra i meccanismi responsabili per la formazione di nubi fredde ad alta densità propongo la presenza di flussi compressivi, instabilità di Kelvin-Helmholtz e instabilità termi-

che indotte dalla turbolenza. A differenza di ciò che è predetto da considerazioni di tipo teorico riguardo ad un aumento della brillanza superficiale con il redshift, mostro come essa, invece, non mostri una tale evoluzione. Questo risultato suggerisce quindi un aumento in funzione del tempo cosmico della larghezza della distribuzione del gas freddo. Dato che la turbolenza è un potenziale fattore determinante della larghezza della distribuzione di densità del gas, questo risultato suggerisce un aumento della turbolenza della fase fredda del CGM nei quasar brillanti da $z \sim 4$ a $z \sim 3$.

Contents

List of Figures

List of Tables

Chapter 1

Introduction

The baryonic and dark matter in our Universe is distributed in a web-like pattern. Some of the first observational evidence for this was based on galaxy catalogues constructed from redshift surveys and dates as far back as the 1960s. For instance, plotting the distribution of the galaxies surveyed in Zwicky et al. (1961) reveals that the galaxies are clustered and form a web-like structure. Subsequent redshift surveys, which have extended the resulting galaxy catalogues to both fainter magnitudes and higher redshifts, have further confirmed that the galaxies are indeed arranged in a web-like manner (de Lapparent et al. 1986; York et al. 2000; Jones et al. 2004; Cole et al. 2005; Peacock et al. 2001; Scoville et al. 2007; Driver et al. 2011; Huchra et al. 2012; Guzzo et al. 2014). The underlying cause of this distribution is the theorised anisotropic gravitational collapse in the early Universe of both gas and dark matter into intersecting sheets and filaments (Zeldovich et al. 1982), which constitute the so-called Cosmic Web (Bond et al. 1996). The filamentary distribution of both gas and dark matter is further corroborated by cosmological N-body simulations (e.g., Navarro et al. 1996; Tormen et al. 1997; Jenkins et al. 1998; Springel 2005), with galaxies and the virialised dark matter haloes in which they form located in the densest regions of the cosmic web, the nodes where filaments and sheets intersect (Rees & Ostriker 1977; Silk 1977; White & Frenk 1991).

Based on the aforementioned numerical simulations, dark matter and gas are thought to continually accrete along the cosmic filaments and sheets towards the nodes of the Cosmic Web under the influence of gravity. Although ram pressure stripped gas from satellite galaxies has also been shown to be a relevant source of gas accretion (Gunn & Gott 1972; Grcevich & Putman 2009; Putman et al. 2021), it is predicted that gas accretion from the Cosmic Web is the dominant accretion mechanism (Kereš et al. 2005; Brooks et al. 2009; Joung et al. 2012b). Far away from the haloes, in the inter galactic medium (IGM), the diffuse gas in the Cosmic Web remains cold, sitting at a temperatures of $\sim 10^4$ K. As it accretes along the filaments into the haloes it experiences shock heating, resulting in its temperature rising to the virial temperatures of the respective haloes. For haloes with masses of $10^{12}\mathrm{M}_\odot$ and higher this means the accreted gas reaches temperatures as high as 10^6 K (Birnboim & Dekel 2003). For that gas to then fuel star formation in the central galaxy, it needs to cool back down to temperatures below 10^4 K, as well as accrete

onto the central galaxy. The way in which the gas reaches the central galaxy is not yet well understood due to a lack of direct observations and a lack of resolution in simulations, but there is evidence that density fluctuations and turbulence can lead to the condensation of cool gas clouds which then subsequently rain down on the galaxy. At higher redshift ($z > 2$) the picture is slightly different due to the higher density contrast between the Cosmic Web filaments and the surrounding medium. The higher density of the filaments prevents the shock heating of the accreting gas, allowing it to remain cold ($< 10^5$ K) and relatively dense (Kereš et al. 2005; Dekel & Birnboim 2006; Agertz et al. 2009; Dekel et al. 2009; Kereš et al. 2009). Thus even massive haloes ($\sim 10^{12}$M$_\odot$) are supplied with cold gas capable of fuelling star formation. Another effect of the gas remaining cold, is that the halo remains embedded in and connected to the cold, diffuse Cosmic Web filaments.

Despite these well motivated theoretical predictions, there is still no direct observational evidence of gas accretion from the Cosmic Web. This is predominantly due to its diffuse nature, which makes in extremely hard to detect. One piece of indirect evidence for the continual accretion of gas into haloes and the galaxies they host are the observed star formation rates of the galaxies themselves. The resultant depletion times of galaxies are typically on scales shorter than Gyrs (Daddi et al. 2010; Genzel et al. 2010; Schiminovich et al. 2010; Bigiel et al. 2011; Tacconi et al. 2013; Leroy et al. 2013). Hence, if the galaxies were not continuously being supplied with more gas, they would quench on timescales comparable to their depletion times. These comparatively short quenching times, with regard to the Hubble time, would result in the majority of galaxies observed being quenched, in contrast to the observed quenched fractions (Kauffmann et al. 2003; Baldry et al. 2004; Arnouts et al. 2007; Drory et al. 2009).

Setting aside the kinematics of the gas in the Cosmic Web, the presence of diffuse, cold and neutral gas distributed throughout the IGM, as well as in the immediate vicinity of haloes and galaxies is well established observationally. The so-called Lyα forest constitutes some of the first observational evidence of the presence of gas clouds in the IGM. Despite the onset of reionisation at $z > 6$, the diffuse gas in the Cosmic Web has remained mostly neutral and is therefore expected to leave absorption features in the spectra of background emitters. These features arise due to the absorption of photons emitted bluewards of the resonant Lyα line of the background object by the primordial Hydrogen in the Cosmic Web. Multiple efforts to detect these absorption features in the spectra of background galaxies failed as the emission from the galaxies was not sufficiently bright and the observations not sufficiently sensitive (e.g., Field 1959). However, with the discovery of the first quasar this limitation was overcome. Spectroscopic observations of numerous high redshift quasars revealed discrete Lyα absorption lines as well as higher order Lyman lines confirming that low metallicity, neutral gas structures, e.g., primordial gas, is indeed responsible for the absorption features (Bahcall & Salpeter 1965; Gunn & Peterson 1965; Baldwin et al. 1974; Carswell et al. 1975; Coleman et al. 1976; Young et al. 1982). Finally, by analysing the spatial clustering of the absorbers Sargent et al. (1980) were able to show that the most likely source of this "forest" of Lyα lines, i.e., the Lyα forest, is diffuse, intergalactic gas.

In addition to passing through the IGM, quasar sightlines can also pass through haloes hosting other galaxies between them and the observer. They can thus be used to probe the cirmcumgalactic medium (CGM) of the foreground galaxy. These quasar sightlines have become the standard method with which the CGM is probed in absorption and have revealed a continuous distribution of gas from the Cosmic Web in the IGM all the way to the immediate vicinity of galaxies, namely their CGM (Penton et al. 2002; Wakker & Savage 2009; Prochaska et al. 2011; Tumlinson et al. 2013). By fitting the absorption lines with Voigt profiles, it is possible to obtain constraints on the temperature, column density and redshift of the detected absorbers. Thus through large surveys and careful analysis, it is now widely accepted that the CGM of most galaxies at all redshifts contains multiple, highly complex gas phases (Hennawi et al. 2006; Rubin et al. 2010; Steidel et al. 2010; Tripp et al. 2011). The ample detection of Lyα absorbers in the CGM provides evidence for cool, diffuse gas which could have accreted from the Cosmic Web (Rudie et al. 2012). Detections of low-ionisation state absorbers which trace cool gas such as, but not limited to, CII, CIII, SiII, SiII, NII and NII absorbers indicate that the cool gas is chemically enriched (Narayanan et al. 2011; Zafar et al. 2013; Crighton et al. 2015a; Dutta et al. 2020). This complicates the picture of accretion from the pristine IGM and suggests the cool CGM may be enriched by processes such as galactic recycling (Tumlinson et al. 2011; Werk et al. 2014) or, as mentioned above, the ram pressure stripping of satellite galaxies. In addition to a cool gas phase, observations of high-ionisation state absorbers indicate the existence of a chemically enriched hot gas phase in the CGM (Howk et al. 2009; Tumlinson et al. 2011; Prochaska et al. 2011; Narayanan et al. 2012; Meiring et al. 2013). The existence of this hot gas is thought to be predominantly due to stellar or AGN feedback and its existence represents strong, indirect evidence of feedback powered outflows (Weiner et al. 2009; Lehner et al. 2009; Tripp et al. 2011; Mathes et al. 2014). Thus the simplified picture that emerges from absorption studies is one where primordial gas from the Cosmic Web continually accretes into the haloes. However, cosmic accretion is not the only source gas in the halo/CGM as stellar and AGN feedback expel chemically enriched gas from the galaxy back into the CGM resulting in a multiphase medium. Considering that an absorption feature in a quasar sightline can necessarily only probe the intervening matter along the line of sight between the observer and the quasar, it is remarkable how much has been deduced about the gas in the Cosmic Web and the CGM from these observations. Although this limitation can partly be mitigated by using lensed background quasars which afford multiple sight lines through one halo's CGM (Smette et al. 1992; Monier et al. 1998; Rauch et al. 2001; Ellison et al. 2004; Zahedy et al. 2016; Rubin et al. 2018) or gravitational arc tomography (Lopez et al. 2018; Mortensen et al. 2021; Tejos et al. 2021; Bordoloi et al. 2022; Fernandez-Figueroa et al. 2022), it is necessary to observe the gas in emission to study its morphology in detail.

The gas in the Cosmic Web is predicted to emit fluorescent Lyα radiation due to ionising radiation from the cosmic UV background (UVB). In detail, the illumination of the Cosmic Web by the UVB is capable of ionising the Hydrogen in the Cosmic Web, which then subsequently recombines and emits Lyα radiation (Hogan

& Weymann 1987; Gould & Weinberg 1996). Despite multiple, deep spectroscopic observations and stacking analyses, there have not yet been any definitive detections of fluorescent Lyα emission from the Cosmic Web in the IGM (Lowenthal et al. 1990; Bunker et al. 1998; Rauch et al. 2008; Gallego et al. 2018; Bacon et al. 2021). However, these non-detections are to be expected due to how faint this emission in the IGM is predicted to be (Cantalupo et al. 2005; Silva et al. 2016; Witstok et al. 2021). On the other hand, Lyα emission from the Cosmic Web closer to its nodes, i.e., from the CGM of galaxies, is brighter due to the higher gas densities closer to the nodes and also due to the added ionising radiation stemming from the central galaxy if it is star-forming or hosts an AGN (Haiman et al. 2000; Haiman & Rees 2001; Fardal et al. 2001; Furlanetto et al. 2003, 2005; Kollmeier et al. 2010; Faucher-Giguère et al. 2010; Rosdahl & Blaizot 2012; Silva et al. 2013). Initially, these predicted "Lyα nebulae" were only observed in large statistical stacks of Narrow-Band images and deep, long slit spectroscopic observations (Yang et al. 2009; Steidel et al. 2011; Hennawi & Prochaska 2013). This situation has dramatically changed due to newer, more sensitive spectrographs such as the Keck Cosmic Web Imager (KCWI) (Martin et al. 2010; Morrissey et al. 2018) and the Multi Unit Spectroscopic Explorer (MUSE) on the ESO Very Large Telescope (VLT) (Bacon et al. 2010). Due to the exquisite sensitivity of these instruments it has become possible to detect emission as faint as 10^{-19} erg s^{-1} cm^{-2} arcsec^{-2} with integration times of less than an hour, thus allowing the almost ubiquitous discovery of Lyα nebulae around star-forming galaxies and AGN at $2 \lesssim z \lesssim 6$, the redshift range probed by the KCWI and MUSE spectrograph (Cantalupo et al. 2012, 2014; Farina et al. 2017; Patrício et al. 2016; Wisotzki et al. 2016; Borisova et al. 2016; Cai et al. 2017; Vanzella et al. 2017; Leclercq et al. 2017; Arrigoni Battaia et al. 2019a; Cantalupo et al. 2019; Drake et al. 2019; Umehata et al. 2019a; Cai et al. 2019; Farina et al. 2019; Mackenzie et al. 2021; Fossati et al. 2021; Chen et al. 2021).

With observations of these Lyα nebulae it is possible obtain constraints on the morphology and kinematics of the cold, emitting CGM in addition to the constraints on the cold CGM's temperature and column density obtained from absorption studies. Additionally, the brightness of the emission from the Lyα nebulae primarily depends on the density of the emitting gas and could thus be used to constrain the cold gas density of the CGM. However, it is not clear that recombination radiation is always the dominant source of Lyα emission in the CGM. In addition to recombination radiation, collisional excitation and the scattering of Lyα photons from the central galaxy or AGN (photon pumping) can contribute to the emission from such Lyα nebulae (Cantalupo 2017). Attempting to disentangle these three emission mechanisms is extremely challenging, partly due to the detailed ionisation state and radiative transfer modelling required, which is hampered by the insufficient resolution of the current simulations. In particular, emission due to collisional excitation is sensitive to the exact neutral fraction of the emitting gas. Photon pumping is also dependent on the neutral fraction as well as being governed by radiative transfer effects. In contrast, recombination radiation depends on the gas's ionised fraction. A model commonly adopted when attempting to understand the ionisation state of emitting gas is that of ionisation equilibrium, where the ionisation

state of the gas is determined by the balance of the incident, ionising radiation, the collisional ionisation rate and the recombination rate of the gas. In scenarios where the incident, ionising radiation is sufficiently bright, the neutral fraction of the gas becomes small enough ($\chi_{HI} \ll 1$) for the emission from recombination radiation to become dominant with regards to the radiation stemming from collisional excitation and photon pumping, thus facilitating the theoretical interpretation of observations. The bright, ionising radiation has the additional effect of boosting emission from the CGM, making it easier to detect. One potential source of such ionising radiation is a UV-bright quasar (Bunker et al. 2003; Cantalupo et al. 2008). Indeed, the majority of extended Lyα nebulae have been detected around quasars due to the aforementioned boost in brightness from the quasar fluorescence, which allows the nebulae to be detected in fairly shallow observations (Cantalupo et al. 2012; Farina et al. 2017; Arrigoni Battaia et al. 2016, 2019a; Drake et al. 2019; Cai et al. 2019; Farina et al. 2019; O'Sullivan et al. 2020; Mackenzie et al. 2021; Fossati et al. 2021; Langen et al. 2023). In some cases, the detected emission extends to scales of hundreds of kpc. Thus it is not simply the CGM that is probed in emission, but the filaments of the Cosmic Web itself (Cantalupo et al. 2014; Borisova et al. 2016; Cai et al. 2018; Cantalupo et al. 2019; Umehata et al. 2019a). First analyses of the kinematics of the Lyα emitting gas through flux weighted first and second moment maps (i.e., the line of sight velocity and velocity dispersion maps) have even supplied tentative evidence of cold gas accreting directly from the Cosmic Web into the CGM of galaxies (Martin et al. 2019; Daddi et al. 2021, 2022).

Despite these exquisite observations, it is still challenging to draw robust conclusions concerning the kinematics of the Lyα emitting gas. This is due to the resonant nature of the Lyα line. On the one hand, it is exactly this resonant nature which causes the emission to be bright enough to be detected almost ubiquitously around quasars. On the other hand, this resonance also broadens the emission line, thus washing out the kinematic information. One way to counteract this difficulty, is to consider the non-resonant emission lines which are also expected to arise due to the recombination of primordial gas, such as the H-Hα and He-Hα lines. However, exactly because these lines are non-resonant their emission is far fainter, thus hampering their detection. It is for this reason, that there are far fewer such detections, although this is rapidly changing with multiple, recent detections (Leibler et al. 2018; Cantalupo et al. 2019; Marino et al. 2019; Fossati et al. 2021; Langen et al. 2023, Travascio et al. in prep.). Comparing the ratios of resonant and non-resonant lines also enables one to obtain tighter constraints on the exact contribution to the Lyα emission from photon pumping. Thus additional observations of this non-resonant emission in the future will provide a clearer picture concerning the kinematics and emission mechanism of the Lyα nebulae. Unfortunately, even if the precise kinematics and emission mechanisms were known, it would still not be possible to derive the precise physical properties of the emitting gas from observations, as they currently still lack the spatial resolution to resolve the individual emitting structures (Crighton et al. 2015a; Arrigoni Battaia et al. 2015). Thus any properties derived are in fact averaged over the spatial resolution elements.

Following this overview of the observational evidence concerning the Cosmic

Web and filamentary accretion from the Cosmic Web into the CGM, it is worth reviewing the theoretical evidence. As already stated above, both analytical considerations and simulations show that the matter in the Universe is distributed in this Cosmic Web, with virialised haloes hosting galaxy sitting at the nodes of the web being continuously fed by dark matter and gas. What is not yet completely clear, is to what extent the Cosmic Web filaments can remain intact within the central galaxy's CGM and what the physical properties of the accreting gas are. As previously stated, simulations predict that at $z > 2$ (the redshift relevant when comparing to observations of the Cosmic Web in emission) a stable shock is prevented from forming even in haloes with masses above $\sim 10^{12}$ $M_{\odot}$, thereby allowing gas from the Cosmic Web filaments to directly accrete into the CGM and onto the central galaxy (Kereš et al. 2005; Dekel & Birnboim 2006; Agertz et al. 2009; Dekel et al. 2009; Kereš et al. 2009). However, these simulations lack the resolution to adequately resolve the CGM, thereby prohibiting robust conclusions as to the physical properties, such as the density, of the accreting gas. Over the past two decades, astonishing strides have been made in simulating galaxies and their large scale environments. Utilising smoothed particle hydrodynamics (SPH) codes such as GADGET (Springel et al. 2001; Springel 2005; Springel et al. 2021) and GIZMO (Hopkins 2013), or moving mesh codes such as AREPO (Springel 2010), cosmological hydrodynamic simulations like OWLS (Schaye et al. 2010), the Illustris Project (Vogelsberger et al. 2014a,b; Genel et al. 2014), the FIRE simulations (Hopkins et al. 2014), the EAGLE simulation suite (Schaye et al. 2015; Crain et al. 2015), MUFASA (Davé et al. 2016), IllustrisTNG (Pillepich et al. 2018) and SIMBA (Davé et al. 2019), to name a few, model the gravitational interactions of dark matter and the hydrodynamic interactions of the gas. Over time they have also come to include progressively more sophisticated subgrid physics recipes. Such subgrid physics implementations are necessary because even the most cutting edge cosmological simulations only reach a mass resolution for the gas and dark matter of a few 10^4 $M_{\odot}$. This corresponds to a resolved length of a few 100 pc. Hence, these simulations are unable to resolve the scales on which, for instance, star formation occurs, a process integral to the evolution of galaxies. The subgrid physics implentations are calibrated on certain observables such as, but not limited to, the galaxy stellar mass function (Schaye et al. 2015) and govern, among other things, star formation, stellar feedback, blackhole accretion, AGN feedback and cosmic rays in the various cosmological simulations.

Despite their limitations, these simulations have been remarkably successful in reproducing observed galaxy populations (e.g., Genel et al. 2018), column densities (e.g., Rahmati et al. 2015) and in providing clues as to how these quantities evolve. One example is the over-cooling problem, where simulations initially over predicted the amount of cool gas in galaxies and their star-formation rates (Navarro & Steinmetz 1997; Pearce et al. 1999; Springel & Hernquist 2002; Saro et al. 2006). This in turn meant that they were unable to reproduce the quenched fraction of the galaxy population at low redshift. These discrepancies ultimately lead to the discovery of the importance of energy injection by feedback processes into both the interstellar medium (ISM) and the CGM (Marri & White 2003; Tang et al. 2009; Ceverino &

Klypin 2009), as well as the important role AGN-feedback (Sijacki et al. 2007; McCarthy et al. 2010, 2011; Teyssier et al. 2011) and mergers (Di Matteo et al. 2005; Pontzen et al. 2017; Davies et al. 2022, 2024) play in quenching the star-formation of galaxies. Slowly but surely, the resolution of these simulations is approaching scales on which the processes governing the physics of the CGM act. Thus, our understanding of the CGM is likely to dramatically shift in the next few years. For instance, there is now tentative evidence, that due to the CGM being unresolved, the amount of cold gas in the CGM at high redshift has been underestimated in previous studies (Hummels et al. 2019; Mandelker et al. 2019b; Corlies et al. 2020; Nelson et al. 2020). Another theoretical approach to understanding the cold CGM as it relates to the Cosmic Web, is to consider high resolution, hydrodynamical simulations of a cold stream in a hot medium (Joung et al. 2012a; Mandelker et al. 2016; Gronke & Oh 2018; Mandelker et al. 2018; Padnos et al. 2018; Mandelker et al. 2019a; Vossberg et al. 2019). While these simulations indicate that Kelvin-Helmholtz instabilities can play a role in the disruption of the filament as it flows through the CGM, they also show that, given a certain diameter, it is very likely that cold, filamentary accretion can reach the central galaxy. They also indicate the potential existence of cold, dense gas clumps linked to filamentary accretion which form due to the interaction between the cold filament and the hot, ambient medium.

Taking the observational and theoretical evidence together, the picture that emerges is the following: There is strong evidence for the presence of cold gas from the Cosmic Web in the CGM of galaxies at $z \gtrsim 2$. However, due to the lack of resolution in observations and simulations, the exact physical properties of the cold gas, such as its density distribution and kinematics, are currently poorly constrained. The aim of this work is place new constraints on the density and kinematics of the gas accreting from the Cosmic Web in the CGM of galaxies hosting UV-bright quasars at $z \gtrsim 3$. Fortuitously, the brightness of the Lyα emission due to recombination radiation depends partly on the square of the cold gas's density along the line of sight. This means that the emission is sensitive to the broadness of the cold gas's density distribution a long the line of sight and within a spatial resolution element or, in other words, the clumpiness of the medium (Cantalupo et al. 2019). Hence, information concerning the density and morphology can be extracted from observed Lyα surface brightness (SB) profiles. This can be done by comparing existing observations of Lyα nebulae associated to bright quasars with mock observations generated from existing cosmological hydrodynamical simulations. Discrepancies between the two can then be used to infer in what way simulations do not capture the physical reality of the CGM, thereby obtaining new constraints on the cold CGM at high redshifts. In order to obtain meaningful constraints on the density of the emitting gas, it is imperative that one compare the observations to simulated Lyα nebulae hosted by haloes of the same mass as those hosting the observed nebulae (e.g. Pezzulli & Cantalupo 2019). The brightness of Lyα nebulae scales with the host halo's mass because more massive haloes have a higher average density and a larger size along the line of sight at a fixed radial distance with respect to smaller haloes. Additionally, the halo mass may affect the temperature of the hot CGM, the halo baryon fraction and cold gas fraction, potentially further affecting the Lyα

SB profiles (Crain et al. 2007; Kulier et al. 2019). Thus, comparing the observations to more or less massive haloes would result in an under- or overestimation of the emitting gas's density. It is therefore necessary to first constrain the masses of the quasar haloes in the observations. The issue is, that at the relevant redshift, quasar auto-correlation measurements and quasar galaxy cross-correlation measurements suggest quasar halo masses anywhere between $10^{12}M_{\odot}$ and $10^{13}M_{\odot}$ (Shen et al. 2007; Trainor & Steidel 2012; Font-Ribera et al. 2013; Eftekharzadeh et al. 2015; García-Vergara et al. 2017; He et al. 2017). For the purpose of constraining the cold gas densities, this mass window is too wide.

The purpose of the RePhyNe project ("Resolving the physics of Quasar Lyα Nebulae"), presented in this work, is to develop and test a new, independent, methodology to constrain quasar halo masses through the kinematics of their Lyα emitting CGM. With this alternative mass estimate in hand, I then provide additional constraints on the density and morphology of the cold gas in the CGM of bright quasars. In Chapter 2 the link between quasar halo mass and kinematics of the Lyα emitting gas is established by showing that the kinematics are dominated by the gravitational potential of the host halo through the use of cosmological hydrodynamical simulations. It is also demonstrated that the velocity dispersion of the Lyα nebulae can be used to trace the kinematics of the emitting gas, despite the resonant nature of the Lyα line. Finally, the new quasar mass estimation method is introduced and applied to the Lyα nebulae presented in Borisova et al. (2016) and Fossati et al. (2021). In Chapter 3, simulated Lyα SB profiles from nebulae hosted by haloes within the mass range obtained in Chapter 2 are compared to observed Lyα SB profiles. From this comparison it is inferred, that the cold CGM is indeed under-resolved in the cosmological simulations. I further show, that the presence of cold, dense gas clouds is required throughout the CGM to explain the observed SB brightness levels. The formation mechanisms of such dense gas clouds and their survivability are also discussed in Chapter 3. Both Chapters 2 and 3 are adapted from soon to be submitted and published works

Chapter 2

Constraining Quasar host halo masses through Circumgalactic Medium kinematics[1]

Summary

Lyα nebulae ubiquitously found around $z > 2$ quasars can supply unique constraints on the properties of the Circumgalactic Medium, such as its density distribution, provided the quasar halo mass is known. We present a new method to constrain quasar halo masses based on the line-of-sight velocity dispersion maps of Lyα nebulae. By using MUSE-like mock observations obtained from cosmological hydrodynamic simulations under the assumption of maximal quasar fluorescence, we show that the velocity dispersion radial profiles of Lyα-emitting gas are strongly determined by gravity and that they are thus self-similar with respect to halo mass when rescaled by the virial radius. Through simple analytical arguments and by exploiting the kinematics of HeII1640Å emission for a set of observed nebulae, we show that Lyα radiative transfer effects plausibly do not change the shape of the velocity dispersion profiles but only their normalisation without breaking their self-similarity. Taking advantage of these results, we define the variable $\eta_{40-100}^{140-200}$ as the ratio of the median velocity dispersion in two specifically selected annuli and derive an analytical relation between $\eta_{40-100}^{140-200}$ and the halo mass which can be directly applied to observations. We apply our method to 37 observed quasar Lyα nebulae at $3 < z < 4.7$ and find that their associated quasars are typically hosted by $\sim 10^{12.16\pm0.14}\mathrm{M}_{\odot}$ haloes independent of redshift within the explored range. This measurement, which is completely independent of clustering methods, is consistent with the lowest mass estimates based on quasar auto-correlation clustering at z$\sim$ 3 and with quasar-galaxies cross-correlation results.

[1]This chapter is adapted from de Beer et al. (2023).

2.1 Introduction

Within the standard paradigm of structure formation we expect that the dark matter and gaseous structures in our universe form due to gravitational collapse, where the matter contracts into sheets and filaments which constitute the Cosmic Web (Bond et al. 1996). The quasi-spherical haloes which are expected to form in the nodes of the web are are continuously fed with primordial and recycled gas through the filaments of the Cosmic Web, with galaxies forming in the central regions of the haloes (Rees & Ostriker 1977; Silk 1977; White & Frenk 1991). Several numerical studies from the last decades have suggested that gaseous filaments penetrating high-redshift haloes can remain relatively cold ($< 10^5 K$) and dense compared to the surrounding halo gas and thus directly feed the central galaxy (Kereš et al. 2005; Agertz et al. 2009; Dekel et al. 2009; Kereš et al. 2009). However recent studies have pointed out, that a lack of spatial resolution could have led to an overestimation of the amount of cold gas reaching the galaxies in this way (Joung et al. 2012a; Mandelker et al. 2016, 2018, 2019a; Peeples et al. 2019; Hummels et al. 2019; Vossberg et al. 2019; Corlies et al. 2020; Gronke et al. 2022; Li & Tonnesen 2020; Fielding et al. 2020). Thus, the detailed physical processes which shape gas accretion onto galaxies and the physical properties of the Circumgalactic Medium (CGM) are still uncertain, especially at $z > 2$, during the peak of galaxy formation. These uncertainties are partly due to the diffuse nature of the gas in the CGM, which has hampered its direct study in emission and thus the possibility to probe its morphology and detailed physical properties.

While the study of absorption features in the spectra of background quasars and galaxies confirmed the existence of a multi-phase CGM (Hennawi et al. 2006; Rubin et al. 2010; Steidel et al. 2010; Rudie et al. 2012; Fumagalli et al. 2013; Turner et al. 2014; Bielby et al. 2017; Dutta et al. 2020, 2021; Lofthouse et al. 2023), the now almost ubiquitous detection of Lyα emission around galaxies, the so called Lyα haloes, has confirmed the existence of an extended reservoir of cold gas in the CGM at high redshift. The detection of these Lyα haloes was enabled by large statistical stacks of Narrow-Band imaging observations (Steidel et al. 2011), deep, long slit spectroscopic observations of multiple foreground and background quasar pairs (Hennawi & Prochaska 2013) and newer, highly sensitive instrumentation such as the MUSE spectrograph and the KCWI being able to reach deeper magnitudes. However, because this Lyα emission could be due to three different emission mechanisms (recombination radiation, collisional excitation and "continuum-pumping"), and because of the resonant nature of Lyα radiation, directly translating these observational constraints into a measurement, e.g. of gas density, is extremely challenging.

Luckily, the phenomenon of quasar fluorescence both increases the brightness of the Lyα emission by orders of magnitudes compared to the CGM of typical galaxies and simplifies the its interpretation (Haiman & Rees 2001; Bunker et al. 2003; Cantalupo et al. 2005). The intense ionising radiation of a bright quasar is able to almost fully ionise its CGM, at least within the quasar ionisation cones, and Cosmic Web filaments on scales of several hundreds of kpc (Cantalupo et al. 2014; Umehata et al. 2019b; Bacon et al. 2021). The resulting recombination emission from

the cold ($< 10^5 K$) gas is easily detectable with Narrow-band imaging and shallow MUSE surveys ($<$ 1 hour of integration time) at $z > 2$ (Cantalupo et al. 2012, 2014; Farina et al. 2017; Borisova et al. 2016; Arrigoni Battaia et al. 2019a; Cantalupo et al. 2019; Drake et al. 2019; Umehata et al. 2019b; Cai et al. 2019; Farina et al. 2019; Fossati et al. 2021). In addition, other CGM emission lines also become easier to detect, including the non-resonant He-Hα emission (Cantalupo et al. 2019) and H-Hα (e.g. Leibler et al. 2018; Langen et al. 2023), and metal emission lines such as the CIV doublet (1548.2 Å, 1550.8 Å) (Travascio et al. 2020; Guo et al. 2020; Fossati et al. 2021). The non-resonant emission lines can then be used to constrain the kinematics, test the recombination-radiation nature of Lyα emission, constrain densities and the "clumpiness" of the medium, even below the spatial resolution scale (e.g. Cantalupo et al. 2019). In the last few years observations of quasar fields with integral-field-spectroscopy have revealed the ubiquity of CGM Lyα emission around quasars at $z > 2$, including quasars with absolute magnitudes within the range of $-27.2 < M_i < -23.7$, some of the faintest known SDSS quasars (e.g. Mackenzie et al. 2021), at all explored redshifts up to the red-wavelength cut-off range of MUSE at $z \sim 6$ (e.g. Farina et al. 2019). The availability of quasars and the ease of detection has produced an impressively large statistical sample of more than a few hundred quasar Lyα nebulae in less than a decade, which can be used to directly probe the CGM's physical properties. The extended and diffuse morphology of these nebulae suggest the presence of a pervasive and diffuse cold component of the CGM, as the recombination process becomes inefficient at higher temperatures.

As the brightness of Lyα nebulae scales with the mass of the halo hosting the quasar and associated nebulae, knowledge of the quasar host halo mass is fundamental to making precise inferences about other properties of the CGM, such as its density distribution, from the Lyα SB (see Section 2.2.1 for more details). Current methodologies of estimating quasar host halo masses rely on measuring quasar auto-correlation functions (or quasar-galaxy cross correlation functions) which in principle can provide precise estimates of halo masses. However, there are significant discrepancies between different works at similar redshifts that are not yet fully understood. In particular, quasar auto correlation studies suggest halo masses between 10^{12}M$_\odot$ and 10^{13}M$_\odot$ (Shen et al. 2007; Eftekharzadeh et al. 2015; Timlin et al. 2018) between $z \sim 3$ and $z \sim 3.5$. In contrast, quasar galaxy cross-correlation studies consistently measure typical quasar halo mass values below $10^{12.5}$M$_\odot$ at redshifts from $z \sim 3$ to $z \sim 4$ (Trainor & Steidel 2012; Font-Ribera et al. 2013; García-Vergara et al. 2017; He et al. 2017) and do not indicate a significant evolution with redshift. At $z > 3.5$, the constraints provided by these studies start diverging from quasar auto-correlation measurements. These discrepancies between quasar auto-correlation and quasar galaxy cross-correlation results at higher redshifts are not yet well understood but have significant implications on the inferred physical properties of the CGM, such as its density distribution. Thus our understanding of the CGM physical properties using its emission will greatly benefit from an alternative and independent methodology to measure quasar host halo masses.

Section 2.2 describes the methods used to derive mock MUSE-like observations which are then used to obtain the line-of-sight velocity dispersion profiles of the emit-

ting gas. In Section 3.3, the new quasar halo mass estimation method is presented, which consists of an analytical relation based on the self-similarity with respect to mass of the velocity dispersion profiles rescaled by the virial radius. In Section 2.3, the method is applied to obtain new constraints on the halo mass associated with observed quasars in the MAGG and MQN samples (Lofthouse et al. 2020; Borisova et al. 2016). Section 2.4 comprises of a discussion of the advantages and limitations of the new mass estimation method and a comparison to previous results from literature. For the sake of consistency with the cosmological simulations used to derive our analytical relation (EAGLE and ENGINE, see Section 3.2.1) we assume the same flat ΛCDM cosmology and use the parameters from the 2013 Planck results (Planck Collaboration et al. 2014). In particular, we use $H_0 = 67.7$ km s^{-1} Mpc^{-1}, $\Omega_b = 0.04852$, and $\Omega_m = 0.307$. Furthermore, we define the virial radius r_{vir} of a halo as r_{200}, the radius at which the average density of the spherical halo reaches 200 times the critical density of the universe at the given redshift.

2.2 Developing a new mass estimation method

In this section, we develop and test a new quasar halo mass estimation method which uses the CGM emission kinematics. As such, it is independent of and complementary to previous quasar clustering studies at $z > 2$. Because current observations only probe the cold ($10^4 < T < 10^5$ K) part of the CGM, the proposed halo mass estimation method will focus on the kinematics of this component and, in particular, on its associated Lyα radiation, which is the most commonly detected emission. An analytical expression quantifying the degeneracy between halo mass and the CGM's physical properties, further motivating the need to fix the host halo's mass, is derived in Section 2.2.1. In order to take the possibly complex morphology and kinematics of gas accretion within dark matter haloes into account, we calibrate our mass estimate method using mock observations of Lyα nebulae in hydrodynamic cosmological simulations of cosmic volumes. The procedure for generating the mock observations is detailed in Section 2.2.2 and the subsequent kinematical analysis is presented in Section 3.3. Finally, in Section 2.2.4 we introduce the new quasar halo mass estimation method.

2.2.1 Degeneracy between halo mass and gas clumping factor

Because the observed SB is the integral of the emissivity over the line of sight, we expect that to the first order it will depend both on halo mass (which determines both the gas density at a given projected distance from the ionising source and the "integration length") and the cold gas density distribution along the line of sight. The latter can be parameterised through the so called "clumping factor" (see, e.g. Cantalupo (2017) for a review):

$$C_l \equiv < n^2 > / < n >^2, \tag{2.1}$$

where n is the gas density and l is the spatial scale (or volume) over which the integral is performed. C_l is by definition equal to one if the density on scales l is constant and greater than one otherwise. Because our main goal is to constrain the CGM gas density distribution from the observed CGM emission SB, it is important to understand its possible degeneracy with other variables. We can derive a simple expectation concerning this degeneracy through analytical considerations as developed in Pezzulli & Cantalupo (2019) (to which we refer the reader for more details). In particular, by rewriting Equation 12 in Pezzulli & Cantalupo (2019) to include the clumping factor[2], one can obtain the following relation between clumping factor, halo mass, CGM cold gas fraction $f_{CGM,cold}$, and the volume filling factor of cold gas (f_v) for a fixed SB profile proportional to $R^{-\beta}$, with $\beta = 1.5$:

$$C_l \propto f_v \, f_{CGM,cold}^{-2} \, M_h^{-5/6}. \tag{2.2}$$

The CGM cold gas fraction used in this relation refers to the total mass of cold gas in the CGM normalised by the total baryonic mass associated to the halo

$$f_{CGM,cold} = \frac{M_{cold}}{(\Omega_b/\Omega_m) M_h} \tag{2.3}$$

and the exponent of the halo mass in Equation 3.12 can be derived as $(1+\beta)/3$. This relation implies that for a fixed SB profile there is a degeneracy between clumping factor, halo mass, CGM cold gas fraction, and the volume filling factor of the cold gas. Thus information concerning these attributes is required to derive the CGM gas density distribution from observed SB profiles. However, the exact behaviour of both quantities is currently unknown in observations and deriving an expectation from simulations is also non-trivial as both quantities may be sensitive to the simulation's feedback recipes and numerical resolution. In Paper II we will study these two quantities in more detail using cosmological simulations of differing resolutions. Under the plausible assumption that these quantities vary slowly within the halo range relevant for this study, Equation 3.12 implies that current uncertainties in the quasar host halo masses as derived by clustering measurements (see Introduction for more details) result in relatively large uncertainties in our ability to constrain the physical properties of the CGM. This highlights the importance of finding complementary methods to constrain quasar host halo masses at $z > 3$ as discussed in this work.

2.2.2 Generating Mock Observations

Cosmological simulations

Quasar clustering estimates suggest that quasar host halo masses are in the range of $10^{12}\mathrm{M}_\odot - 10^{13}\mathrm{M}_\odot$ at $z > 3$ (Shen et al. 2007; Eftekharzadeh et al. 2015; Timlin

[2] in order to include the clumping factor, we substitute f_v in Equation 12 in Pezzulli & Cantalupo (2019) with f_v/C_l following the explanation in Section 2.1.2 of that paper. We note that C_l here refers to the "internal clumping factor" of individual clumps as discussed in detail in Section 2.2.3.

Prefix	L [cMpc]	N	m_g [$M_\odot$]	m_{dm} [$M_\odot$]
Ref	100	1504^3	1.81×10^6	9.70×10^6
RECAL	50	1504^3	2.26×10^5	1.21×10^6
NoAGN	50	1504^3	2.26×10^5	1.21×10^6

Table 2.1: Resolutions and box sizes of the EAGLE (Ref) and ENGINE (RECAL & NoAGN) simulations used in this work. From left to right the columns show: simulation name prefix, the comoving box size, the number of dark matter particles and the initial equal number of baryonic particles, the initial baryonic particle mass and the dark matter particle mass. The mass resolution of the RECAL and NoAGN simulations is 8 times higher than that of the Ref simulation.

et al. 2018). To follow the formation and evolution of these large haloes cosmological simulations with a volume of at least 50 comoving Mpc^3 (cMpc) at $z > 3$ are needed. At the same time, these simulations require a high enough resolution to resolve the kinematic components of the CGM. For this reason, we use the EAGLE (Schaye et al. 2015; Crain et al. 2015; McAlpine et al. 2016; EAGLE-Team 2017) and ENGINE SPH simulation suites which contain haloes with a mass of up to $10^{13.25}$ M$_\odot$. Although the CGM is likely not fully resolved in the EAGLE simulations, Rahmati et al. (2015) have shown that observed global column density distribution function of HI and the observed radial covering fraction profiles of strong HI absorbers around bright quasars are well reproduced. This suggests that the simulations are at least able to capture the large scale distribution of the gas in the CGM. In particular, the ENGINE simulation uses the EAGLE baryonic physics implementation applied to a 50 cMpc^3 volume with the same number of particles as the EAGLE fiducial 100 cMpc^3 simulation, resulting in a higher mass resolution. The specific EAGLE simulation used is called RefL0100N1504 (Ref): a box with a side length of 100 cMpc containing 1504^3 particles with the standard EAGLE stellar and AGN feedback implementation where both stellar and AGN-feedback are modelled with a stochastic injection of thermal energy (Schaye et al. 2015). The two ENGINE simulations used are RECALL0050N1504 (RECAL) and NoAGNL0050N1504 (NoAGN). Both are boxes with a side length of 50 cMpc containing 1504^3 particles with the recalibrated EAGLE stellar feedback implementation. The difference between the two simulations is that RECAL also has AGN-feedback implemented, while in the NoAGN simulation the AGN-feedback is turned off. The reason for including the NoAGN simulations is that it allows us to quantify the effect of the EAGLE AGN-feedback implementation on the obtained mass estimates as discussed in Section 2.4.2. Although the RECAL and NoAGN simulations have the same initial conditions, their simulated haloes and gaseous structures are not identical. This coupled with the projection to two dimensions (see Section 2.2.2) ensures that we do not analyse two sets of identical Lyα nebulae. A basic overview of the simulations properties is given in Table 2.1.

In order to compare our results to current observations, we analyse two snapshots

from each of the three simulations corresponding to redshifts $z = 3.528$ and $z = 3.017$. These two snapshots are chosen to be compatible with the redshift of previous observations of Lyα nebulae (Arrigoni Battaia et al. 2019a; Borisova et al. 2016; Marino et al. 2019; Fossati et al. 2021) and maximise the halo mass coverage, as the range of halo masses contained in the simulation box increases with decreasing redshift.

As is common in current cosmological simulations, the multi-phase inter stellar medium (ISM) is not resolved, so the properties of the star-forming gas is defined by an effective equation of state: $P_{\rm eos} \propto \rho_g^{4/3}$, where $P_{\rm eos}$ is the gas pressure and ρ_g is the gas volume density. This implies that the temperature of these gas particles is artificially set by the effective pressure imposed on the unresolved, multi-phase ISM (Schaye et al. 2015) and not by the hydrodynamical interaction with the ambient gas. In the EAGLE and ENGINE simulations gas is defined to be star-forming, and thus placed on the effective equation of state, if its density lies above the following metallicity (Z) dependant threshold:

$$n_*(Z) = \left(\frac{0.002}{Z}\right)^{0.64} 10^{-1}\mathrm{cm}^{-3}\,. \tag{2.4}$$

As this threshold separates the CGM from the ISM in the cosmological simulation, its actual value is of relevance for the predicted SB of the CGM emission and it will be further explored in Paper II. However, this threshold has a negligible effect on the quasar host halo mass estimate as is demonstrated in Appendix A.

The simulations allow us to separately explore the kinematics of the different components of quasar haloes, including dark matter, cold ($T < 10^5$K) and hot ($T > 10^5$K) gas, of which solely the cold component is currently traceable by CGM emission observations at $z > 2$. The kinematics of the dark matter is directly linked to the gravitational potential of the halo and thus to its mass. In later sections, we explore the relation between the cold and the dark matter kinematics in order to test if the former can be used as a proxy for the latter.

Modelling the CGM emission of quasars

As discussed in the introduction, one of the advantages of studying the Lyα CGM emission around quasars is their intense ionising radiation. This leads to the majority of the hydrogen in their CGM being highly ionised, simplifying Lyα modelling with respect to the CGM of star-forming galaxies for example. In the "highly-ionised" case the the contributions due to collisional excitation (Haiman et al. 2000; Fardal et al. 2001; Dijkstra et al. 2006; Cantalupo et al. 2008; Rosdahl & Blaizot 2012) can be neglected at temperatures above $T = 10^4$K based on the derivation in Pezzulli & Cantalupo (2019). There is not enough neutral hydrogen for collisional excitation to make a significant contribution to the emission, even though the collisional excitation coefficient dominates the recombination coefficient at those temperatures (Cantalupo et al. 2008). We also neglect scattering (or "photon-pumping") of Lyα and continuum photons of galaxies and quasars (Cantalupo et al. 2014), which is difficult to model properly with current numerical models. Sophisticated radiative

transfer modelling would be required and such modelling depends on the optical depth and precise kinematics of the emitting gas clumps on sub-kiloparsec scales which are currently not resolved by cosmological simulations (Hummels et al. 2019; Corlies et al. 2020; Zahedy et al. 2021). Observations of non-resonant lines such as He-Hα and H-Hα confirm that recombination is the main emission source at $z \sim 2.3$ (Leibler et al. 2018; Langen et al. 2023). It is, however, not clear if the same holds at $z > 3$, but upcoming JWST observations will help clarify the issue.

By not modelling any radiative transfer effects we also do not model the broadening of the Lyα line caused by its resonant nature (Cantalupo et al. 2005). However, our mass estimation method is designed to be independent of the line-broadening as is explained in Sections 2.2.3 & 2.2.4. Moreover, as discussed below, the kinematical analysis is predominantly independent of the actual value of the SB, as long as the SB value is high enough to be detectable. For the reasons stated above and for simplicity sake, we thus only include Lyα emission from recombination radiation and we leave further discussion concerning emission mechanisms to Paper II.

We calculate the emissivity of the gas due to Lyα recombination radiation by assuming an ionising source, such as a bright quasar, resides in the centre of each halo and assuming *maximal fluorescence*, i.e. the central ionising source is bright enough to ionise the entirety of the surrounding medium within an opening angle of 100%. The Lyα emissivity $\epsilon_{\mathrm{Ly}\alpha}$ is calculated using the following relation

$$\epsilon_{\mathrm{Ly}\alpha} = \frac{1 - Y/2}{1 - Y} \frac{h\nu_{\mathrm{Ly}\alpha}}{4\pi} n_{\mathrm{H}}^2 \alpha_{\mathrm{eff}}(T) \ . \tag{2.5}$$

Where Y is the number fraction of primordial helium, $(1-Y/2)(1-Y)$ is a correction term due to the presence of primordial helium, h is Planck's constant, $\nu_{\mathrm{Ly}\alpha}$ is the Lyα rest-frame frequency ($1215.67\mathring{A}$), n_{H} is the number density of hydrogen and $\alpha_{\mathrm{eff}}(T)$ is the case A effective recombination coefficient. We note that using the case B effective recombination coefficient would produce very similar results (e.g. Pezzulli & Cantalupo 2019). The case A recombination coefficient is taken from Hui & Gnedin (1997) Appendix A and the (weakly temperature dependent) fraction of recombination events that result in the emission of a Lyα photons is taken from Cantalupo et al. (2005)

$$\alpha_{\mathrm{eff}}(T) = 0.35 \times \alpha(T) \, , \tag{2.6}$$

$$\alpha(T) = 1.269 \times 10^{-13} \mathrm{cm^3 s^{-1}} \frac{\tau^{1.503}}{[\,1.0 + (\tau/0.522)^{0.470}\,]^{\,1.923}} \, , \tag{2.7}$$

$$\tau = 2 \times \frac{157807\,\mathrm{K}}{T} \, . \tag{2.8}$$

A central, ionising source, such as we are assuming, would also heat the gas through photo-electric heating. We refer to this temperature as the photo-heating temperature and its exact value is largely determined by the shape of the ionising spectrum (Osterbrock & Ferland 2006). Pezzulli & Cantalupo (2019) have calculated this photo-heating floor for the ionised CGM as a function of density, metallicity and the ionising QSO spectrum for a distance of 50 kpc away from the ionising source. Their results can be found in the aforementioned work. We adopt a value of

$T = 5 \times 10^4 K$ for the photo-heating floor which corresponds to a metallicity of $0.1 Z_\odot$ and cool phase number density of 1 cm^{-3} assuming a "standard" QSO spectrum (Lusso et al. 2015). While an over- or underestimation of the photo-heating floor does effect the emissivity of the gas, it does not influence our ultimate halo mass estimation. We discuss in Paper II how varying the imposed photo-heating floor changes implications concerning the density of the CGM based on our halo mass estimates and calculated Lyα emissivity.

SPH particle to grid conversion

The large majority of Lyα nebulae known to date have been discovered using integral-field-spectroscopy, e.g. with the MUSE or the KCWI instruments (Wisotzki et al. 2016; Borisova et al. 2016; Leclercq et al. 2017; Arrigoni Battaia et al. 2019a; Fossati et al. 2021). Hence the observations are essentially 3D spatial-spatial-velocity grids. In order to compare the simulation to the data, the SPH-particle based simulations are also converted to grids. We use the code `P2C`[3] (Particles to Chombo; originally developed by S. Cantalupo) to this aim. A brief description of the code is given below.

`P2C` converts particle fields, such as SPH outputs generated by the EAGLE, Sherwood (Bolton et al. 2017) or AREPO (Springel 2010) codes, into adaptively-refined-meshes in the standard "Chombo" format (Adams et al. 2021), which can be used as an input for state-of-the-art visualisation softwares such as VisIt (Childs et al. 2012). In particular, after a regular base grid is defined and populated with the particle data as described below, the mesh can be further refined into a nested hierarchy of rectangular grids of different sizes and levels of refinement, following the implementation called "patch-based AMR", originally described in Berger & Oliger (1984). The algorithm, which has been developed for the RADAMESH radiative-transfer code (Cantalupo & Porciani 2011), is described in detail in section 3.1 of Cantalupo & Porciani (2011). Because our goal is to compare to the uniform three-dimensional grids of MUSE and KCWI, we do not use the multi-mesh capabilities of P2C here. Currently, the gas attributes that can be mapped to the grid are their density, x-, y- & z-velocity, temperature, emissivity and emissivity weighted velocities. The grid cells emissivity values are calculated from the luminosity of the particles. A particle's luminosity is obtained by integrating $\epsilon_{\mathrm{Ly}\alpha}$, as defined in Equation 3.2, over the particle's volume. The particle's luminosity is then distributed over the grid according to a given smoothing kernel. We choose to use the same smoothing kernel as is used in the EAGLE simulations: the C^2 kernel from Wendland (1995) (EAGLE-Team 2017), but note that the actual choice of the smoothing kernel has little effect on scales larger than the smoothing kernel itself, which is usually the case for the majority of the quantities. The user can also choose to exclude gas above a given uniform density threshold or metallicity dependant threshold described in Equation 3.1, as usually done in cosmological simulation to define star-forming regions. A minimum temperature floor, e.g. due to photo-heating, can also be imposed.

[3] `https://gitlab.com/sdebeer/P2C`

Mock integral-field-spectroscopy observations

Due to the complex, non-spherical morphology of the "cold" components in the CGM, the same structure observed from different directions can appear to have completely different morphologies. We take advantage of this effect to increase our sample size by generating three mock integral-field-spectroscopy observations (mock cubes) for each halo included in this analysis by using three perpendicular lines of sight. The mock cubes are designed to be directly comparable to cubes obtained from the MUSE integral field spectrograph, meaning that the cubes have a spatial resolution of 0.2 arcsec ($\sim$ 1.5 physical kpc (pkpc) at both redshifts) and a spectral resolution of 1.25 Å. Their side length is 3.084 cMpc and 3.478 cMpc at $z \sim 3$ and $z \sim 3.5$ respectively.

The first step in generating the mock cubes is to assign all the gas particles in the box centred on the halo centre to a 3D grid and calculate the emissivity in each cell using `P2C`. The velocity of the cells is with respect to the bulk-velocity of the respective central halo and the velocity shift due to the Hubble-flow is accounted for. As mentioned in Section 2.2.2, we impose a photo-heating temperature floor of $5 \times 10^4 K$ on all the cells in the grid. When building the mock cube for a given line of sight, the emissivity field and the emissivity weighted line-of-sight velocity field are used. Each cell in the emissivity field is assigned to a spectral layer based on the corresponding line-of-sight velocity cell. The value of the emissivity grid in that cell is then added to the cell in the mock cube with the same spatial coordinates projected along the line of sight and the corresponding spectral coordinate. The spectral coordinates are calculated by dividing the grid's line-of-sight velocity range into spectral layers of 1.25 Å and assigning the cells to spectral layers based on their line-of-sight velocity with respect to the central halo. This corresponds to layers with a width of 75 km s^{-1} for redshift $z \sim 3$ and 68 km s^{-1} for redshift $z \sim 3.5$.

Operating under the assumption of *maximal fluorescence*, we treat the whole mock-cube simulation volume as ionised. In order to avoid over-ionising the gas at the largest distances we simply impose an upper fluorescent SB limit[4]. The limit depends on the distance from the central ionising source as well as its ionising luminosity. It is given by

$$\mathrm{SB_{max}} = 2.25\mathrm{e}{-17} \left(\frac{1+2.3}{1+z} \right)^4 \frac{1}{\mathrm{R}^2} \frac{\mathrm{erg}}{\mathrm{s\ cm^2\ arcsec^2\ \AA}}\,, \tag{2.9}$$

where R is the distance to the central ionising source in units of phys Mpc assuming an ionising luminosity comparable to the UM287 quasar (Cantalupo et al. 2014, 2019). As the i-band magnitude of the quasar UM287 is comparable to that of bright quasars observed with MUSE this relation is also applicable to our mock observations. To mimic typical seeing conditions we apply two dimensional Gaussian smoothing to each spectral layer individually, we additionally mimic the typical

[4]This upper limit should be thought of as a safety net for extreme cases with negligible effect on the generated mock observations. As a reference point: The maximum number of voxels affected by this upper limit in one mock observation is roughly 30 out of $512^2 \times$ 22.

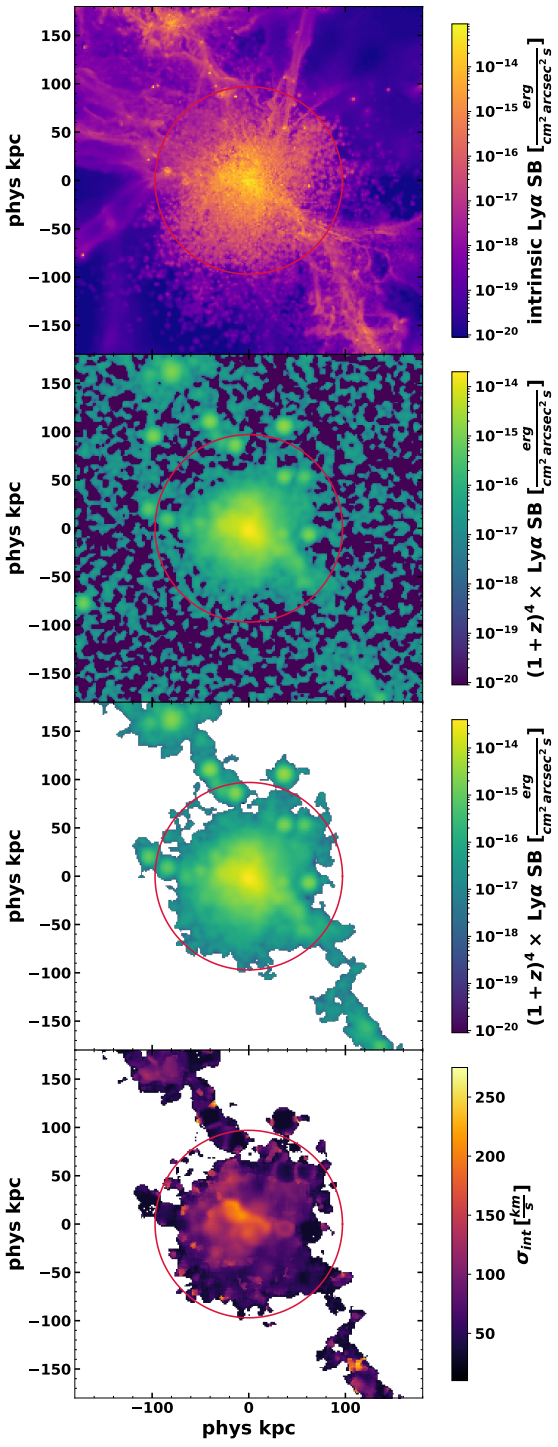

Figure 2.1: A visual representation of the conversion from simulation to velocity dispersion maps of a $1.9 \times 10^{12} M_{\odot}$ halo included in the analysis. From top to bottom: The intrinsic Lyα SB map, obtained by summing the emissivity grid output by `P2C` over a line of sight. The SB map of the mock cube generated from said grid. The SB map of the central Lyα nebula extracted using `CubEx`. Lastly, the intrinsic velocity dispersion map of the nebula. In each panel the halo's virial radius is marked with a red circle and the SB values in the top three panels are not corrected for cosmological dimming.

z	number of haloes	number of Lyα nebulae	detection rate
3.528	73 (NoAGN) 74 (RECAL) 639 (Ref)	219 (NoAGN) 222 (RECAL) 1917 (Ref)	100% (NoAGN) 100% (RECAL) 100% (Ref)
3.017	107 (NoAGN) 109 (RECAL) 941 (Ref)	321 (NoAGN) 327 (RECAL) 2769 (Ref)	100% (NoAGN) 100% (RECAL) 98% (Ref)

Table 2.2: The number of haloes and Lyα nebulae analysed. From left to right the columns show: the redshift of the simulation snapshots, the number of haloes within the halo mass range $10^{11.75}$M$_\odot$ - $10^{13.25}$M$_\odot$ in each simulation snapshot, the number of Lyα nebulae extracted from those haloes using three perpendicular lines of sight and the detection rate of Lyα nebulae in the mock observations.

MUSE line spread function as reported in Bacon et al. (2017) by applying Gaussian smoothing along the spectral dimension. We then add artificial noise to the mock cubes layer by layer which has a Gaussian distribution with a standard deviation of $\sigma = 5 \times 10^{-20}$ erg/(s cm^2 arcsec^2 Å). We note that this noise level typically corresponds to a time integration of more than 10 hours with MUSE, i.e. to a deep observation. However, as we demonstrate in Appendix B, the results presented here are not particularly affected by the chosen noise level as long as the nebula is detected with at least two wavelength layers per spaxel.

As the gas's emissivity depends on the square of its density and thus on the CGM clumping factor (see Equation 3.2), there is a link between the signal-to-noise ratio (SNR) in an individual mock cube voxel and the density of the gas attributed to that voxel. In general, at a set distance from the halo centre, the average gas density and thus both the emissivity and SNR are lower for a halo with lower mass. The nebulae extracted from mock cubes around haloes with masses above 10^{12}M$_\odot$ are not affected by noise levels which are an order of magnitude higher than the one used here. However, haloes below 10^{12}M$_\odot$ in EAGLE have average densities and clumping factors which would preclude their detection in shallow MUSE observations (a detailed comparison of mock and observed SB will be presented in Paper II). We stress that the SB normalisation, driven by the unknown gas clumping factor, is not important for the results presented here (see Appendix C). Therefore, instead of increasing the SB normalisation, or the gas clumping factor, by an arbitrary value we have decided to keep the noise level low in order to increase the detectability of nebulae across a large mass range.

Detection and extraction of Lyα nebulae

In order to make our analysis as similar as possible to the actual observations, we detect and extract the Lyα nebulae from the mock cubes using `CubEx` from the `CubeExtractor` package (Cantalupo et al. 2019) which has been widely used in the literature (Borisova et al. 2016; Marino et al. 2018, 2019; Arrigoni Battaia

et al. 2019a; Langen et al. 2023). In particular, we use the following parameters, which are very similar to the ones used in actual observations. For an object to be extracted we require that all voxels attributed to that object have a SNR value above 2.0 and that the object consists of at least 1000 voxels. If multiple objects extracted from the mock cube fulfil these criteria we choose the object with the largest number of voxels. We find that the object with the largest number of voxels always spatially coincides with the massive halo selected as the centre of the mock cube. If no object is extracted from the mock cube, that cube is discarded from our sample. Table 2.2 lists how many haloes are analysed at each redshift, how many nebulae are extracted and the Lyα nebulae detection rates. The number of nebulae is higher than the number of haloes as for each halo we generate three mock cubes using three perpendicular lines of sight. As done in observations, we calculate the velocity dispersion as the second moment of the flux distribution using the segmentation mask generated by `CubEx` through the `Cube2Im` software, also part of the `CubeExtractor` package. We require that the detected emission occupies at least 2 spectral layers at a given spatial coordinate for the velocity dispersion to be calculated in that spaxel. We also apply a 3×3 spatial boxcar smoothing filter before generating the velocity dispersion maps. As we do not model any radiative transfer effects, the velocity dispersion calculated in this way directly traces the kinematics of the emitting gas. We therefore refer to it as the *intrinsic* velocity dispersion, in order to differentiate this quantity from the observed velocity dispersion, which is subject to radiative transfer effects.

In Figure 2.1, we give an example of the process of converting the simulated haloes to velocity dispersion maps. Each panel depicts one stage of this conversion for a $1.9 \times 10^{12} M_{\odot}$ halo included in this analysis. In each panel the halo centre is located in the middle and its virial radius is marked with a red circle. The top panel shows the Lyα emissivity as calculated by `P2C`, summed up over a given line of sight axis, resulting in an intrinsic Lyα SB map of the halo. The main halo and subhaloes are visible as well as the two major cosmic web filaments penetrating it. There are also numerous, more delicate filaments evident in emission. The second panel shows a surface brightness map generated from the mock cube containing the halo, using the same line of sight. The main halo, some subhaloes and the main filaments are still visible, however, the more tenuous filaments have now become undetectable under the noise. The third panel from the top contains the surface brightness map solely of the region attributed to the main Lyα nebula as extracted by `CubEx` using SNR = 2.0. Both major filaments are included in the detected emission. The bottom panel shows the intrinsic velocity dispersion map of the main nebula generated using `Cube2Im`. There is clearly a maximum in the region of the halo centre with the intrinsic velocity dispersion decreasing at larger distances.

It is worth stressing that the mock Lyα nebulae obtained through our method exhibit morphologies which resemble comparable observed nebulae (Borisova et al. 2016; Arrigoni Battaia et al. 2019a; Fossati et al. 2021), although they tend to be systematically dimmer. This may be due to the small scale clumpiness which is unresolved in the EAGLE/ENGINE simulations, as we will discuss in greater detail in Paper II.

2.2.3 Kinematical analysis of the cold CGM

In order to quantify the link between the kinematics of the cold ($< 10^5 K$) CGM and the mass of the host halo in the simulations, we compare the spherically averaged radial velocity profiles of the dark matter, the cold, Lyα emitting gas and the hot ($> 10^5 K$) gas. Building on the link revealed in the spherically averaged radial velocity profiles (Section 2.2.3), we investigate the evolution of the circularly averaged intrinsic velocity dispersion profiles with host halo mass, showing they are actually self-similar. We switch from the radial velocity to the intrinsic Lyα velocity dispersion, as the radial velocity is not an observable. With the link between the intrinsic velocity dispersion and the host halo mass established in Section 2.2.3, we discuss how we correct for the resonant broadening of the Lyα line in Section 2.2.3. Finally, in Section 2.2.4 we derive an analytical relation based on the self-similarity of the Lyα velocity dispersion profiles which can be used to constrain the host halo mass.

Radial velocity profiles

We analyse the radial velocity of the gas and dark matter surrounding the haloes in the Ref and RECAL simulations at redshifts $z \sim 3.5$ and $z \sim 3$. To do this, we calculate the spherically averaged radial velocity profiles of the dark matter, the hot gas ($T > 10^5 K$) and the Lyα emitting gas within five virial radii of each halo. For each simulation and redshift we divide the haloes into four mass bins and stack the radial profiles of each mass bin by calculating the median of all spherically averaged radial profiles in that mass bin. For the dark matter we calculate the radial velocity of each dark matter particle with respect to the halo's centre of gravity. For the Lyα emitting gas and the hot gas we calculate the radial velocity of the gas in each cell obtained with `P2C`. To calculate the profiles of the Lyα emitting gas we calculate the average radial velocity of the gas in all cells contained within a given spherical shell and use the Lyα emissivity of the cells as weights. Figure 2.2 shows the radial velocity profiles at $z \sim 3.5$ and $z \sim 3$ for the four mass bins considered.

At a distance of roughly three virial radii and further away from the halo centre the radial velocity of the Lyα emitting gas is consistent with that of the hot gas and the dark matter for all halo masses, redshifts, and simulations. The negative radial velocities of the gas and dark matter imply that all three are flowing towards the halo centre. The fact that the radial velocity values of both the hot and Lyα emitting gas are consistent with those of the dark matter suggests that, at these large distances, the gas is kinematically tracing the dark matter. In all four mass bins, at roughly three virial radii from the halo centre the average radial velocity of the hot gas begins to increase, diverging from that of the dark matter and Lyα emitting gas. This divergence is likely caused by hot outflows which result in a positive (outflowing) radial velocity for the hot gas out to roughly two virial radii. The outflows are driven by stellar & AGN-feedback that simultaneously heat and expel the gas from the central galaxy and the halo in the EAGLE & ENGINE simulations. However, not all the gas is heated and expelled as indicated by the fact the Lyα emitting gas, which effectively corresponds to the cold gas ($T < 10^5$ K),

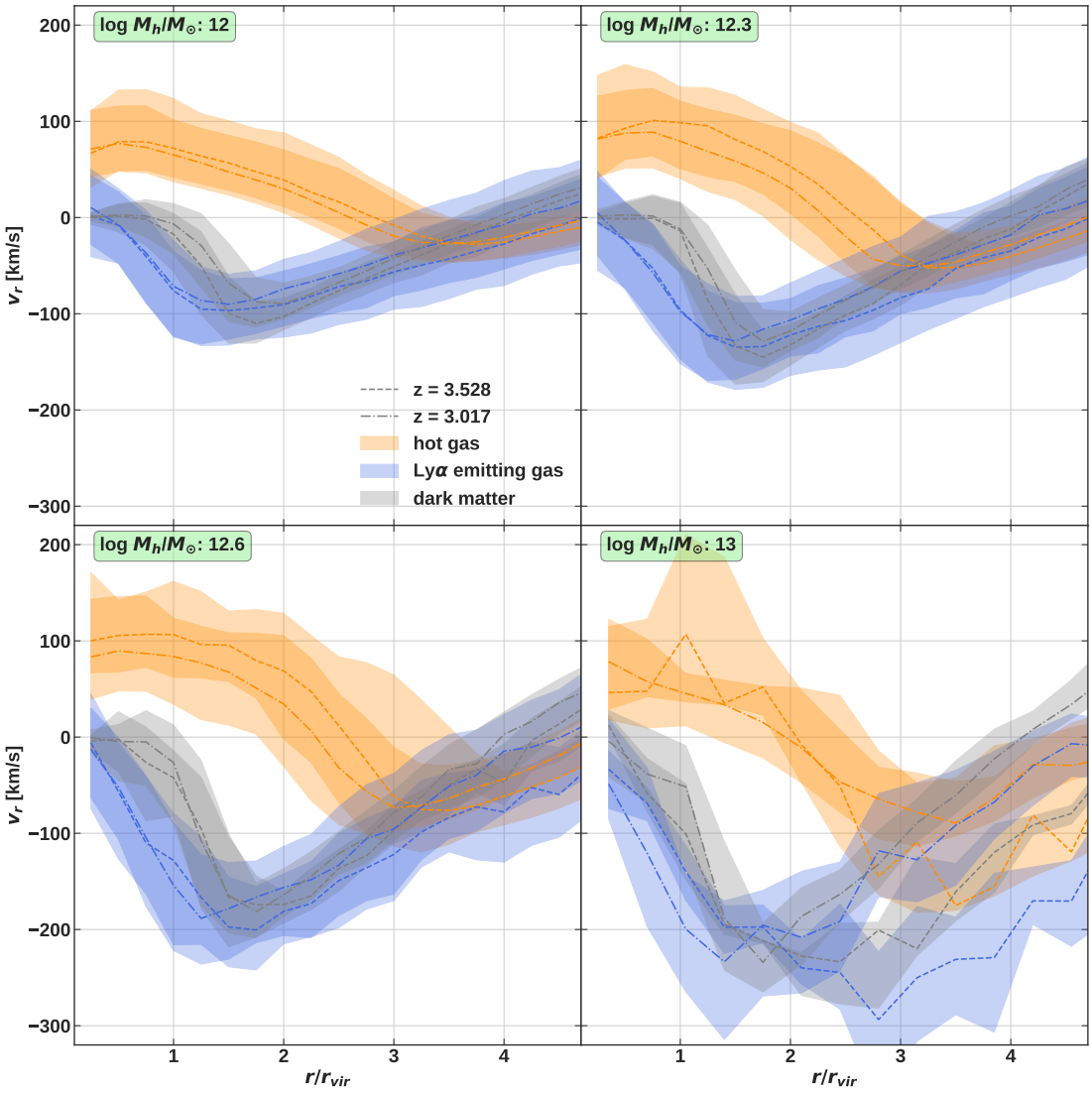

Figure 2.2: Spherically averaged radial velocity profiles of the dark matter (grey), the Lyα emitting gas (blue) and the hot ($> 10^5 K$) gas (orange) at redshifts $z = 3.528$ (dashed lines) and $z = 3.017$ (dash-dotted lines). Before stacking, distances from the centre of the haloes for each individual profile are rescaled by the host halo's virial radius. The mass bins are centred on $10^{12} M_\odot$, $10^{12.3} M_\odot$, $10^{12.6} M_\odot$ and $10^{13} M_\odot$ as indicated in the labels within the panels. The three lower mass bins are 0.3 dex wide and the highest mass bin has an extent of 0.5 dex in order to increase statistics. The shaded areas indicate the range spanned by the 25th and 75th percentile for each radial profile. The radial velocity of the hot gas diverges from that of the Lyα emitting gas and the dark matter at $\sim 3 r_{vir}$. Remarkably, the radial velocities of the Lyα emitting gas and dark matter follow each other up until $\sim 1.5 r_{vir}$. We will use this result to derive a relation between the line-of-sight velocity dispersion of the Lyα emitting gas and halo mass as explained in Section 2.2.4.

continues to fall towards the halo centre, kinematically tracing the dark matter.

Both the dark matter and Lyα emitting gas are accelerated towards the halo centre until their radial inflow velocity abruptly starts to decrease. This decrease occurs between one and two virial radii with the decrease in the dark matter's radial inflow velocity occurring up to 0.5 virial radii before that of the Lyα emitting gas. The apparent radial deceleration of the dark matter is likely due to the co-existence of particles with positive and negative radial velocities associated with virialisation. The radial deceleration of the Lyα emitting gas could be explained by weak virial shocks that, despite decreasing the radial inflow velocity, do not heat it to virial temperature or other hydrodynamical interactions. We note that the dark matter's point of maximum infall velocity coincides with the halo's splashback radius (Fillmore & Goldreich 1984; Bertschinger 1985; Diemer & Kravtsov 2014; More et al. 2015). For both the dark matter and Lyα emitting gas the maximum radial infall velocity increases with increasing halo mass.

These results clearly indicate that the kinematics of the Lyα emitting gas are dominated by gravity up to 1.5-3 virial radii from the halo centre, at least within the assumptions made in the EAGLE and ENGINE models. Moreover, the fact that the radial velocity of the Lyα emitting gas is almost exclusively negative implies that Lyα emission traces the gas accreting into the halo.

As mentioned in Section 3.2.1, the incorporation of both the RECAL and NoAGN ENGINE simulations allows us to quantify the effect of the EAGLE AGN-feedback implementation on the kinematics of the gas. We find that the AGN-feedback has no effect on the radial velocity of the Lyα emitting gas and that stellar feedback is the main driver of the hot outflows as can be seen in Appendix D in Figures D.4 & D.5.

Our findings with regard to the radial velocity profiles are broadly consistent with similar analyses performed on different sets of cosmological simulations. For instance, the distance at which the radial velocity of the Lyα emitting gas begins increasing is consistent with the distance of $0.75 - 1.25 r_{vir}$ that Nelson et al. (2016) find. The bi-modal behaviour of the hot and cold (Lyα emitting) gas has also been observed by Huscher et al. (2021) for an EAGLE zoom simulation of galaxy haloes at redshift $z \sim 2 - 3$ with masses of $\approx 10^{12} \mathrm{M}_{\odot}$.

The profiles shown in Figure 2.2 clearly reveal a correlation between the maximum infall velocity and halo mass. Similarly, there is evidence for a correlation between the point of deceleration of the accreting gas and the halo's virial radius. These results suggest that the maximum infall velocity and point of deceleration of the Lyα emitting gas could be used to determine the halo's mass, if they could be observed.

Velocity dispersion profiles

As the radial velocity of the Lyα emitting gas is not a direct observable, we investigate whether there is any correlation present between the observable line-of-sight velocity dispersion and halo mass. Analogously to the radial velocity profiles, we calculate the circularly averaged velocity dispersion profile for each halo and each of

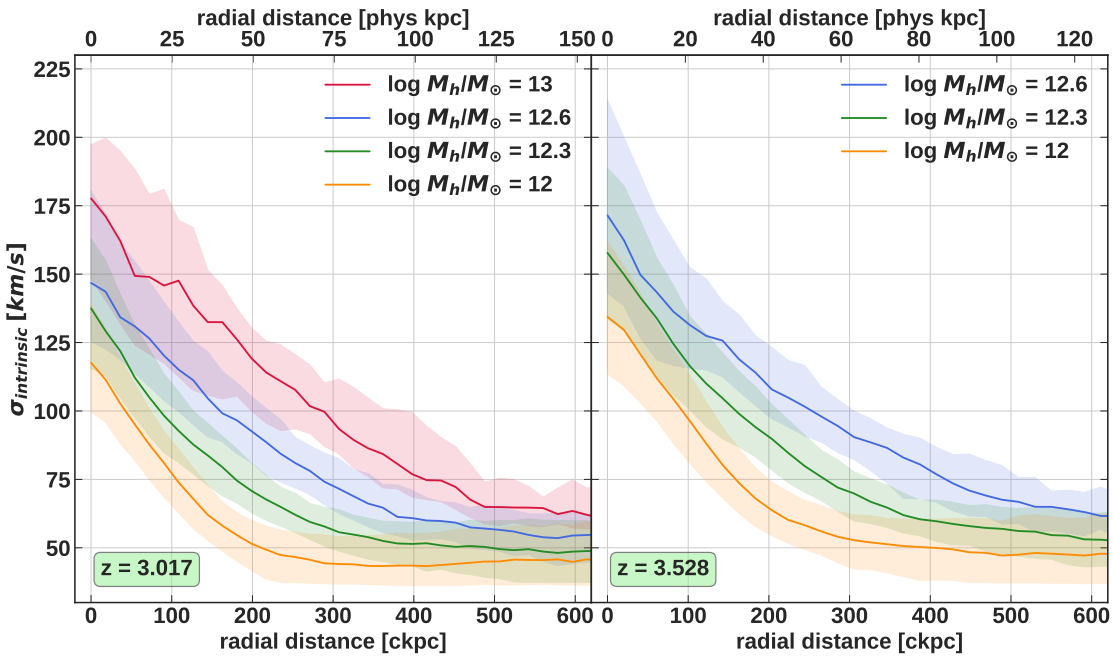

Figure 2.3: Circularly averaged intrinsic velocity dispersion profiles of the extracted Lyα nebulae hosted by haloes with masses of $10^{12\pm0.15}M_\odot$ (yellow), $10^{12.3\pm0.15}M_\odot$ (green), $10^{12.6\pm0.15}M_\odot$ (blue) & $10^{13\pm0.25}M_\odot$ (red). The left panel shows the velocity dispersion profiles for Lyα nebulae at redshift $z = 3.017$ and the right panel shows the profiles for $z = 3.528$. The region between the 25th and 75th percentile of the velocity dispersion for each mass bin is delimited by the shaded areas. The mass bin $10^{13\pm0.25}M_\odot$ is not included for $z = 3.528$ as there are only 2 haloes contained in that mass bin at that redshift. The maximum velocity dispersion value increases with halo mass analogously to the maximum radial inflow velocity. Additionally, the shape of the intrinsic velocity dispersion profiles becomes flatter/less concave with increasing halo mass.

its lines of sight in all three simulations at both redshifts. Then we divide the haloes into the same mass bins and stack the circularly averaged velocity dispersion profiles for each mass bin by calculating the median velocity dispersion profile. The stacked velocity dispersion profiles are shown in Figure 2.3. As explained in Section 2.2.2, we remind the reader that the plots show the intrinsic velocity dispersion without taking radiative transfer effects into account.

Previous observations of Lyα nebulae have found average velocity dispersion values of $\sigma \approx 250$ km/s and higher (Arrigoni Battaia et al. 2015; Borisova et al. 2016; Cantalupo et al. 2019; Marino et al. 2019; Drake et al. 2022). Our stacked profiles do not reach such high values and are more compatible with velocity dispersion values $\sigma \approx 100$km/s of HeII-1640Å nebulae that are co-spatial with Lyα nebulae around AGNs (Marino et al. 2019, Travascio et al. in Prep.). The lower velocity dispersion values measured in the co-spatial HeII nebulae are due to the absence of resonant broadening effects. This implies that the intrinsic kinematics of the emitting gas in the CGM is traced by the emission from the HeII-1640Å transition in observations, just as the intrinsic kinematics of the emitting gas in the simulations is traced by

the mock Lyα emission. The agreement between our simulated intrinsic velocity dispersion values and the observed ones indicates that although the CGM is likely unresolved in the simulations, its large scale kinematics are well reproduced.

Similarly to the maximum infall velocity, the maximum intrinsic velocity dispersion increases with halo mass at both redshifts for all three simulations. The shape of the profiles also becomes flatter/less concave with increasing halo mass. Both of these findings can be explained with the behaviour of the radial velocity profiles discussed in Section 2.2.3. In particular, due to the projection effects, higher infall velocities translate to a larger spread of velocities along the line of sight. The flattening is connected to the fact that the point where the radial inflow velocity of the gas starts to decrease is at the same distance in virial radii units from the halo centre. Due to $r_{vir} \propto M_{halo}^{(1/3)}$, this point is farther away from the halo centre for higher mass haloes. In particular, this point of deceleration corresponds to the region where the velocity dispersion profile transitions from constant to monotonically increasing. Thus, the farther away this point is from the halo centre, the flatter the profile.

In order to quantify in which way the flattening depends on the halo mass, we plot the intrinsic velocity dispersion as a function of r/r$_{vir}$ and rescale the profiles by their value in the the inner most radial bin in Figure 2.4. At both redshifts the rescaling leads to the profiles coming to lie on top of each other, independently of redshift and halo mass. This self-similarity with respect to halo mass of the rescaled velocity dispersion profiles is consistent with expectations from dark matter simulations, observational results pointing to the self-similarity of the cold CGM with respect to the virial radius (Churchill et al. 2013a,b) and with the fact that the Lyα kinematics closely trace the dark matter kinematics in the EAGLE simulations (see Figure 2.2). This result gives us the opportunity to constrain the virial radius, and thus the halo mass, from the shape of the Lyα velocity dispersion profile, which is an observable quantity. In order to facilitate this task, we obtain an analytical relation between the rescaled velocity dispersion and the halo's virial radius by fitting a third degree polynomial to the rescaled velocity dispersion profiles of each individual nebula. The coefficients of the fitted polynomial

$$\sigma_{rescaled}(x) = ax^3 + bx^2 + cx + d \tag{2.10}$$

are $a = 0.168 \pm 0.016$, $b = 0.174 \pm 0.03$, $c = -0.96 \pm 0.016$ and $d = 1.018 \pm 0.001$, where x is the projected distance to the centre of the nebula rescaled by the halo's virial radius: r/r_{vir}. While performing the fit, only values at radial distances less than 1.25 r/r_{vir} are considered in order to avoid including the plateau region of the profiles which could be affected by signal-to-noise and spectral resolution limitations. The analytical relation is plotted with a black, dashed line in both panels in Figure 2.4. The mean rescaled velocity dispersion profiles for each mass bin are also plotted in red, blue, green and orange with the standard deviation for each mass bin indicated by the shaded regions. The fact that the fitted analytical function is in good agreement with the mean profile of each halo mass bin indicates that this relation holds equally well for the whole mass range considered in this work. We stress that fitting the polynomial to the median rescaled profiles would

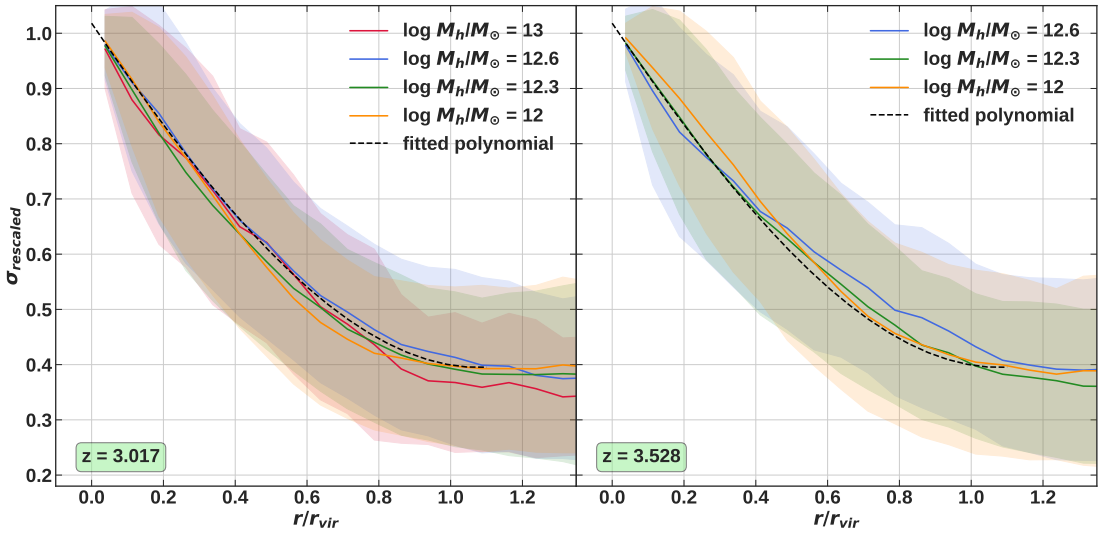

Figure 2.4: Circularly averaged profiles of the rescaled intrinsic velocity dispersion as a function of virial radius of the halo hosting the extracted Lyα nebulae. The average profiles of the mass bin $10^{12\pm0.15}M_\odot$ (yellow), $10^{12.3\pm0.15}M_\odot$ (green), $10^{12.6\pm0.15}M_\odot$ (blue) & $10^{13\pm0.35}M_\odot$ (red) are shown with the shaded regions indicating the respective standard deviations. The left panel shows the profiles for redshift $z = 3.017$ and the right shows them for $z = 3.528$. The joint rescaling of the distance to the halo centre and the intrinsic velocity dispersion leads to all profiles of the different mass bins lying on top of each other, demonstrating the dependence on halo mass of both the intrinsic velocity dispersion values and the profiles shapes. The third degree polynomial fitted to all individual profiles is plotted in black in both panels. Its excellent agreement with each average profile further confirms the self-similarity of the rescaled velocity dispersion profiles.

result in a very similar shape and thus would not significantly affect our results as presented in Section 2.2.4.

In principle, applying this relation to observations could directly constrain the virial radius and thus halo mass. A direct comparison between the self-similar rescaled velocity dispersion profiles and observations is however impractical for the majority of observed nebulae given their limited signal-to-noise ratios. Moreover, the central bin used for the rescaling is typically dominated by the bright quasar Point-Spread-Function (PSF). For these reasons we introduce a new parametrisation in Section 2.2.4 which is based on the analytical relation presented in Figure 2.5 and mitigates these observational limitations. However, before proceeding further, the resonant broadening of the Lyα velocity profile must be taken into account, as discussed in the next section.

Lyα spectral broadening

In the previous sections we generate Lyα velocity dispersion profiles under the assumption of maximal fluorescence and ignoring possible radiative transfer effects ("intrinsic" velocity dispersion profiles). In this section, we first verify that the gas

in the CGM is not highly self-shielded and then derive the effect of radiative transfer on the shape and normalisation of the observable velocity dispersion. We then compare our analytical expectations with observations.

The large Lyα absorption cross section ($\sigma_0 \simeq 5.9 \times 10^{-14}$ cm^2 at line centre for T=10^4K) implies that even a highly ionised medium such as the CGM of quasars could have a high opacity to Lyα photons generated by recombinations. Let us assume, following Pezzulli & Cantalupo (2019), that the CGM is composed of a hot component (at about the virial temperature) and a cold component at a temperature fixed by quasar photoionisation in the form of clouds (of arbitrary shape) with a typical size l and average density n. The average neutral density ($< n_{\rm HI} >$) of these clouds at a distance r from the quasar will be given by

$$< n_{\rm HI} > \simeq \frac{< n_{\rm H} >^2 \ \alpha(T) \ C_l}{\Gamma_i} = \\ 4.8 \times 10^{-6} C_l \ T_4^{-0.75} \left[\frac{< n_{\rm H} >}{\rm cm^{-3}}\right]^2 \left[\frac{r}{30 \ \rm kpc}\right]^2 \ {\rm cm^{-3}}, \tag{2.11}$$

under the plausible assumption that $\Gamma_i \gg n \cdot \alpha(T)$, where $\Gamma_i \simeq 10^{-7} (r/30{\rm kpc})^{-2} {\rm s}^{-1}$ is the photoionisation rate of bright quasars in MUSE surveys such as Borisova et al. (2016) (see Pezzulli & Cantalupo (2019) for details), $T_4 \equiv T/(10^4{\rm K})$, $\alpha(T) = 4.8 \times 10^{-13} T_4^{-0.75} {\rm cm^3 s^{-1}}$ is the hydrogen case A recombination coefficient[5] , and C_l is the clumping factor over scales l previously introduced in Section 2.2.1.

The neutral hydrogen column density ($N_{\rm HI}$) of such clouds is thus

$$N_{\rm HI} = < n_{\rm HI} > l \simeq \\ \simeq 1.5 \times 10^{15} C_l \ T_4^{-0.75} \ \left[\frac{n}{\rm cm^{-3}}\right]^2 \left[\frac{r}{30 \ \rm kpc}\right]^2 \left[\frac{l}{100 \rm pc}\right] \ {\rm cm^{-2}} \ . \tag{2.12}$$

Under the assumption that the observed Lyα SB is produced by recombination radiation, Pezzulli & Cantalupo (2019) have derived the following radial average density profiles for clouds at a distance r from quasars in the Borisova et al. (2016) sample at $z \sim 3.2$ (which we assume in the following as a reference redshift)

$$n(r) = 1.2 \ C_l^{-1/2} T_4^{0.48} \left[\frac{f_v}{10^{-3}}\right]^{-0.5} \left[\frac{r}{30 \ \rm kpc}\right]^{-1.25} {\rm cm^{-3}}, \tag{2.13}$$

where f_v is the volume filling factor occupied by cold clouds with average a density n on scales of l.

The cloud size is connected to the volume filling factor through this relation

$$l = r_{\rm vir} \cdot f_v \cdot f_c^{-1} \simeq 74 \left[\frac{f_v}{10^{-3}}\right] f_c^{-1} M_{12}^{1/3} \ {\rm pc}, \tag{2.14}$$

[5]The case A recombination coefficient $\alpha(T)$ quoted in this section is taken from Pezzulli & Cantalupo (2019) for the sake of consistency with their derivation. However, although this approximation differs slightly from the $\alpha(T)$ defined in Section 2.2.2, both calculations of the Lyα emissivity $\epsilon_{\rm Ly\alpha}$ in Section 2.2.2 and of the average neutral fraction $x_{\rm HI}$ this Section are insensitive to the exact approximation of $\alpha(T)$ used.

where $r_{\rm vir}$ is the halo's virial radius, f_c is the covering factor as seen by the quasar, or, equivalently, the average number of clouds with size l between the quasar and the virial radius (assumed here to be the far "edge" of the CGM for simplicity), and M_{12} is the total halo mass in units of 10^{12} $M_\odot$.

Inserting Equations 2.13 and 2.14 into Equation 2.12, we finally obtain

$$N_{\rm HI} \simeq 1.6 \times 10^{15} \left[\frac{r}{30 \text{ kpc}}\right]^{-0.5} T_4^{0.21} f_c^{-1} M_{12}^{1/3} \text{ cm}^{-2}, \tag{2.15}$$

or, equivalently, in terms of line centre optical depth to the Lyα radiation (τ_0)

$$\tau_0 \simeq 94.4 \left[\frac{r}{30 \text{ kpc}}\right]^{-0.5} T_4^{0.21} f_c^{-1} M_{12}^{1/3}, \tag{2.16}$$

where we have used the relation $\sigma_0 \simeq 5.9 \times 10^{-14} T_4^{-1/2}$ for the line centre cross section and assumed the *internal* velocity dispersion of the clouds, or equivalently, the gas velocity dispersion on scales of l, to be dominated by the thermal broadening due to quasar photoheating.

Equation 2.12 implies that both $N_{\rm HI}$ and τ_0 depend linearly on the size of the clouds l, which is currently unknown. As demonstrated in Equations 2.14 - 2.16 the unknown cloud size l can be recast in terms of the covering factor f_c along the quasar line-of-sight. Doing this, one can characterise the local $N_{\rm HI}$ and τ_0 as inversely proportional to a global value of f_c and mildly proportional to the other parameters (distance from the quasar, cloud temperature and halo mass). In principle, the covering factor can be measured by looking at quasar absorption spectra. In practice, however, it could be challenging to identify and count absorption lines in a very narrow velocity window, which from the results presented above should be of the order of a few hundred km/s without a very precise measurement of the quasar systemic redshift.

However, we can provide some useful limits on the value of f_c from the following considerations. The smoothness of observed SB maps indicates that the individual clouds must have sizes smaller than the spatial resolution element of the MUSE observations, which is typically 5 kpc. Additionally, observations in both absorption and emission have placed upper limits on the individual cloud sizes of $l \lesssim 20-500$ pc (Crighton et al. 2015a; Arrigoni Battaia et al. 2015). Using eq. 2.14 and assuming $f_v = 10^{-3}$, this would imply $f_c > 0.15$ and thus $N_{\rm HI} < 10^{16}$ cm^{-2}. Such column densities and their associated optical depths are below the HI self-shielding limit to the ionising radiation, implying that these clouds produce Lyα photons from recombination efficiently, as initially assumed. We discuss how our results would be effected by the presence of neutral gas, due to a smaller ionisation cone for instance, in Section 2.4.1. On the other hand, as long as $f_c < 100$ (and thus $\tau_0 > 1$), the associated absorption lines to these clouds in the spectra of observed quasars should be easily measurable.

Let us consider, as an example, the observed dN/dz of observed absorption line systems in the presence of the quasar "proximity effect" and overdensity of matter

in their associated haloes. In particular, we can define the expected number of absorption line systems at a distance r from the quasar as

$$\frac{dN}{dz} = N_0(1+z)^{\gamma}[1+\frac{\Gamma_i(r)}{\Gamma_{\rm UVB}}]^{-(\beta-1)}\,\delta^{\,(\beta-1)} \times \Delta(r), \tag{2.17}$$

where $N_0(=6.1)$ and $\gamma(=2.47)$ are observationally derived parameters which describe the number density of absorption line systems away from quasars in a given column density range ($13.64 \lessapprox \log N_{\rm HI} \lessapprox 17$, corresponding to the f_c limits discussed above). The parameter $\beta(=1.6)$ is also observationally constrained and describes the column density distribution function which is consistent with a power law with index $-\beta$ (see e.g. Meiksin 2009, and references therein) and $\Gamma_{\rm UVB}$ is the photoionisation rate in absence of radiation from the quasar (i.e., only due to the cosmic UV background). $\Delta(r)$ is a factor which accounts for the increase in number density of systems of a given column density (in absence of quasar radiation) at a distance r from the quasar. The factor $\delta^{\,(\beta-1)}$ quantifies the fact that the internal density of these clouds could increase due to compression from the hot component of the CGM, which in turn would lead to an increase of the recombination rate, thus counteracting the aforementioned "proximity effect". Substituting the numerical values, assuming $\Gamma_{\rm UVB} = 10^{-12}$ s^{-1}, $z = 3.5$, $\delta = 1$ and using $r = r_{\rm vir}$, we obtain

$$f_c \simeq 0.5\Delta z \times \Delta(r_{\rm vir}) \simeq 0.75\frac{\Delta {\rm v}(\Delta z)}{100{\rm km\ s^{-1}}}\frac{\Delta(r_{\rm vir})}{1000}. \tag{2.18}$$

As the value of δ is unknown, we set it to the lower limit of 1, but note that δ could contribute to a higher covering factor. We also stress that the actual value of $\Delta(r_{\rm vir})$ is unknown and likely larger than the canonical value of 200 given by gravity alone since the physics that determines the properties of clouds in the CGM of a massive halo could be different to the physics for the generic cloud population in the IGM. However, it is interesting to consider that unless $\Delta(r_{\rm vir})$ is extremely large, we obtain f_c values which are of the order of unity which would imply $\tau_0 >> 1$, in addition to $\tau_0 < 10^4$, as derived above.

Once produced within the clouds, the Lyα photons thus cannot directly escape from the interior regions of the cloud and will be absorbed and re-emitted by atoms *within* the cloud (thus experiencing negligible spatial diffusion compared to CGM scales) until their frequency is sufficiently far away from the line centre. Unfortunately, there are no analytical solutions to predict the emerging spectral shape of the Lyα photons at such values of τ_0. However, we do expect that the emerging spectrum would have a significant depletion of Lyα photons at the line centre with respect to the "intrinsic" spectrum. As a reference, a pure absorbing screen with $N_{\rm HI} \simeq 10^{16}$ cm^{-2} (which is on the flat or "logarithmic" part of the Lyα equivalent width curve of growth) would produce an absorption line with a FWHM of about four times the value of the Doppler parameter (e.g. Meiksin 2009).

The emerging spectrum from an individual cloud would then be significantly broader than the "intrinsic one". However, the amount of broadening for each individual cloud would be rather insensitive to the actual value of τ_0 as long as it is within the range $10 \lessapprox \tau_0 \lessapprox 10^4$, which is the case for the clouds discussed above. In

particular, given the very weak dependency on distance from the quasar of Equation 2.16, τ_0 variations would be of the order of a few. This would result in very similar broadening independent on cloud distance from the quasar.

The resulting integrated spectrum would however depend on the number of clouds encountered by the Lyα photons before escaping the CGM and thus on f_c. If $f_c < 1$, broadening would only happen within the individual clouds. The emerging spectrum would therefore be a convolution of the clouds' velocity dispersion due to their bulk motion and the individual (constant) broadening within individual clouds. The expected effect is thus a flattening of the Lyα observed velocity dispersion profile with respect to the "intrinsic" one. As discussed below, this would imply that the halo masses derived from Lyα velocity dispersion profiles should be considered as upper limits. On the other hand, if $f_c > 1$, the broadening of the emerging spectrum would also depend on the bulk velocity dispersion between different clouds providing a possible mechanism to produce a constant relative broadening. A detailed calculation of the magnitude of the spectral broadening would require detailed radiative transfer simulations. However, radiative transfer effects do not change our results as long as the *shape* of the velocity dispersion profile is not significantly affected by resonant broadening.

In order to empirically understand whether solely the normalisation and not the shape of the velocity dispersion profile is changed, observations of a non-resonant line, such HeII-1640Å (i.e., HeII Hα) are needed. This line is particularly useful for at least three reasons: i) it is a primordial element like hydrogen, thus we expect that both are distributed in the CGM in a similar fashion, ii) its transition wavelength places it in an observable range from the ground with MUSE, iii) for fully doubly ionised Helium, its flux is expected to be relatively bright, i.e. about one third of the Lyα flux for recombination radiation. Unfortunately, as discussed in Cantalupo et al. (2019), HeII emission is typically much fainter than expected for fully, doubly ionised Helium in quasar nebulae suggesting the presence of very dense gas in the CGM. We will return to this point in Paper II. From an observational point of view, this makes HeII nebulae more challenging to detect and indeed they are rarely found in the literature.

To overcome this limitation we have re-examined several MUSE medium-deep ($\sim$ 4h) observations of quasars and optimised the analysis to specifically search for HeII emission. Our optimised methodology, applied to 26 of the 28 quasar nebulae in the MAGG sample (Fossati et al. 2021), where two nebulae are excluded due to being gravitationally lensed and associated with multiple quasars respectively, allowed us to discover 14 individually detected HeII nebulae[6]. The data analysis and results will be presented in detail in Travascio et al. (in Prep.). These HeII nebulae have SB values which are typically about 10 - 20 times fainter than the Lyα SB at the same spatial location, consistent with previous results at lower redshifts (e.g. Cantalupo et al. 2019). The faintness of the emission only allows us to probe CGM kinematics, when HeII is detected, up to about 200 ckpc from the quasars.

[6]We note that the fraction of detected nebulae is mostly determined in the MAGG sample by the data noise properties and in particular by the presence of bright sky lines at the expected HeII wavelengths combined with the intrinsic faintness of the line.

The dispersion typically reaches values between 100 and 150 km/s and in three cases values above 200 km/s. Interestingly, these values are very consistent with the intrinsic velocity dispersion values shown in Figure 2.3. In order to reduce the noise associated with the fainter HeII emission, we compare the median velocity dispersion profiles of both HeII and Lyα emission (using the same subset of sources) instead of the individual profiles. The ratio of these median velocity dispersion profiles is found to be consistent with a constant value of 5.66$\pm$0.68 (where the errors indicate the 25th and 75th percentiles) at every radius at which HeII is detected, i.e. up to 200 ckpc.

In light of the discussion above, this result suggests, in the case of $f_c < 1$, that the Lyα velocity dispersion profile is not significantly flattened with respect to the intrinsic one, or, in the case of $f_c > 1$, that the radiative transfer effects due to multiple clouds along the line of sight do not change the *shape* of the Lyα velocity dispersion profiles. In both cases, this would imply that the Lyα velocity dispersion profiles can be used as direct tracers of the halo kinematics. In the remainder of this work, we will assume for simplicity that this result holds at all radii and for all nebulae.

Finally, we stress that, even in the case of $f_c < 1$, the velocity dispersion measured in emission as discussed here, would still be a good representation of the overall kinematics of the system, instead of the velocity dispersion within individual clouds. This is the case as long as multiple clouds at different radial distances are present within the spatial resolution element. Indeed, assuming $f_v \simeq 10^{-3}$ would imply $l \simeq 370$ pc for a $M_{12} = 1$ halo[7]. The spatial resolution element used in the observations and in the production of mock cubes is of the order of 5 kpc (determined by the seeing). Assuming for the sake of simplicity that the typical line of sight length through the halo is about the same size of the virial radius, we obtain that at least ~ 18 clouds should be contributing to each individual spatial resolution element if $f_c > 0.1$. Although this number is sensitive to the actual (unknown) value of f_v, our order of magnitude estimate is useful in conveying that even a covering below unity plausibly results in a significant number of clouds along the line of sight within the spatial resolution element.

2.2.4 Constraining quasar halo masses

In the previous sections, we have seen that the shape of the normalised Lyα "intrinsic" velocity dispersion profiles is self-similar if represented in units of r/r_{vir} (see Figure 2.4) and can be described by an analytical function (see Equation 2.10). Moreover, through analytical considerations and by comparing to HeII emission observations (for a sub-sample of nebulae), we have shown that this result should also apply to the *observed* Lyα velocity profiles, which differ from the "intrinsic" ones

[7]In reference to the work of Pezzulli & Cantalupo (2019), we note that this value for f_v would be compatible with a cosmological baryon fraction within haloes, quasar photo-heating and Lyα emission produced by recombination radiation, as long as $C_l > 10$. A value of C_l different than 1 would imply that some regions of the emitting clouds should be out of pressure-equilibrium with the ambient medium. We will return to this point extensively in Paper II.

by a renormalisation factor which is independent of radius.

Taking advantage of these results, we present an analytical relation based on the self similarity of the rescaled velocity dispersion profiles, which can be used to constrain the quasar halo masses using the observed Lyα velocity profile *shape* as a function of comoving radial distance from the quasar. To this end, we introduce a new variable representing the ratio of the median velocity dispersion in two concentric annuli

$$\eta_{40-100}^{140-200} \equiv \frac{\sigma_{140-200}}{\sigma_{40-100}} \, , \tag{2.19}$$

where σ_{40-100} is the *median* velocity dispersion of spaxels within the annulus at 40 to 100 ckpc from the quasar, and $\sigma_{140-200}$ is the *median* velocity dispersion within the annulus 140 to 200 ckpc. These annuli have been carefully chosen in order to avoid the central regions (affected by quasar PSF subtraction in observations) and to maximise the velocity dispersion variations across the relevant spatial scales as shown in Figure 2.3. Note that a "flatter" velocity dispersion profile as a function of comoving distance (corresponding to larger halo masses) would have a higher $\eta_{40-100}^{140-200}$ than a steeper profile (corresponding to lower halo masses). At the same time, $\eta_{40-100}^{140-200}$ is independent of any radiative transfer broadening effects, as long as these effects are mostly independent of radius (as argued in the previous sections).

As the function for $\sigma_{rescaled}$ given in Equation 2.10 is monotonic, the median $\sigma_{rescaled}$ within an annulus is simply the value of $\sigma_{rescaled}$ at the radius where half the surface of the annulus is reached. Hence, $\eta_{40-100}^{140-200}$ can be written as

$$\eta_{40-100}^{140-200} = \frac{\sigma(r_{out}/r_{vir})}{\sigma(r_{in}/r_{vir})}. \tag{2.20}$$

We have dropped the subscript *rescaled* from σ for the sake of readability, $r_{out} \sim 172$ ckpc and $r_{in} \sim 76$ ckpc refer to the radii at which the median σ is reached in the two annuli and all radii are in comoving units. With the relation

$$r_{vir} = \left(\frac{M_h \, G}{100 \, H_0^2 \, \Omega_m} \right)^{1/3} , \tag{2.21}$$

which is redshift independent for comoving units within our redshift range of interest[8], the velocity dispersion ratio $\eta_{40-100}^{140-200}$ can be rewritten as

$$\eta_{40-100}^{140-200} = \frac{a \, P \, r_{out}^3 \, \mu^3 + b \, P^{2/3} \, r_{out}^2 \, \mu^2 + c \, P^{1/3} \, r_{out} \, \mu + d}{a \, P \, r_{in}^3 \, \mu^3 + b \, P^{2/3} \, r_{in}^2 \, \mu^2 + c \, P^{1/3} \, r_{in} \, \mu + d}. \tag{2.22}$$

Where $\mu \equiv M_h^{-1/3}$, $P = (100 \, H_0^2 \, \Omega_m)/G = 3.197 \times 10^4$ $\mathrm{M}_\odot$ ckpc^{-3}, G is the gravitational constant, the coefficients a, b, c and d are those of the fitted polynomial in Equation 2.10 and M_h is in units of $\mathrm{M}_\odot$.

[8] In comoving units the mass of a halo can be written as $M_h = 100 r_{vir}^3 \, H_0^2 G^{-1} (\Omega_m + \Omega_\Lambda (1+z)^{-3})$. As Ω_m dominates $\Omega_\Lambda (1+z)^{-3}$ at $z > 2$ one can neglect the second term in the brackets, resulting in the relation quoted in Equation 2.21.

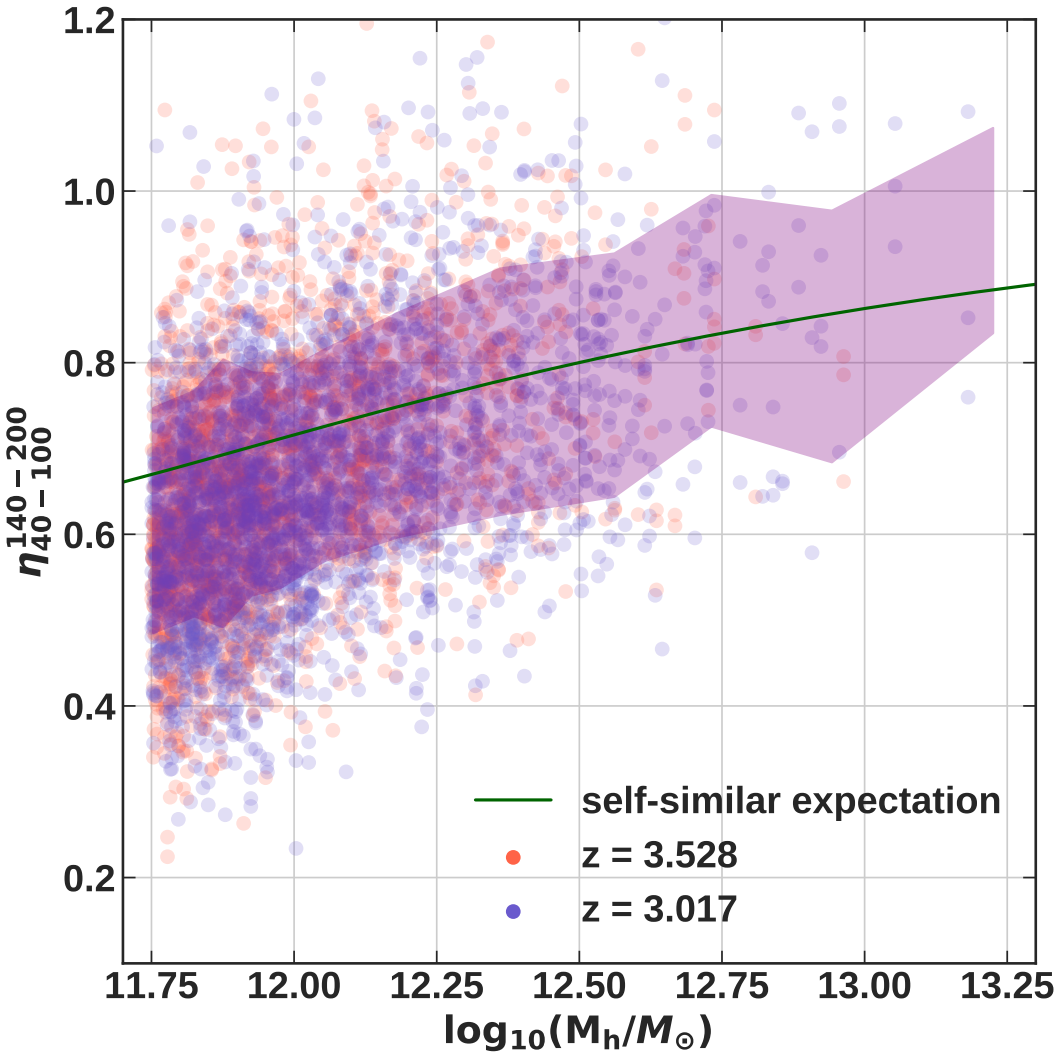

Figure 2.5: The ratio of the median velocity dispersion values in the outer (140 - 200 ckpc) and inner (40 - 100 ckpc) annuli from all three simulations and both redshifts as a function of halo mass. The blue dots refer to $\eta_{40-100}^{140-200}$ at $z \sim 3$, the red dots to $z \sim 3.5$ and the purple shaded region indicates the standard deviation of the individual $\eta_{40-100}^{140-200}$ values as a function of halo mass. The analytical relation based on the self-similarity of the rescaled velocity dispersion profiles given in Equation 2.22 is plotted in green. The values of $\eta_{40-100}^{140-200}$ do not vary with resolution, redshift or feedback implementation, which is why we combine all six simulation snapshots. Despite the significant scatter there is a clear correlation with halo mass as expected from our analytical relation.

In Figure 2.5 we plot the analytically derived $\eta_{40-100}^{140-200}$ given in Equation 2.22 as a function of halo mass (through its relation with the virial radius) in green. We plot the $\eta_{40-100}^{140-200}$ of the individual mock Lyα nebulae to confirm that their $\eta_{40-100}^{140-200}$ scales with halo mass as predicted by Equation 2.22. Additionally, we indicate the region within the standard deviation of the simulated nebulae's $\eta_{40-100}^{140-200}$ as a function of halo mass with the purple shaded region. We emphasise that the analytical relation is based on the self-similarity of the shape of the velocity dispersion profiles which are independent of mass and redshift if represented in units of the virial radius. The large scatter of the individual $\eta_{40-100}^{140-200}$ values in Figure 2.5 is consistent with the scatter in the individual velocity dispersion profiles presented in Figure 2.4 and reflects the systematic effects related to morphological and physical properties of the haloes as discussed in detail in Section 2.4.1. As such, we remind the reader that the analytical $\eta_{40-100}^{140-200}$ versus halo mass function presented here should be seen as a relation valid for a population of haloes rather than for single quasars. The blue dots refer to redshift $z \sim 3$ and the red dots to redshift $z \sim 3.5$. As expected, the values of $\eta_{40-100}^{140-200}$ appear to be largely independent of redshift within the range explored here. Moreover, we have also verified that they are independent of simulation resolution and AGN-feedback implementation.

By varying the Lyα emissivity of each particle (by a constant factor, for simplicity), we have also verified that the analytical relation presented above is independent of the surface brightness normalisation as long as emission is detectable. We refer to Figure C.3 in Appendix C for more details. Moreover, we have also found that $\eta_{40-100}^{140-200}$ is largely independent of the spectral resolution of the mock cubes as long as it is high enough to resolve the typical width of the "intrinsic" velocity dispersion value (which is typically the case for MUSE within the considered spatial annuli). Because the velocity dispersion should decreases with increasing distance from the halo centre, the values of $\eta_{40-100}^{140-200}$ are expected to be lower than 1, as is the case for the analytical $\eta_{40-100}^{140-200}$ plotted in Figure 2.5. However, as is evident from Figure 2.5 there are some individual instances of $\eta_{40-100}^{140-200}$ that have values larger than 1, implying a larger velocity dispersion at larger distances from the quasar. This can be attributed, e.g., to the superposition along the line of sight of multiple halos separated by hundreds of kpc or a few Mpc which are, however, spectrally blended with the quasar Lyα nebula. These projection effects are expected to happen, in a statistical sense, both in our mock observations and in real data (see Cantalupo et al. (2019) for a discussion of one of these possible cases associated with the Slug Nebula).

We propose using the function given in Equation 2.22 to constrain the mass of haloes hosting observed Lyα nebulae powered by bright quasars based on their measured $\eta_{40-100}^{140-200}$. Theoretically, the $\eta_{40-100}^{140-200}$ value of a sample with a given mass distribution can be expressed as

$$\eta_{40-100}^{140-200} = \frac{\int_0^\infty \eta(M_h)\, P(M_h)\, n(M_h)\, dM_h}{\int_0^\infty P(M_h)\, n(M_h)\, dM_h}, \tag{2.23}$$

where $P(M_h)$ is the mass dependent probability of a halo hosting a bright quasar and is $n(M_h)$ is the halo mass function. Following the standard procedure used in quasar

clustering studies, e.g. Eftekharzadeh et al. (2015), we use two possible functional shapes for $P(M_h)$: i) a delta function (which thus defines a "characteristic" halo mass) and, ii) a step function (which defines a "minimum" halo mass) as described in detail below. We stress, however, that any shape of $P(M_h)$ can in principle be used in combination with our method. Thus, we define the characteristic halo mass M_h of a sample of Lyα nebulae as the halo mass for which the analytical $\eta_{40-100}^{140-200}$ in Equation 2.22 corresponds to the measured $\eta_{40-100}^{140-200}$ of the sample. Additionally, a minimum halo mass M_{min} can be derived by assuming that $P(M_h)$ is a step function for which $P(M_h) = 1$ for $M_h > M_{min}$ and zero otherwise. In the latter case, we interpret the measured $\eta_{40-100}^{140-200}$ as the mean $\eta_{40-100}^{140-200}$ of all haloes with masses above M_{min}, weighted by the halo mass function (see Equation 9, Eftekharzadeh et al. 2015).

In the following sections, we apply our method to a subset of observed MUSE Lyα nebulae around bright quasars at $3 < z < 4$ and provide constraints on the characteristic and minimum halo masses of the samples based on the CGM kinematics.

2.3 Application of Mass estimation method

As a first application of the method presented above, we use the analytical relation given in Equation 2.22 to constrain the characteristic mass of haloes hosting bright quasars and surrounding Lyα nebulae presented in the first MUSE GTO survey around bright quasars (MUSE Quasar Nebulae snapshot survey, or MQN) (Borisova et al. 2016) and those included in the MAGG sample (Lofthouse et al. 2020; Fossati et al. 2021). These nebulae are extended enough and have sufficiently high SNR to be excellent candidates for our mass estimation method.

2.3.1 The observed Lyα nebula samples

The Lyα nebulae sample presented in Borisova et al. (2016) is comprised of two sub-samples, observed during the two different MUSE GTO programs: 094.A-0396, 095.A-0708, 096.A-0345 PI: S. Lilly & 094.A- 0131, 095.A-0200, 096.A-0222 PI: J. Schaye. We solely consider the first sub-sample (094.A-0396, 095.A-0708, 096.A-0345), which consists of 12 of radio-quiet quasars within the redshift range $z \approx 3.0 - 3.3$. For the sake of brevity we refer to this sub-sample as the MQN $z \sim 3.1$ sample. We note that a handful of the nebulae in the higher redshift sub-sample (094.A- 0131, 095.A-0200, 096.A-0222) are included in the MAGG sample. Relevant for this analysis is that the observed quasars are some of the brightest known radio quiet quasars within the redshift range considered.

We calculate the velocity dispersion ratio $\eta_{40-100}^{140-200}$ for 10 of the 12 Lyα nebulae using the velocity dispersion maps obtained as discussed in Borisova et al. (2016) and presented in Figure 7 of that work[9]. When calculating the velocity dispersion

[9]It is worth noting that although Figure 7 in Borisova et al. (2016) shows the FWHM, they calculate the FWHM by using the relation $2.35 \times \sigma$. Therefore these values could be directly used

ratio $\eta_{40-100}^{140-200}$ for the extracted nebulae, we require that at least 20% of spaxels in the outer annulus have a velocity dispersion measurement. Due to this requirement, one nebula (MQN17) is excluded from our analysis. We further exclude another nebula (MQN07) as its SB peak does not spatially coincide with the quasar, possibly suggesting that the quasar could be hosted by a companion or satellite galaxy not located at the halo centre. This is different than our mock observations for which, by construction, the quasar is placed at the centre of mass of the host halo. As a consequence, all distances relevant for our empirical relations are calculated with respect to the centre of the halo, making our mass estimation method likely unsuitable for observed nebulae with clear displacements between quasar position and the SB spatial peak. This issue could be solved by changing the definition of halo centre in observed nebulae to the SB spatial peak. For simplicity however, in this first analysis, we have excluded the peculiar nebula MQN07.

The MAGG sample is introduced and described in detail in Lofthouse et al. (2020) & Fossati et al. (2021), here we briefly summarise the aspects relevant to this work. The sample consists of 28 quasars for which archival high-resolution (R$\gtrsim$ 30 000) spectroscopy is available, with m$_r$ ¡ 19 AB mag covering a redshift range of $z \approx 3.2 - 4.5$. The selection criteria for the quasars require that these are observable from the VLT with low airmass, and have at least one intervening strong hydrogen absorption line system at $z > 3.05$ with $N_{\rm HI} > 10^{17}{\rm cm}^{-2}$. The original extraction and detection of Lyα nebulae in Fossati et al. (2021) is performed with `CubEx` imposing a SNR threshold of 2.0 and a minimum number of connected voxels of 1000. We note that one of the Lyα nebulae is excluded from the analysis in Fossati et al. (2021), due to it being strongly lensed and thus exhibiting an irregular morphology. The sample can be split into a high and low redshift sub-samples with median redshifts of $z \sim 4.1$ and $z \sim 3.5$ respectively. We apply our mass estimation method to each redshift sub-sample separately and to the whole sample combined with the MQN sample in order to investigate any potential redshift evolution of the typical mass of halo hosting a quasar.

2.3.2 Characteristic quasar halo masses as a function of redshift

We calculate the median $\eta_{40-100}^{140-200}$ of the three samples described in Section 2.3.1. This results in the following values: 0.755, 0.744 and 0.736 for the MAGG $z \sim 4.1$, $z \sim 3.5$ and MQN $z \sim 3.1$ samples respectively. In Figure 2.6 we indicate the individual $\eta_{40-100}^{140-200}$ values of each Lyα nebula with vertical ticks. The top three panels refer to the three samples separately and the bottom panel refers to the combination of all three samples. In each panel the median of the samples is marked with a solid vertical grey line. We use the median of each $\eta_{40-100}^{140-200}$ distribution and Equation 2.22 to obtain a characteristic quasar halo mass for each sample as outlined in Section 2.2.4. We estimate the uncertainties of the characteristic halo mass by means of a bootstrap estimate. We randomly re-draw a population of

as our method requires sigma modulo any constant multiplicative factor.

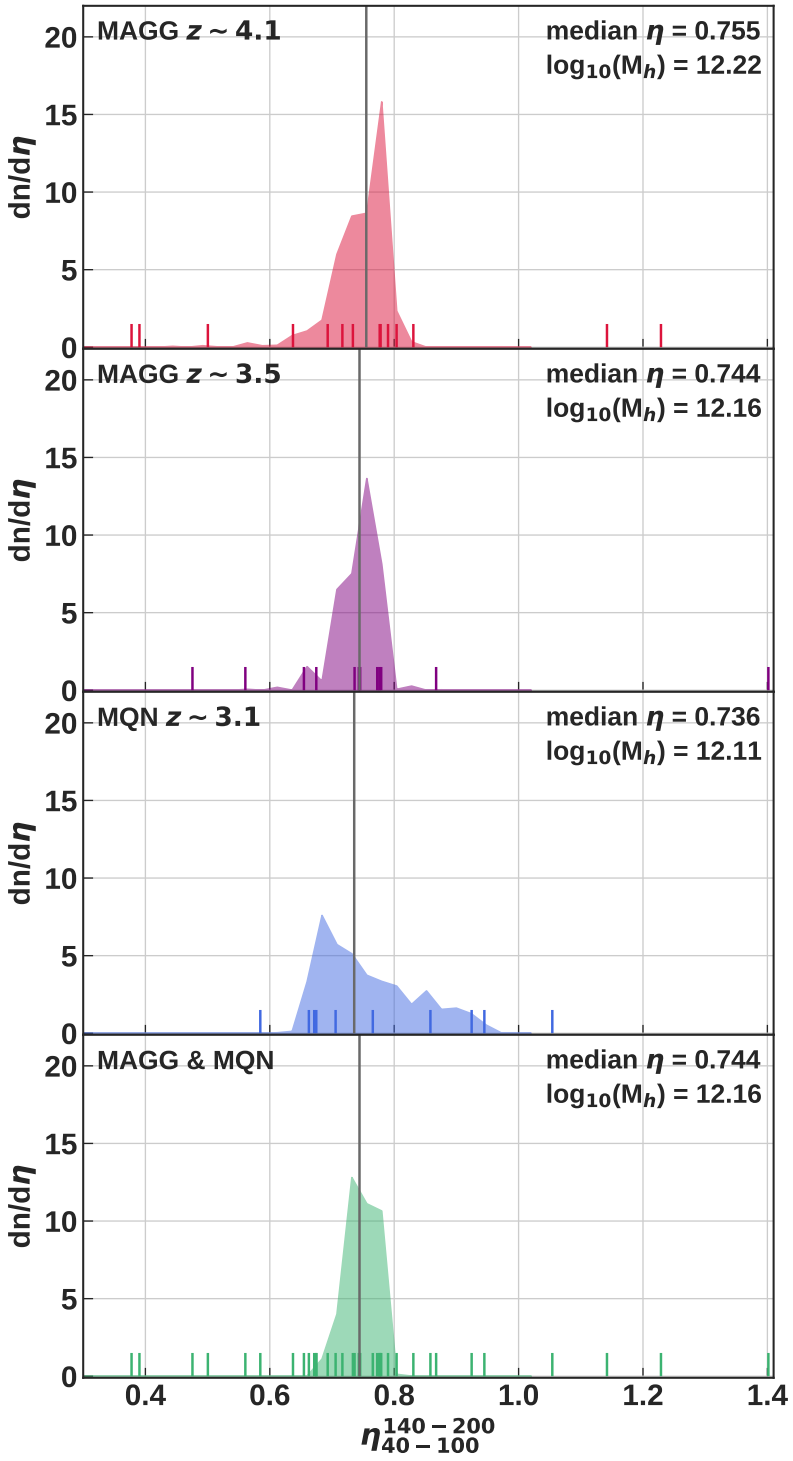

Figure 2.6: Starting from the top, the panels refer to the MAGG $z \sim 4.1$, $z \sim 3.5$, MQN $z \sim 3.5$ and to all three samples combined. In each panel the vertical ticks indicate the $\eta_{40-100}^{140-200}$ of the individual Lyα nebulae included in the analysis and the shaded region refers to the distribution of medians of the randomly redrawn samples normalised such that the integral of the area equals one. The samples respective median $\eta_{40-100}^{140-200}$ are marked with a vertical, solid line. The characteristic halo mass for each sample as obtained using our analytical relation (Equation 2.22) is quoted in each panel.

$\eta_{40-100}^{140-200}$ values from each observed sample 10000 times and calculate the median of each random population. The shaded region in each panel of Figure 2.6 indicates the distribution of these medians, normalised so that the integral of the distributions is one. We calculate the standard deviation of these 10000 median $\eta_{40-100}^{140-200}$ values and quote this standard deviation as the uncertainty of our mass estimates. The decadic logarithms of the obtained quasar halo mass estimates in units of $M_\odot$ are thus $12.22^{+0.28}_{-0.25}$, $12.16^{+0.18}_{-0.17}$ and $12.11^{+0.47}_{-0.42}$ for the MAGG $z \sim 4.1$, $z \sim 3.5$ and MQN $z \sim 3.1$ samples respectively. We use the median $\eta_{40-100}^{140-200}$ of the samples instead of the mean to limit our sensitivity to outliers. We stress, however, that using the mean instead of the median would result in halo mass estimates that are consistent to the above values within their errorbars. In particular, calculating the characteristic masses from the mean would result in halo mass estimates with decadic logarithms of $12.15^{+0.28}_{-0.25}$, $12.28^{+0.19}_{-0.18}$ and $12.40^{+0.59}_{-0.44}$ for the three samples (in order of decreasing redshift). We compare the measured $\eta_{40-100}^{140-200}$ values of the individual Lyα nebulae in the MAGG $z \sim 3.5$ sample to the number of Lyα emitters (LAEs) in each MUSE field as reported by Fossati et al. (2021) and find evidence for a weak correlation (see Appendix E), which strengthens our results.

Despite the relative broadness of the observed $\eta_{40-100}^{140-200}$ distributions, the median values of $\eta_{40-100}^{140-200}$ are very much consistent with each other, independent of redshift. Combining all three redshift ranges results in an almost symmetrical distribution of $\eta_{40-100}^{140-200}$ around a median of 0.744. We therefore obtain a characteristic halo mass with a decadic logarithm of $12.16^{+0.14}_{-0.13}$ ($12.26^{+0.15}_{-0.14}$ if we use the mean $\eta_{40-100}^{140-200}$ of the combined samples instead). In addition to calculating the characteristic halo masses of the observed samples, we also calculate the minimum halo mass following the procedure described in Section 2.2.4 and Eftekharzadeh et al. (2015). The decadic logarithms of the minimum halo masses obtained in this way are: 12.04, 11.94, 11.87 and 11.94 respectively for the MAGG $z \sim 4.1$, $z \sim 3.5$, MQN $z \sim 3.1$ samples and for all samples combined.

Characteristic halo masses as large as $10^{13} M_\odot$ are thus clearly outside our 1σ confidence interval at $3.1 < z < 4.5$. This result, combined with the other literature measurements presented in Figure2.7, has important implications for the derivation of the CGM physical properties, such as emitting gas densities and clumpiness as will be discussed in detail in Paper II (see also discussion in Pezzulli & Cantalupo (2019)). Moreover, this result has important implications when compared to other quasar host halo mass measurements, e.g. from clustering as discussed in Section 2.4.3.

2.4 Discussion

With the help of cosmological simulations and Lyα nebulae observations at $z > 3$, we have shown that it is possible to derive new constraints on quasar halo masses from the CGM kinematics that are complementary to quasar clustering measurements. Despite the model uncertainties and statistical limitations due to the size of the observed samples used in this work, these constraints have the potential to provide a

new view of the host halos of quasars, their environment and thus of CGM properties. In Section 2.4.1 we give an overview of the limitations of the halo mass estimation method presented here. In particular, among the possible model uncertainties, we discuss the effect of the AGN feedback implementation in EAGLE on our results in Section 2.4.2. Finally, in Section 2.4.3 we put our method into a broader context by comparing it and the derived mass estimates to other estimates and methods.

2.4.1 Limitations of our method

As is evident from Figures 2.4 and 2.5, there is a relatively large scatter of the simulated velocity dispersion profiles and ratios $\eta_{40-100}^{140-200}$. Such a large scatter stems both from systematic effects related to morphological and physical properties of the haloes and, partly, from the noise associated with the (mock) measurements themselves. Indeed, realistic halo shapes are far from simple spheres and radial inflows may occur along a few filaments coming from various directions (Bond et al. 1996; Kereš et al. 2005). As such, the same halo as seen from different directions could have different radial profiles of the line of sight velocity dispersion as measured in emission. In addition, realistic haloes do not live in isolation: projection effects due to multiple haloes along the line of sight (as discussed in Section 2.2.4) can artificially increase the velocity dispersion. Because these effects are aleatory and, in principle, independent of the quasar host halo mass, the error on the median halo mass of a sample of quasars could be decreased by increasing the sample size. As a first application, we have used a relatively limited sample of MUSE Lyα nebulae around quasars for which we had access to the velocity dispersion maps. A much larger dataset is already available and in principle our analysis could be repeated using a larger sample. Moreover, the ubiquity of Lyα nebulae around quasars at all redshift explored so far ($z > 2$) provide the opportunity to extend the redshift range and plan for dedicated surveys targeting a much larger number of quasars.

Observational limitations are related to the necessary SNR required to measure the line of sight velocity dispersion at a given distance from the quasar. Because the method presented here is based on the value of $\eta_{40-100}^{140-200}$, observable emission should extend to at least 200 ckpc from the quasar. While this is the case for the majority of bright quasar nebulae discovered so far, fainter quasars and quasars at higher redshifts more often have smaller detectable nebulae (Farina et al. 2019; Mackenzie et al. 2021) at a given SB sensitivity level. As long as these quasars are "illuminating" gas on large scales, this issue can be solved by increasing the exposure time of the observations.

We have proposed the use of the Lyα emission as a tracer of the shape of the velocity dispersion profile given the brightness of this line which makes it easily detectable on large scales even in short exposure times. However, as discussed in detail in section 2.2.3, this is a resonant line which may suffer from radiative transfer broadening. We have argued, based on analytical considerations and on complementary HeII-Hα observations for a subsample of quasar nebulae, that the Lyα broadening with respect to the "intrinsic" velocity dispersion should be independent of distance, making our method based on $\eta_{40-100}^{140-200}$ independent of Lyα broadening. In the model

presented in Section 2.2.3, a series of simplified assumptions have been made, for instance, that the quasar ionising radiation is isotropic and that the whole CGM is thus ionised. However, some observations suggest that this is not the case, at least for quasars which are around 2-3 mag fainter than the sample studied here (Prochaska et al. 2013), and that part of the transverse direction is not ionised by the quasar. While we have verified that this does not affect our result based on the "intrinsic" velocity dispersion (for an opening angle at least as large as 60°), this could have an effect on the broadening of the Lyα emission produced on the far side of the quasar halo. For ionising cones as expected from the AGN unification model (e.g. den Brok et al. 2020), this would possibly imply a larger broadening at larger distances from the quasar. In this case, our estimate should be considered an *upper limit* on the quasar halo mass.

Lastly, it is worth stressing that our results are based on the fact that the kinematics of the cold emitting gas is *on average* determined by gravity only and thus by the host halo mass to a high degree, as derived and demonstrated using the EAGLE and ENGINE simulations. However, different assumptions, e.g., concerning galaxy feedback, or missing physics in these simulations could lead to a different result, i.e. to different cold gas kinematic patterns and radial velocity dispersion profiles. For instance, if galactic feedback is preferentially increasing the velocity dispersion of the emitting gas closer to the centre of the haloes, then the actual values of $\eta_{40-100}^{140-200}$ would be *lower* than predicted from pure gravitational effects. This would imply that the actual halo mass could be higher than predicted by from our model. This scenario can however be excluded by looking at the *absolute* value of the velocity dispersion in the inner annulus used in our analysis as measured through a non-resonant line, such as HeII-Hα emission. In particular, the values measured in the MAGG sample by Travascio et al. (in Prep.) and discussed in Section 2.2.3 are of the order of 100 km/s which is very much consistent (or slightly below) the intrinsic velocity dispersion in the mock observations presented here (see Figure 2.2.3). Future Hα observations, e.g. with JWST, will test this hypothesis. With the data available up until now we then find it very implausible that the actual masses of the quasar host haloes are *significantly larger* than what is found in this work.

2.4.2 The impact of AGN feedback on CGM kinematics

Though not the main focus of this work, we take advantage of the different implementation of feedback in the EAGLE simulations to verify the possible effect of AGN feedback on the overall CGM kinematics (and thus also on our halo mass estimate). In particular, in this section, we compare the radial velocity profiles obtained from the NoAGN and RECAL simulations (see Table 2.1). For haloes in the three highest mass bins contained in these two simulations the inclusion of AGN-feedback leads to higher maximum outflow velocities of the hot gas in the radial velocity profiles. The radial velocity profiles of the Lyα emitting gas, however, are not affected by the inclusion of AGN-feedback and there is no significant difference between the radial profiles obtained from the NoAGN and the RECAL simulations at either redshift as can be seen in Figures D.4 and D.5 in Appendix D. This is likely due to the

fact that, as mentioned in Section 2.2.3, the Lyα emitting gas roughly corresponds to the cool gas ($\lessapprox 10^5 K$). The low temperature of the gas implies that it has not been significantly heated by feedback processes. Indeed, the hot gas ejected from the galaxy due to the AGN-feedback (as implemented in EAGLE) is expected to take the path of least resistance and therefore flows out of the galaxy via the regions with lower densities, without interacting with the cold and dense accreting filaments (see also van de Voort et al. (2011b)). As such, the presence of AGN feedback, at least as implemented in EAGLE, has little effect on our halo mass estimates based on $\eta_{40-100}^{140-200}$.

We stress however that AGN feedback implementation is still highly debated in the literature. While works based on EAGLE-like simulations, e.g. Rahmati et al. (2015), or other simulations such as SIMBA (Davé et al. 2019) typically found that the HI distribution in the CGM, traced via mean Lyα flux fluctuation profiles at high redshift, is not affected by the presence of AGN-feedback (e.g. Sorini et al. 2020), other works, such as Costa et al. (2022), suggest that AGN feedback can also have an effect on the cold CGM component, at least at very high redshift ($z > 6$). From an observational view-point, the situation is also not clear. While extended emission around radio-galaxies and radio-loud quasar have often been associated with outflows (Villar-Martín et al. 1999; Silva et al. 2018) given the large velocity dispersion values (> 600 km/s) found in non-resonant emission lines, the large majority of radio-quiet nebulae discovered around quasars at $z > 2$ present relatively quiet kinematics consistent with gravitational motion only, e.g., in HeII-Hα as we have discussed in Section 2.2.3 (see also Cantalupo (2017) for a review). The discriminating factor could be the presence of a radio-jet on CGM scales which certainly has the potential to inject energy and momentum, possibly also affecting the cold CGM component. It could thus be interesting to apply our methodology to a sample of radio-loud quasars and galaxies in the future and compare the *intrinsic* velocity dispersion profiles to search for AGN feedback effects, assuming, e.g., that radio-loud quasars live in similar haloes with respect to their radio-quiet counterparts. Unfortunately, radio-loud AGN are much rarer and thus a specific sample should be built for this purpose. We note that, especially for radio-galaxies, a non-resonant line (e.g., hydrogen or helium Hα) is necessary for this analysis since Lyα broadening could be different for these systems. This would be the case, for instance, if the ionisation cone of these AGN is oriented along the plane of the sky rather than along our line-of-sight as for quasars.

2.4.3 Comparison to other halo mass estimation methods

Typical methods currently used to estimate the mass of the haloes hosting quasars are based on clustering and include, in particular, quasar auto-correlation (QSO-clustering studies) (Shen et al. 2007; da Ângela et al. 2008; Shen et al. 2009; Eftekharzadeh et al. 2015; Timlin et al. 2018) or quasar-galaxy cross-correlation studies (Trainor & Steidel 2012; Font-Ribera et al. 2013; He et al. 2017). In some recent works, kinematics of galaxies and some simplified treatment of Lyα emission kinematics have also been used to put some constraints for quasars at $z > 2$ (Lau

et al. 2018; Arrigoni Battaia et al. 2019a; Fossati et al. 2021). In this section, we compare these results to those obtained by applying the method developed here to the MAGG and MQN samples as detailed in Section 2.3.2.

We stress that, due to the differences in sample sizes and redshifts it is not trivial to compare our mass estimates with those obtained measuring the quasar auto-correlation or quasar-galaxy cross-correlation functions. Furthermore, these differences and additional caveats, such as the modelling of nonlinear scales and the inclusion of Poisson shot-noise, also make it non-trivial to compare the results obtained using correlation functions with each other. Despite this, we give a qualitative comparison of the quasar halo mass estimates obtained in this study and those from QSO-clustering studies and quasar-galaxy cross-correlation studies in Figure 2.7. Our results and their uncertainties for the redshifts $z \sim 3.1$ (MQN sample), $z \sim 3.5$ & $z \sim 4.1$ (MAGG sample) are indicated with yellow stars and red error bars. The characteristic mass and associated uncertainties for the three samples combined is plotted with a yellow star and grey error bars. Mass estimates and their uncertainties obtained with QSO-clustering are plotted with circles and green error bars, the results from quasar-galaxy cross-correlation studies are indicated with squares and blue error bars. The colours of the individual markers refer to each individual piece of work.

Our inferred halo mass is lower than the mass estimate of quasar hosting haloes obtained from QSO clustering studies performed at comparable redshifts by Shen et al. (2007) ($z \sim 3$ and $z \sim 4.3$, blue circle and green error bars) & Timlin et al. (2018) ($z \sim 3.5$, orange circle and green error bars). Eftekharzadeh et al. (2015) (pink circles and green error bars) use a far larger sample, which they divide into three redshift sub-samples, with the two higher redshift bins being most compatible with the quasars used in our analysis. Their mass estimate for the $z \sim 3$ bin is lower than our mass estimate, while their mass estimate for the $z \sim 2.5$ redshift bin is consistent with our results. The fact that clustering studies do not include Poisson shot-noise and only use a linear bias relation while fitting the correlation function also on (mildly) nonlinear scales could lead to an overestimation of the bias and hence of the haloes masses. The first effect is mitigated with increasing sample size and could explain why Shen et al. (2007) & Timlin et al. (2018) find higher halo masses.

Our mass estimates are in very good agreement with those obtained from quasar-galaxy cross-correlation reported in Figure 2.7. These include the work of Trainor & Steidel (2012) (dark orange square and blue error bars), in which they calculate the quasar-galaxy cross-correlation function for a sample of 15 hyper-luminous quasars and the surrounding galaxies that lie within 4.2 h^{-1}cMpc at redshifts $2.5 < z < 2.9$, as a part of the Keck Baryonic Structure Survey (KBSS) (Steidel et al. 2014). Comparing the observed cross-correlation function to the galaxy-quasar cross-correlation function of simulated halo populations while varying masses of both the simulated quasar haloes and surrounding galaxy haloes they find that the hyper-luminous quasars are hosted by haloes with a median mass of $10^{12.3\pm0.5} M_{\odot}$. Font-Ribera et al. (2013) ($z \sim 2.38$, dark blue squares and blue error bars) measure the cross-correlation function of quasars from the Baryon Oscillation Spectroscopic Survey

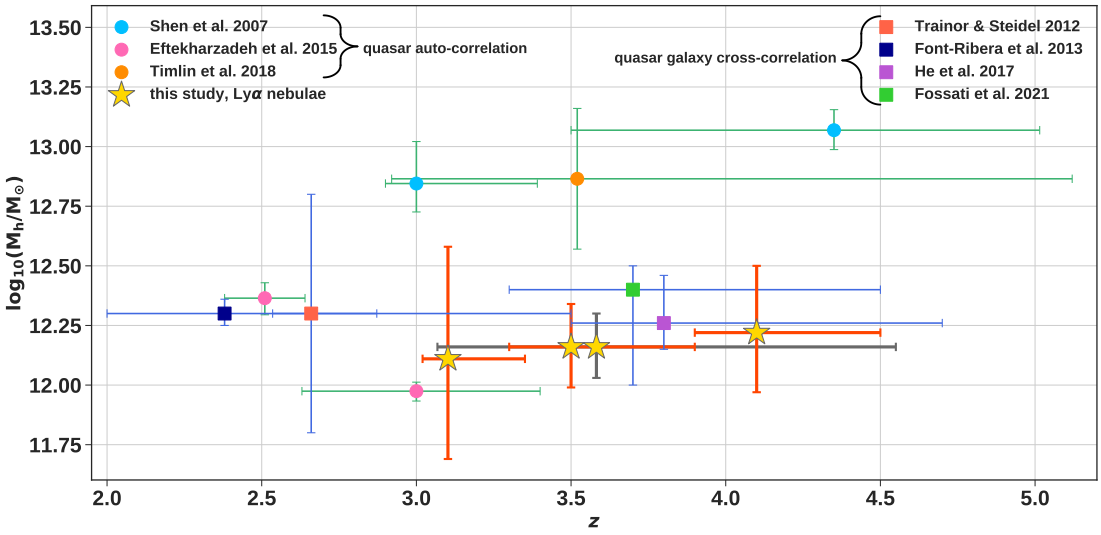

Figure 2.7: Comparison of our quasar host halo median mass estimates for the MQN $z \sim 3.1$, $z \sim 3.5$, $z \sim 4.1$ MAGG samples (yellow stars with red error bars) and those three samples combined (yellow stars with grey error bars) with quasar halo mass estimates obtained from QSO-clustering studies (circles with green error bars) and galaxy-quasar clustering studies (squares with blue error bars), as reported in the legend (see Section 2.3.2). All horizontal errorbars denote the redshift range of the quasars included in the different studies. The vertical errorbars denote the halo mass range for each sample. For some studies (He et al. (2017), Timlin et al. (2018) & Fossati et al. (2021)), only a halo mass range and not a characteristic mass are given. In this case, we centre the errorbars on the averaged halo mass within the quoted mass range for visualisation purposes. The characteristic quasar halo mass and mass range of the quasar sample presented in Shen et al. (2007) & Font-Ribera et al. (2013) are taken from Eftekharzadeh et al. (2015). At $z \sim 3$ our measurements are consistent with the quasar auto-correlation constraints presented in Eftekharzadeh et al. (2015), which conflict with those presented in Shen et al. (2007). Our method, which is independent of clustering studies, thus suggest that (bright) quasar are typically hosted by $10^{12.16}$ $M_\odot$ haloes, independent of redshift in the range $3 < z < 4$. See section 2.4.1 for a detailed discussion of the strength and limitation of our methods and the possible implication of this results.

(BOSS) (Dawson et al. 2013) and the Lyα forest absorption in redshift space. They measure bias factors consistent with auto-correlation measurements at comparable redshifts. He et al. (2017) ($z \sim 3.8$, purple square and blue error bars) use a combination of two quasar samples totalling 1'243 quasars and 25'790 bright $z \sim 4$ Lyman break galaxies to calculate a quasar-galaxy cross-correlation function and derive the bias by comparing the measured clustering strength to that of the underlying dark matter based on linear structure formation theory. From this bias they derive a halo mass range of $10^{12.15} M_\odot$ - $10^{12.46} M_\odot$.

Our estimate is also consistent with that obtained by Fossati et al. (2021) for the same MAGG sample used in this work. In particular, these authors calculate the quasar-galaxy cross-correlation function for the MAGG sample's 28 quasars and

113 LAEs. However, this measurement is not used to constrain the quasar halo masses as the small field of view of the MUSE instrument prevents the inclusion of larger scales, thus hampering the conversion of the cross-correlation function into a bias and quasar halo mass. Instead, they constrain the quasar halo masses in the MAGG sample by calculating the overdensity of LAEs around the MAGG quasars and comparing this overdensity to that of galaxies around the 15 hyper-luminous quasars from the KBSS calculated in Trainor & Steidel (2012). As the two galaxy overdensity values are consistent with one another, Fossati et al. (2021) deduce that the quasar halo masses in the MAGG sample are likely also consistent with those calculated in Trainor & Steidel (2012) using the quasar-galaxy cross-correlation function. Fossati et al. (2021) further evaluate the velocity offset of the LAEs with respect to the nebulae's redshift. They compare the kinematic dispersion of these galaxies with that of galaxies in the same line of sight velocity window centred on haloes with a mass of $M_h \sim 10^{12.4} - 10^{12.6}$ $M_\odot$ from the Millennium simulation (Springel et al. 2005), finding that the observed kinematic dispersion is consistent with a typical halo mass of $10^{12.5}$ $M_\odot$. Based on these two comparisons, Fossati et al. (2021) derive a quasar halo mass estimate of $10^{12} M_\odot$ - $10^{12.5} M_\odot$. Although this estimate is not strictly based on the quasar-galaxy cross-correlation function, we still include it in our comparison in Figure 2.7 for the sake of completeness. It is plotted with a green square and blue error bars.

We note that combining the halo mass estimates of the MQN sample at $z \sim 3.1$ and the MAGG sample with that of the KBSS would imply a negligible evolution of bright quasar hosting halo masses from $z \sim 2.7$ to $z \sim 3.7$. This is consistent with a negligible halo mass evolution within the MAGG sample from $z \sim 3.5$ to $z \sim 4.1$ already mentioned in Section 2.3.2 and could have significant implications for our understanding of quasar formation and evolution. However, this interpretation needs additional confirmation as additional effects, such as selection biases affecting both samples, could be responsible for the apparent non-evolution of the mass of haloes hosting bright quasars.

Finally, it is interesting to compare our method to the analysis performed by Arrigoni Battaia et al. (2019a) on their sample of 61 quasar Lyα nebulae as a part of the MUSEUM survey. In particular, they calculate the spatial average of the Lyα velocity dispersion over the whole area in which the emission is detected ($< \sigma_{\mathrm{Ly}\alpha} >$) quoting a value of $\sigma_{Ly\alpha} < 400$ km s^{-1} (and typical values around 250 km s^{-1} according to their Figure 11). Assuming a NFW profile (Navarro et al. 1997) and a concentration of $c \sim 3.7$ at $z \sim 3$, they estimate that a halo with a mass of $10^{12.5}$M$_\odot$ should have a maximum circular velocity of $v_{circ}^{max} = 360$km s^{-1}. Further assuming that the velocity dispersion obeys $\sqrt{2}\,\sigma_{1D\,rms} = v_{circ}^{max}$ (Tormen et al. 1997), they infer $\sigma_{1D\,rms} \simeq 250$km s^{-1}, which they note is similar to their $< \sigma_{\mathrm{Ly}\alpha} >$, implying a similar halo mass to the one obtained using our method. We note that, given that the MUSEUM survey is shallower in exposure time with respect to MAGG (40 minutes vs a typical exposure time of 4 hours) and the MQN sample (1 hour exposure time), nebulae in this survey are typically detected up to smaller distances from the quasars with respect to these other surveys. The median maximum extent of the nebulae in the MUSEUM survey is indeed around

170 ckpc, thus the $< \sigma_{\mathrm{Ly}\alpha} >$ typically represent only the inner regions of the nebulae. However, because the area changes for each nebula and because of the large spatial averaging it is not easy to translate their $< \sigma_{\mathrm{Ly}\alpha} >$ in any of the quantities used in this work, such as the median velocity dispersion in our inner and outer annuli (which are defined at fixed comoving distances from the quasars). Given the large differences between our method and the approach used by Arrigoni Battaia et al. (2019a), it therefore possible that this agreement is partially coincidental. We have seen that Lyα broadening significantly increases the observed line widths compared to non-resonant emission, such as HeII-Hα, making it non-trivial to directly convert the absolute Lyα velocity dispersion values to a measurement of the gas's intrinsic kinematics. Farina et al. (2019) also apply this analysis to the 12 Lyα nebulae at $z > 5.7$ detected by them and measure an average 1D rms velocity dispersion of $\sigma_{1D\,rms} \simeq 340 \pm 125$km s^{-1}, which is consistent with the gravitational motions in a $10^{12.5}$M$_{\odot}$ halo at $z = 6$. Although the caveats mentioned above also apply to the comparison of our results with those obtained by Farina et al. (2019), taken together these results support a link between the Lyα kinematics and dark matter halo mass even at higher redshifts.

2.5 Conclusion

The discovery of ubiquitous Lyα emission from the CGM and IGM around quasars at $z > 2$ gives us the unique opportunity to constrain the physical properties of gas around galaxies directly through emission, provided that the quasar host halo mass is known (e.g. Pezzulli & Cantalupo 2019). Unfortunately, current constraints on quasar host halo masses given by clustering studies (e.g. using SDSS Shen et al. 2007; Eftekharzadeh et al. 2015) exhibit significant discrepancies at $z \simeq 3$ (see Figure 2.7), the redshift at which most Lyα nebulae have been discovered so far.

We develop a new method to constrain quasar halo masses based on the kinematics of the cold (T $< 10^5$ K), Lyα emitting CGM. By using the cosmological simulations EAGLE and ENGINE (Schaye et al. 2015), we first show in Section 2.2.3 that the kinematics of cold Lyα emitting gas in the CGM of massive haloes ($\mathrm{M}_h > 10^{11.75}M_{\odot}$) should directly depend on the total halo mass, rather than galactic feedback over the scales of interest for Lyα nebulae observations. In particular, we find that the radial velocity profiles of cold emitting gas (Lyα-emissivity-weighted) closely follow the radial velocity profiles of the dark matter, at least in the EAGLE and ENGINE simulations (Figure 2.2) at distances between roughly 1.5 and 5 virial radii from the ionisation of haloes in the mass range $10^{11.75}$M$_{\odot}$ - $10^{13.25}$M$_{\odot}$. At distances below 1.5 virial radii from the halo centre the Lyα emitting gas is predominantly inflowing.

With the aim of exploiting this result, we generate mock MUSE-like observations of Lyα emission from massive haloes in EAGLE and ENGINE under the assumption of maximally fluorescent emission due to bright quasar ionisation (see Sections 2.2.2 & 2.2.2), including sky background noise, atmospheric smoothing and the finite MUSE spectral resolution. The mock observations are then analysed with the same

software as is used for MUSE observations, producing first and second moment maps of the flux distribution (Section 2.2.2). These maps are then used to generate the *intrinsic* velocity dispersion profiles of the Lyα emission (i.e., without considering the effect of resonant broadening) as a function of projected distance from the quasar, a quantity which can be directly compared to observations. We find that, once rescaled by the virial radius and normalised to the value of the central velocity dispersion, these profiles become self-similar (Figure 2.4), demonstrating that they could be used to derive a constraint on the virial radius of the associated halo and thus on its total mass.

Taking advantage of this self-similarity, we define a new variable which can be directly measured in observations and used to derive the halo mass: the velocity dispersion ratio $\eta_{40-100}^{140-200}$. This variable represents the ratio of the median velocity dispersion values in two concentric annuli (40-100 and 140-200 ckpc). These annuli have been carefully selected to maximise the $\eta_{40-100}^{140-200}$ variation across the expected halo mass range associated with quasars (10^{12}M$_\odot$ and 10^{13}M$_\odot$ Shen et al. 2007; Eftekharzadeh et al. 2015; Timlin et al. 2018), while at the same time excluding the inner regions typically affected by the quasar PSF in observations. More importantly, in Section 2.2.3, we show that the value of $\eta_{40-100}^{140-200}$ is unaffected by the radiative transfer spectral broadening associated to resonant Lyα emission. This result is obtained by comparing the observed HeII-Hα velocity dispersion values to the Lyα velocity dispersion values for a subset of quasars for which both measurements are available (see Section 2.2.3).

As a first application of our new methodology, we apply our analytical relation based on the self-similarity of the velocity dispersion profiles to 37 Lyα nebulae observed at $3 < z < 4.5$ as part of the MAGG (Fossati et al. 2021) and MQN (Borisova et al. 2016) surveys. As is typically done in clustering analysis studies, we derive a characteristic halo mass and a minimum halo mass for each of our quasar samples, obtaining the following characteristic masses in units of solar masses with decadic logarithms of: $12.11^{+0.47}_{-0.42}$, $12.16^{+0.18}_{-0.17}$, $12.22^{+0.28}_{-0.25}$ and the following minimum halo masses: 11.87, 11.94, 12.04 at $z \sim 3.1$, $z \sim 3.5$ and, $z \sim 4.1$ respectively (Section 2.3.2). Given the fact that these mass estimates are consistent which each other at different redshifts, we also obtain a combined constraint by combining all quasars in our samples, resulting in a characteristic halo mass with a decadic logarithm of $12.16^{+0.14}_{-0.13}$ in units of solar masses and a minimum halo mass of 11.94. We then compare our results to other estimates of quasar host halo masses obtained through clustering studies at similar redshifts (see Figure 2.7) finding good agreement with quasar-galaxy cross-correlation studies and intermediate values between the two discrepant quasar auto-correlation clustering measurements of Eftekharzadeh et al. (2015) and Shen et al. (2007) at z$\sim$ 3. We stress that our method is based on the kinematics of cold emitting gas in the CGM of quasars, thereby providing an independent estimate with respect to these studies. Despite the relatively large errorbars due to the limited number of nebulae used in this study, our results suggest no significant redshift evolution of the (bright) quasar host halo masses across the explored redshift range. Combining our studies with cross-correlation clustering results and with the auto-correlation clustering measurements of Eftekharzadeh et al.

(2015) at $z \sim 2.5$ would consistently give a characteristic halo mass of $\sim 10^{12.2} M_{\odot}$ and thus disfavour masses around $\sim 10^{13} M_{\odot}$, such as those suggested by Shen et al. (2007), with a high level of confidence.

The uncertainties associated with our measurement can be significantly improved in the future by taking advantage of the large sample of quasar Lyα nebulae discovered so far (Cai et al. 2019; Farina et al. 2019; Mackenzie et al. 2021), which have not been included in the present study for the sake of brevity. Moreover, ongoing and future observations of Hα emission from quasar nebulae at z$>$ 2, e.g. with JWST or from the ground at some particular redshift (e.g. Langen et al. 2023) will further reduce possible uncertainties associated with the Lyα line radiative transfer, allowing, for instance, to use the *absolute* value of the velocity dispersion as an additional constraint together with the *shape* of the velocity dispersion profile. Additionally, our method could be applied to different subsamples of quasars, e.g., as a function of their UV luminosity or radio-loudness, in order to disentangle possible environmental effects associated with different quasar sub-samples.

In the context of the RePhyNe project, whose main goal is to constrain and resolve the physics of the cold component of the CGM, the results presented here provide a possible resolution to the discrepancy previously found in the literature concerning the host halo masses of quasars at $z \sim 3$. This allows us to break several degeneracies between, e.g., implied cold gas densities and CGM clumpiness from the Lyα emission and halo masses. In particular, based on the analytical model presented in Pezzulli & Cantalupo (2019), a host halo mass of $\sim 10^{12.2} M_{\odot}$ (or lower) for quasar Lyα nebulae would imply high densities in the CGM which cannot be easily confined by the thermal pressure of the hot virialised gas. This would imply, e.g., the presence of broad gas density distributions in the CGM of quasars, as suggested by Cantalupo et al. (2019), or, alternatively, a significant contribution to the Lyα emission from mechanisms differing from recombination radiation (a hypothesis that will be directly tested by JWST Hα emission observations and has so far been excluded by current observations from the ground, (e.g. Langen et al. 2023; Leibler et al. 2018)). In Chapter 3, we take advantage of the results presented here to put strong constraints on the physical properties of cold emitting gas in the CGM of high redshift galaxies (hosting an AGN) by comparing analytical and numerical models to the observed Lyα Surface Brightness profiles.

Chapter 3

High gas densities and turbulence are required to explain observed surface brightness levels at $z \geq 3$[1]

Abstract

The detection of Lyα emission around quasars at high redshift has opened a new window on the study of the Circumgalactic medium (CGM). However, the CGM physical properties, such as its small scale density distribution, are still poorly constrained. Here, we tackle this problem by comparing the surface brightness values of 37 MUSE-observed Lyα nebulae associated with UV-bright quasars at $3 < z < 4.7$ to those of compatible mock observations of Lyα nebulae generated under the assumption of maximal fluorescence from cosmological, hydrodynamic simulations. The simulated Lyα nebulae are selected from haloes within the mass range of $10^{12.03}$M$_\odot$ - $10^{12.3}$M$_\odot$, as derived from the Lyα kinematics of the observed nebulae. By investigating the contribution from cold gas of varying densities to the surface brightness values in the simulations we show that the CGM needs to reach densities of at least 1 - 10 cm^{-3} and exhibit a broad density distribution to explain the observed surface brightness values. We discuss the possibility that such cold, high density clouds can form due to compressive flows in the CGM, through Kelvin Helmholtz instabilities and through turbulence-induced thermal instabilities. We further use theoretical considerations to show that the negligible redshift evolution of the observed surface brightness values implies that the broadness of the cold gas's density distribution increases with time. If turbulence is the driver of the observed broad density distribution, our results imply that the turbulence of the cold CGM of bright quasars should increase from $z \sim 4$ to $z \sim 3$.

[1]This chapter is adapted from de Beer et al. (in prep.)

3.1 Introduction

As the research presented in this chapter is a continuation of work presented in the previous chapter, its context is much the same. Here, I briefly remind the reader of the background which the work presented here is set against. The standard framework of structure formation predicts that the matter in our Universe is distributed in a pattern of intersecting sheets and filaments, the so-called Cosmic Web (Bond et al. 1996). At the intersections, the nodes, virialised haloes hosting galaxies form (Rees & Ostriker 1977; Silk 1977; White & Frenk 1991). Under the influence of gravity, dark matter and gas continually accrete into the haloes, with shock heating of the gas to temperatures of roughly 10^6 K occurring for haloes with virial masses above $\sim 10^{12} M_\odot$ (Birnboim & Dekel 2003). However, at $z > 2$ a stable virial shock is prevented from forming in the inflowing filaments due to their higher density with respect to the surrounding medium. The gas accreting along the filaments can therefore remain dense and cold ($< 10^5$ K) until it reaches the central galaxy (Kereš et al. 2005; Dekel & Birnboim 2006; Agertz et al. 2009; Dekel et al. 2009; Kereš et al. 2009). However, the physical properties of this cold gas in the Circumgalactic Medium (CGM) remain poorly understood and challenging to observe due to its diffuse nature.

Observations of the CGM are primarily conducted through absorption features in the spectra of background quasars and galaxies, revealing multiple phases (Hennawi et al. 2006; Rubin et al. 2010; Steidel et al. 2010; Tripp et al. 2011) and providing information on column density, mass density, and chemical composition (Rudie et al. 2012; Zafar et al. 2013; Werk et al. 2014; Crighton et al. 2015a,b; Fumagalli et al. 2016; Dutta et al. 2020, 2021; Lofthouse et al. 2023). However, absorption studies only offer one-dimensional information, prompting the need to study the CGM in emission. Recent improvements to the sensitivity of instrumentation, the Keck Cosmic Web Imager (KCWI) and the Multi Unit Spectroscopic Explorer (MUSE) being prime examples, have enabled the detection of faint Lyα emission from the CGM. Three mechanisms—recombination radiation, collisional excitation, and "continuum-pumping"—are potential sources of this emission (Cantalupo 2017), which poses challenges to the derivation of the physical properties of the CGM. Quasar fluorescence, where the intense, ionising radiation from the quasar ionises the CGM on scales of hundreds of kpc, facilitates the physical interpretation as the emission due to recombination radiation becomes the dominant emission mechanism. However, challenges arise due to the lack of resolution in the observations to resolve the structure of the cold CGM, introducing uncertainties related to the cold gas's clumping factor. Additionally, a degeneracy exists between the mass of the halo hosting the Lyα nebula and the cold gas's clumping factor for fixed SB values.

On the theoretical side, large scale simulations typically still lack the resolution to adequately resolve the scales relevant to the cold gas in the CGM such as its cooling length, convective scale, Field length and the scale on which turbulence is driven (Field 1965; Sharma et al. 2010; Peeples et al. 2019). Hence, the physical processes governing the formation and survival of the cold, dense gas in the CGM are

not captured, potentially leading to an underestimation of the amount of cold gas in the CGM at high redshift (Hummels et al. 2019; Mandelker et al. 2019b; Corlies et al. 2020; Nelson et al. 2020). At the same time, high resolution, hydrodynamic simulations of cold gas embedded in a hotter, underdense medium have cast doubts on the survival of cold gas clouds in the CGM (Joung et al. 2012a; Mandelker et al. 2016; Gronke & Oh 2018; Mandelker et al. 2018; Padnos et al. 2018; Mandelker et al. 2019a; Vossberg et al. 2019). Hence, as with observations, it is not yet possible to obtain the precise physical properties of the cold CGM solely using simulations.

The goal of this chapter is to constrain the physical properties of the cold CGM around quasars by comparing observed Lyα nebulae associated with quasars with simulated nebulae. However, due to the degeneracy between SB values, host halo mass and clumping factor of the emitting gas mentioned in the previous paragraph, performing this comparison is not trivial. While it is possible to put constraints on the clumping factor with the non-resonant He-Hα emission (Cantalupo et al. 2019, Travascio et al. in Prep) in the recombination dominated scenario, it is still necessary to first constrain the mass of the host halo. At the redshift range relevant to this work quasar auto-correlation measurements and quasar galaxy cross-correlation measurements suggest quasar halo masses ranging from 10^{12}M$_\odot$ to 10^{13}M$_\odot$ (Shen et al. 2007; Trainor & Steidel 2012; Font-Ribera et al. 2013; Eftekharzadeh et al. 2015; García-Vergara et al. 2017; He et al. 2017). This mass window is too wide to break the degeneracy between clumping factor and halo mass, which is why, in the previous chapter, an independent mass estimation method based on the kinematics of the Lyα emitting CGM is developed. This mass estimation method was then applied to the two samples of observed Lyα nebulae presented in Borisova et al. (2016) and Fossati et al. (2021), which span a redshift range of $z \sim 3-4$ and are all associated with bright quasars, meaning the assumption of maximal fluorescence is applicable. The estimates obtained indicate that Lyα nebulae and associated bright quasars are typically hosted by haloes within a mass range of $10^{12.03} - 10^{12.3}$M$_\odot$ and that there is no evolution in halo mass with redshift. Thus with this narrower mass window in hand, it is now possible to meaningfully compare the observed Lyα nebulae to the simulated ones. In this chapter, the SB profiles of the Lyα nebulae presented in Borisova et al. (2016), Arrigoni Battaia et al. (2019a) and Fossati et al. (2021) are directly compared with the profiles of Lyα nebulae hosted by haloes from the EAGLE simulations within the mass range derived in Chapter 2. With this comparison it is possible to put new constraints on the density distribution of the cold, emitting gas in the CGM. As the observational samples considered in this study span a wide redshift range it is possible to quantify the redshift evolution of the SB profiles and the CGM's density distribution.

3.2 Simulating the CGM in emission

The simulated surface brightness profiles are obtained from mock observations generated using hydrodynamic, cosmological simulations of haloes within the estimated mass range obtained in Chapter 2. We use a subset of the mock observations gener-

ated within the scope of Chapter 2 and refer to it for a detailed description of their generation. In this section we give a brief overview of the simulations used to generate the mock observations and how the mock observations themselves are obtained. We specifically go into the details of the star-formation density threshold used, as this in effect defines the upper ceiling of the emitting gas's density. The samples of observed Lyα nebulae which we compare to are also described and we then develop theoretical expectations regarding the scaling of the SB values with halos mass and redshift. Lastly, we also comment on the consequences of broadening our applied mass window.

3.2.1 Cosmological simulations

In keeping with Chapter 2, we use haloes from the EAGLE (Schaye et al. 2015; Crain et al. 2015; McAlpine et al. 2016; EAGLE-Team 2017) SPH simulation suites, specifically the simulation RefL0100N1504. It consists of a 100^3 cMpc^3 box and initially contains 1504^3 dark matter and baryonic particles with a dark matter particle mass of $9.70 \times 10^6 \mathrm{M}_\odot$ and an initial baryonic particle mass of $1.81 \times 10^6 \mathrm{M}_\odot$. The baryonic physics below the resolution limit are modelled using the standard EAGLE sub-grid physics implementation. This encompasses both the stochastic conversion from star-forming gas particles to stellar particles and the stochastic injection of thermal energy to account for both stellar and AGN feedback (Schaye et al. 2015).

The primary goal of this work is to derive the physical properties of the cold, Lyα emitting CGM around quasars by comparing the observed emission to what simulations predict. We therefore analyse three snapshots at the redshifts $z = 3.017$, $z = 3.528$ and $z = 3.984$, the redshift range of the nebulae we compare to (Borisova et al. 2016; Arrigoni Battaia et al. 2019a; Fossati et al. 2021). In Chapter 2 we find that these nebulae are very likely hosted by haloes within a mass range of $10^{12.03} - 10^{12.3}$ M$_\odot$, thus a sufficiently large cosmological volume is required in order to obtain a population of haloes within this mass range at $z \sim 3{-}4$. At the same time we require a high enough resolution for the CGM to be adequately modelled. Despite the CGM not being fully resolved in the EAGLE simulations, they do reproduce the global column density distribution of HI around quasars (Rahmati et al. 2015) and the overall cold gas kinematics of the CGM (see Chapter 2). These two factors make the RefL0100N1504 simulation the ideal choice for this study. Using cosmological simulations also allows us to include any effects the complex morphology of the cosmic web filaments may have on the SB maps of the Lyα nebulae.

Although cosmological simulations allow us to study populations of haloes due to their large box sizes, they have a major limitation: The multi-phase inter-stellar medium (ISM) is not resolved, necessitating the definition of the star-forming gas's properties through an effective equation of state: $P_{eos} \propto \rho_g^{4/3}$ (Schaye et al. 2015). This implies that the temperature of the star-forming gas is determined by the effective pressure imposed on this unresolved medium and not by any hydrodynamical interactions. In the EAGLE simulations gas is defined as star-forming and placed on the effective equation of state if its density lies above the metallicity dependent

density threshold

$$n_\star(Z) = \left(\frac{0.002}{Z}\right)^{0.64} 10^{-1}\mathrm{cm}^{-3}. \tag{3.1}$$

This density threshold is typically used to separate the CGM from the unresolved ISM which is governed by sub-grid modelling in these simulations. In particular, it is worth noting that due to its dependence on metallicity, this density threshold increases as a function of distance from the central galaxy. However, as the aim of this work is to constrain the density of the cold, Lyα emitting CGM by comparing the observed SB values to those of the simulated Lyα nebulae, the actual value of this density threshold will consequently affect our results. For this reason we calculate the Lyα emission from the CGM for three *constant* star-formation (SF) density thresholds of $n_\star = 0.1$ cm^{-3}, $n_\star = 1$ cm^{-3} and $n_\star = 10$ cm^{-3}. Thus, based on whether the simulated or observed SB values are higher at a given distance from the centre of the halo for one of the constant SF density thresholds, we can derive what maximum density the cold gas in the CGM must reach in order to explain the observed SB values.

3.2.2 Mock integral-field-spectroscopy observations

As this study focuses on Lyα nebulae detected around quasars which are sufficiently as bright to continuously ionise their entire CGM, we generate the mock observations under the assumption of maximal fluorescence. This greatly simplifies the modelling with respect to Lyα nebulae powered by strongly star-forming galaxies, as the emission is predominantly due to the cold gas in the CGM recombining. This is because even though the collisional excitation coefficient dominates the recombination coefficient for temperatures above 10^4 K (Cantalupo et al. 2008), not enough neutral hydrogen remains in the CGM of bright quasars for collisional excitation to contribute significantly to the Lyα emission (Pezzulli & Cantalupo 2019). We can thus neglect contributions to the emission from collisional excitation (Haiman et al. 2000; Fardal et al. 2001; Dijkstra et al. 2006; Cantalupo et al. 2008; Rosdahl & Blaizot 2012). We also neglect contributions due to scattering from the broad line region of the quasar (Cantalupo et al. 2014). Although this contribution has not yet been fully constrained at $z > 3$, results at $z \sim 2.3$ using Hα emission suggest that it should be negligible around bright quasars (Leibler et al. 2018; Cantalupo et al. 2019; Langen et al. 2023) Moreover, theoretical predictions are hampered by the fact that cosmological simulations do not resolve the sub-kpc scales on which the radiative transfer would need to be modelled (Hummels et al. 2019; Corlies et al. 2020; Zahedy et al. 2021). We therefore calculate the gas's Lyα emissivity $\epsilon_{\mathrm{Ly}\alpha}$ using the relation

$$\epsilon_{\mathrm{Ly}\alpha} = \frac{1 - Y/2}{1 - Y} \frac{h\nu_{\mathrm{Ly}\alpha}}{4\pi} n_{\mathrm{H}}^2 \alpha_{\mathrm{eff}}(T) \ . \tag{3.2}$$

Where n_H is the hydrogen number density, $\nu_{\mathrm{Ly}\alpha}$ the Lyα rest frame frequency 1215.67$\mathring{A}$, h is Planck's constant and $(1 - Y/2)/(1 - Y)$ is a correction term due to primordial helium, where Y is the primordial helium's number fraction. The case A

effective recombination coefficient

$$\alpha_{\rm eff}(T) = 0.35 \times \alpha(T) \tag{3.3}$$

is based on the fraction of recombination events that result in Lyα emission as calculated by Cantalupo et al. (2005) and the case A recombination coefficient $\alpha(T)$ is given in Appendix A of Hui & Gnedin (1997).

In addition to ionising the CGM, the central quasar also heats the surrounding medium through photo-electric heating. Due to the gas cooling when it recombines and emits radiation, the temperature of the gas will eventually reach an equilibrium between photo-heating and cooling. We refer to this equilibrium temperature as the gas's photo-heating floor. To account for this effect, we impose a photo-heating floor of 5×10^4 K, as calculated in Pezzulli & Cantalupo (2019) for an ionised medium with a number density of 1 cm^{-3} and a metallicity of 0.1 Z$_\odot$ at a distance of 50 kpc from the central, ionising quasar, assuming a "standard" quasar spectrum (Lusso et al. 2015). As the recombination rate $\alpha(T)$ scales inversely with the temperature of the gas, the value of the photo-heating floor will directly affect the SB values. However, we demonstrate in Section 3.4.5 that our estimate of the CGM's density is unaffected by the exact choice of photo-heating floor.

We generate MUSE compatible mock integral-field-spectroscopy observations using the procedure described in detail in Chapter 2. Very briefly, we populate a grid with the emissivity of all the gas particles within a box centred on the haloes considered for this study using `P2C`. Then we convert the grid to mock cubes based on the position of the cells perpendicular to the line of sight and their velocity along the line of sight. The kinematical information of the cells is obtained by populating a grid with the emissivity weighted line of sight velocity of each gas particle using `P2C` as well. By design, the spatial and spectral resolution of the mock cubes is the same as that of the MUSE integral field spectrograph, which has a spatial resolution of 0.2 arcsec and a spectral resolution of 1.25$\mathring{A}$. To mimic the typical seeing conditions and the line spread function of the deep MUSE observations we want to compare our mock cubes to, we apply two dimensional Gaussian smoothing layer by layer with a FWHM of $\sim$ 7 kpc corresponding to $\sim$ 0.9 arcsec at $z \sim 3.5$, as well as Gaussian smoothing along the spectral direction with a FWHM of $\sim$ 160 km/s. Artificial noise, which has a Gaussian distribution with a standard deviation of $\sigma = 5 \times 10^{-20}$ erg/(s cm^2 arcsec^2 Å), is also added to the cubes layer by layer. We then extract the Lyα nebulae from the mock cubes using `CubEx` from the `CubeExtractor` package applying parameters that are consistent with those used on actual observations. This means that for a nebulae to be extracted by `CubEx`, each of its voxels must have a signal-to-noise ratio higher than two, and that it must consist of more than 1000 voxels. If multiple extended objects are extracted from a mock cube by `CubEx` we only consider the object which coincides with the centre of the halo hosting our assumed ionising source. Having extracted the nebulae, we generate the SB maps by simply summing the flux along the line of sight. Thus, by populating the grid with SPH particles and then integrating over the line of sight, we also introduce a clumping factor to the mock observations. The clumping factor of a cell quantifies the broadness of the gas's density distribution within that cell,

i.e., its density distribution along the line of sight, and is defined as

$$C_l \equiv < n^2 > / < n >^2 . \tag{3.4}$$

The spatial scale or volume over which the integration is performed is l and n refers to the gas density. If the density of the gas is constant on scales of l, the clumping factor is equal to one by definition and greater than one otherwise. Although the clumping factor of the real, observed structures is also defined in this way, it is important to note the actual values of the mock observation's clumping factor and those of the observations are different. As the simulations do not completely resolve the CGM, they also do not model the gas's entire density distribution, leading to a different value with regard to observations for the clumping factor. The primary aim of this study is to asses the density of the observed, Lyα emitting gas through comparison to the density of the simulated nebulae. However, the clumping factor of the mock observations itself depends on the density distribution of the gas in the observed CGM and is the quantity we are trying to constrain. Therefore we set C_l to the lower limit of one and derive constraints on the clumping factor in Section 3.3.2. We produce three mock cubes along three perpendicular lines of sight for each halo analysed and find that while the projection along the line of sight can strongly effect the morphology of the extracted nebulae, it has little to no effect on the inner regions of the circularly averaged SB profiles.

In Figure 3.1 we give a visual impression of the process described above. The top panel shows the intrinsic Lyα SB map of one of the haloes included in this study at $z \sim 3$. It has a virial radius of ~ 94 kpc, which is marked by the crimson circle and a halo mass of $\sim 1.9 \times 10^{12} \mathrm{M}_{\odot}$. The second panel shows the SB map of the nebula extracted using `CubEx` after the application of Gaussian smoothing and adding noise, as described above. The bottom panel shows the circularly averaged SB profiles for the metallicity dependent SF density threshold given in Equation 3.1 (plotted in purple) and the three constant SF density thresholds 10 cm^{-3}, 1 cm^{-3} and 0.1 cm^{-3} (plotted in cyan, light green and dark green). The halo's virial radius is marked by the dashed crimson line. Comparing the four SB profiles reveals that applying the metallicity dependent SF density threshold is broadly equivalent to applying a SF density threshold of 0.1 cm^{-3} in the inner 50 kpc of the halo and equivalent to the constant threshold of 10 cm^{-3} in further out.

3.2.3 Observed samples of Lyα nebulae

Each of the three Lyα nebulae samples we compare our mock observations to are observed with MUSE and their redshifts range from $z \sim 3$ to $z \sim 4$. Here we briefly introduce them and describe the details relevant to this work. We analyse a subsample of the Lyα nebulae presented in Borisova et al. (2016). Each of these 12 nebulae is associated with a radio-quiet quasar within the redshift range $z \approx 3 - 3.3$, some of the brightest known radio-quiet quasars at this redshift, and were observed during the MUSE GTO program 094.A-0396, 095.A-0708, 096.A-0345 PI: S. Lilly. The remaining nebulae presented in Borisova et al. (2016) were observed as part of another MUSE GTO program (094.A- 0131, 095.A-0200, 096.A-0222 PI: J.

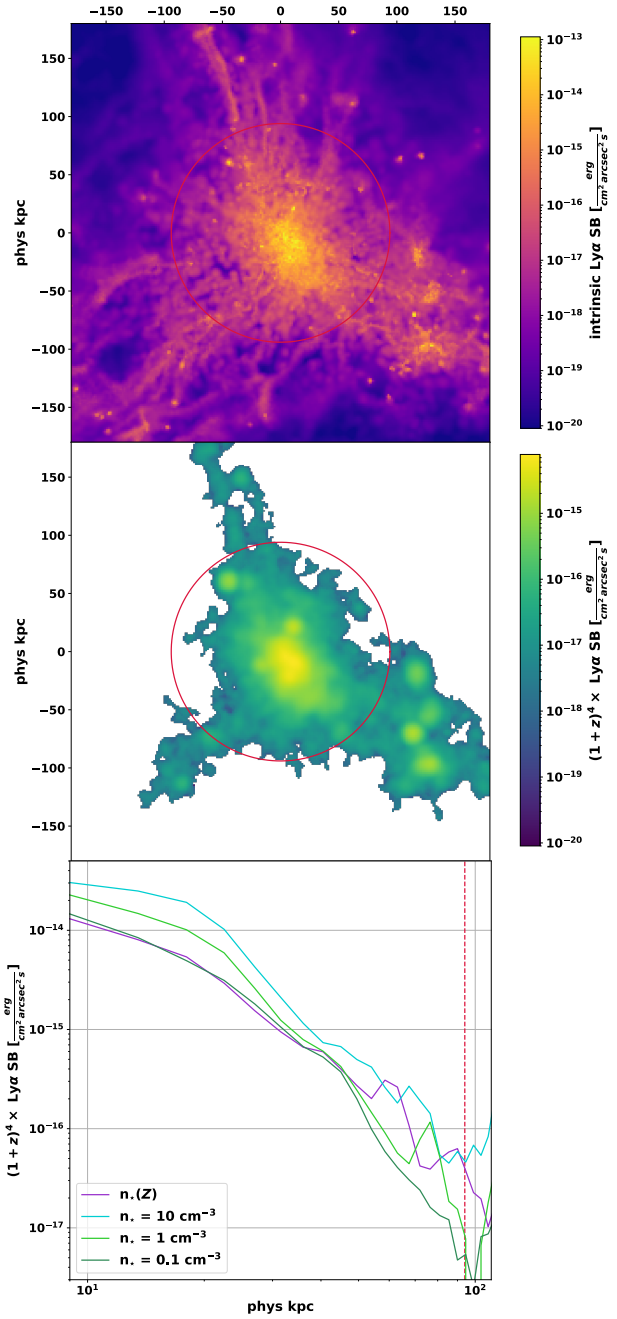

Figure 3.1: A visual impression of the conversion from simulation to Lyα SB profile. The top panel shows the intrinsic Lyα SB map, which is obtained by imposing a SF threshold density of $n_\star = 1$ cm^{-3} and summing the emissivity grid generated by `P2C` over the line of sight. The second panel shows the redshift dimming corrected SB map of the nebula as extracted by `CubEx` from the mock cube generated using the `P2C` output from the top panel. Finally, the bottom panel shows the circularly averaged SB profile of the nebula for the four different SF density thresholds imposed to differentiate the CGM from the ISM. All three panels refer to a halo included in this analysis with a mass of $1.9 \times 10^{12} M_\odot$. The virial radius of the halo (~ 94 kpc) is marked with a crimson circle in the upper two panels, in the lower panel it is marked with the crimson, vertical, dashed line. Based on the four SB profiles it is evident that a higher SF density threshold results in higher SB values.

Schaye), are at a higher redshift and included in the MAGG sample. We calculate the circularly averaged SB profile of each of the 12 Lyα nebulae from the SB maps shown in Figure 1 of that work[2]. Then, to obtain the typical SB values with which to compare our simulated values at $z \sim 3$ in Section 3.3.2, we calculate the median, as well as the 25th and 75th percentiles, of the 12 individual SB profiles. We refer to these 12 nebulae as the MQN sample for the sake of brevity.

The second observational sample we compare our SB profiles to is the QSO MUSEUM survey presented in Arrigoni Battaia et al. (2019a). The QSO MUSEUM survey contains 61 Lyα nebulae associated with quasars with an absolute i-band luminosity normalised to $z = 2$ (Ross et al. 2013) within the range of $-29.67 \leq M_i \leq -27.03$. The survey therefore extends to lower quasar luminosities than the MQN sample, though as can be seen in Figure 3.6 this has no effect on the survey's average SB values with respect to the MQN sample. In Figure 6 of Arrigoni Battaia et al. (2019a) the stacked SB profile of all 61 nebulae is fitted by the exponential $\mathrm{SB}(R) = C_e e^{-R/r_h}$, with $C_e = 56.8 \times 10^{-18}$ erg/(s cm^2 arcsec^2) and $r_h = 15.7 \pm 0.5$ kpc. As the median redshift of the QSO MUSEUM survey is $z \sim 3.2$, we compare our simulated SB profiles at $z \sim 3$ to the fitted exponential.

The MAGG sample contains 28 bright, radio-quiet quasars and their associated Lyα nebulae at redshifts within the range $z \sim 3.2 - 4.5$ and is first introduced in Lofthouse et al. (2020), while Fossati et al. (2021) performed the original extraction of the Lyα nebulae. Following their example we split the MAGG sample into two redshift bins centred on $z \sim 3.5$ and $z \sim 4.1$ and calculate the median SB profile for both bins. In Section 3.3.2 we then compare the MAGG $z \sim 3.5$ SB profile to that of our simulated nebulae at $z \sim 3.5$ and the MAGG $z \sim 4.1$ sample's median SB profile to the $z \sim 4$ simulated SB profiles.

3.2.4 Theoretical Expectations

In order to draw any conclusions concerning the cold CGM's density distribution from SB profiles, it is necessary to first develop a theoretical expectation of how the profiles depend on other physical properties of the host halo and its CGM. The first thing we derive, is how the SB depends on the CGM's cold gas fraction f_{cold}, clumping factor C_l, volume filling fraction f_v and halo mass M_h at a fixed redshift. The SB profiles of Lyα nebulae around bright quasars are well described by a power-law function (Borisova et al. 2016; Arrigoni Battaia et al. 2019a; Fossati et al. 2021):

$$\mathrm{SB}(R) = \mathrm{SB}_0 \left(\frac{R}{R_0} \right)^{-\beta}, \tag{3.5}$$

where R is the projected radial distance to the halo's centre and SB_0 is the surface brightness value at the projected distance R_0. As we are working under the assumption of maximal fluorescence, the Lyα emission from the CGM is dominated by recombination radiation. Hence, the SB profile can also be expressed as an integral

[2]See Figure 4 of Borisova et al. (2016) for the individual SB profiles.

along the line of sight

$$\mathrm{SB}(R) = \int_s A(T)\, f_v\, C_l\, n(s)^2 ds. \tag{3.6}$$

For the sake of readability, we combine all the properties the Lyα emissivity depends on, apart from the density of the gas, in the variable $A(T)$ (see Equation 3.2). The density of the cold gas within the Lyα emitting structures is denoted by $n(s)$, f_v and C_l refer to the cold gas's volume filling fraction and clumping factor respectively. Assuming spherical symmetry and following the derivation presented in Pezzulli & Cantalupo (2019), we can de-project the SB profile given in Equation 3.5 to obtain the profile of the density of the cold, Lyα emitting gas

$$n(r) = n_0 \left(\frac{r}{R_0}\right)^{-\gamma}. \tag{3.7}$$

Where r is the radial distance to the centre of the halo, the slope γ depends on the SB profile's slope β through the relation

$$\gamma = \frac{1+\beta}{2}, \tag{3.8}$$

and n_0 is the average cold gas density at a distance R_0 to the halo's centre. This average density n_0 can be expressed as

$$n_0 = \left(\frac{\mathrm{SB}_0}{2\, f_v C_l R_0\, A(T)\, \chi(1+\beta)}\right)^{1/2}, \tag{3.9}$$

where C_l is the clumping factor on scales of l, f_v is the cold gas's volume filling fraction and χ is the dimensionless projection factor defined as

$$\chi(a) \equiv \int_0^\infty \left(1+x^2\right)^{-a/2} dx, \tag{3.10}$$

according to both Pezzulli et al. (2017) and Pezzulli & Cantalupo (2019). The total mass of the cold gas within the CGM M_{cold} can be obtained by integrating the density profile in Equation 3.7 over the virial sphere:

$$M_{cold} = \int_0^{R_{vir}} 4\pi \frac{m_p}{X} r^2 f_v\, n(r)\, dr = 4\pi \frac{m_p}{X} \frac{R_{vir}^3}{3-\gamma} \left(\frac{R_0}{R_{vir}}\right)^{\gamma} f_v\, n_0. \tag{3.11}$$

The mass of the proton is denoted by m_p and X refers to the cosmic hydrogen abundance by mass. By combining the definition of the CGM cold gas fraction

$$f_{cold} = \frac{M_{cold}}{(\Omega_b/\Omega_m) M_h}, \tag{3.12}$$

Equations 3.9 and 3.11 with the scaling relation $R_{vir}^3 \propto M_h$ and generalising from the specific projected distance R_0 to any projected distance R, we finally find a scaling relation for the SB values:

$$\mathrm{SB}(R) \propto R^{-\beta} f_{cold}^2 \frac{C_l}{f_v} M_h^{(1+\beta)/3}. \tag{3.13}$$

It is worth noting at this point, that the physical properties f_{cold}, C_l and f_v likely vary with halo mass themselves. We address this potential complication below.

The scaling relation above is derived for a fixed redshift. Conversely, if one fixes the halo mass but varies the redshift one obtains the relation

$$\mathrm{SB} \propto (1+z)^5. \tag{3.14}$$

This is derived based on the following arguments: The surface brightness is the line of sight integral of the gas's emissivity, thus the main variables the surface brightness depends on are the distance integrated over, the gas's density squared and its recombination rate (see Equation 3.2). The cold gas outside of the virial sphere does not substantially contribute to the emission from the Lyα nebulae. Hence, the integration length corresponds to twice the halo's virial radius, which for a set halo mass scales as $(1+z)^{-1}$. As for the density, assuming a monolithic density profile for all halos, independent of mass and redshift, the gas density within a halo's virial sphere scales as $(1+z)^3$. This is because for two halos to have the same mass at different redshift, they need to have collapsed at different times, i.e. the higher redshift halo collapsed earlier in the Universe when the average gas density was higher. In contrast, the temperature dependent recombination coefficient does not vary with redshift, thereby not contributing to the scaling relation. This derivation implicitly assumes that the cold gas fraction, volume filling fraction and gas clumping factor do not vary with redshift. We return to this important assumption in Section 3.3.3.

As demonstrated in Equation 3.13, the mass of a halo hosting a Lyα nebula around a bright quasar needs be constrained if one wants to make any inferences about the Lyα emitting CGM based on the Lyα SB profiles. Furthermore, the dependencies of the cold gas fraction, volume filling fraction and clumping factor on the halo mass are not well constrained, making it even more difficult to obtain any constraints on the density of the emitting gas. Luckily, in Chapter 2 we show that bright quasars likely live within the narrow mass range of $10^{12.03} - 10^{12.3}$ $\mathrm{M}_\odot$ at $z \sim 3-4$. This estimated mass window is sufficiently narrow that it becomes plausible to assume that neither the cold gas fraction, volume filling fraction nor clumping factor varies significantly within the mass range relevant for this work at a fixed redshift. In Chapter 2 we also show that there is little to no evolution of the quasar halo masses from $z \sim 4$ to $z \sim 3$, an assumption that goes into the derivation of the evolution of SB values with redshift described by Equation 3.14. As with Equation 3.13, the additional assumption that f_{cold}, C_l and f_v do not vary significantly with redshift is also necessary for the derivation. Therefore, by comparing the redshift evolution of observed SB profiles with our theoretical expectation given in Equation 3.14, it is possible to make inferences concerning the redshift evolution of the physical properties of the CGM as deviations from this relation should primarily be caused by changes in the cold gas fraction, volume filling fraction or cold gas clumping factor.

It is worth considering that the kinematics of the Lyα nebulae analysed in this work are consistent with both a characteristic halo mass of $10^{12.16}$ $\mathrm{M}_\odot$ and a minimum halo mass of $10^{11.94}$ $\mathrm{M}_\odot$ (see Chapter 2). Clearly, if the nebulae are indeed

hosted by haloes with a variety of masses above $10^{11.94}$ $M_\odot$, the assumption that f_{cold}, C_l and f_v do not vary significantly is no longer plausible. While using a minimum mass as opposed to a characteristic mass has little effect on the SB profiles themselves, as we show in Appendix F, we discuss which of the two scenarios is more likely based on observations and what a wider mass range would imply for our results Section 3.4.5.

3.3 Results

In Section 3.3.1 we first evaluate our simulated SB profiles with respect to the theoretical expectations outlined above. Having developed an understanding of the simulated SB profiles' behaviour, we compare them to the observed Lyα SB profiles in Section 3.3.2, with the aim of constraining the density of the cold, emitting gas. Then in Section 3.3.3, we investigate the implications of the observed Lyα SB profiles' redshift evolution on the kinematics and morphology of the cold CGM.

3.3.1 Simulated Lyα surface brightness profiles

As demonstrated in Section 3.2.4, theoretical considerations imply that the SB values of the Lyα nebulae scale with halo mass. Figure 3.2 shows the SB profiles of the simulated Lyα nebulae hosted by haloes in four separate mass bins at $z \sim 4$, $z \sim 3.5$ and $z \sim 3$. It is evident that the SB values do indeed increase with halo mass as predicted by Equation 3.13. Taken in conjunction with Figure 3.1, Figure 3.2 clearly shows that a higher halo mass and a lower SF density threshold can produce the same SB values as a lower halo mass with a higher SF density threshold, as already mentioned in the Introduction. At this point we stress that the simulated Lyα SB values should be thought of as upper values due to them being calculated under the assumption of maximal fluorescence. The profiles we obtain are broadly consistent with those obtained by previous studies (Gronke & Bird 2017; Costa et al. 2022), both with regards to their shape and values. Figure 3.2 also indicates that the assumption that the profiles are well approximated by a power-law function with a constant exponent $-\beta$ holds reasonably well. At each redshift we fit the median SB profile in each mass bin with a power-law and obtain the following average exponents: $\beta = 2.3 \pm 0.4$ at $z \sim 4$, $\beta = 2.0 \pm 0.2$ at $z \sim 3.5$ and $\beta = 2.1 \pm 0.2$ at $z \sim 3$. As already alluded to above, in Equation 3.13 the cold gas and volume filling fractions' scalings with halo mass are not explicit, as a priori we have no theoretical expectations concerning this. To remedy this, we calculate both the cold gas fraction f_{cold} and the volume filling fraction f_v for a representative sample 100 haloes in the EAGLE Ref simulation at $z \sim 4$, ~ 3.5 and ~ 3 in the mass range $10^{11.75} - 10^{13}$ $M_\odot$. In Figure 3.3 we plot f_{cold}, as defined in Equation 3.12, as a function of halo mass at each redshift included in this study. We find that the CGM's cold gas fraction decreases with halo mass at a rate of approximately $f_{cold} \propto M_h^{-0.7}$. Though other works do not measure the same scaling relation, they do measure values compatible with those reported in Figure 3.3 (Wang et al. 2017; Suresh et al. 2019; Ramesh et al. 2023)

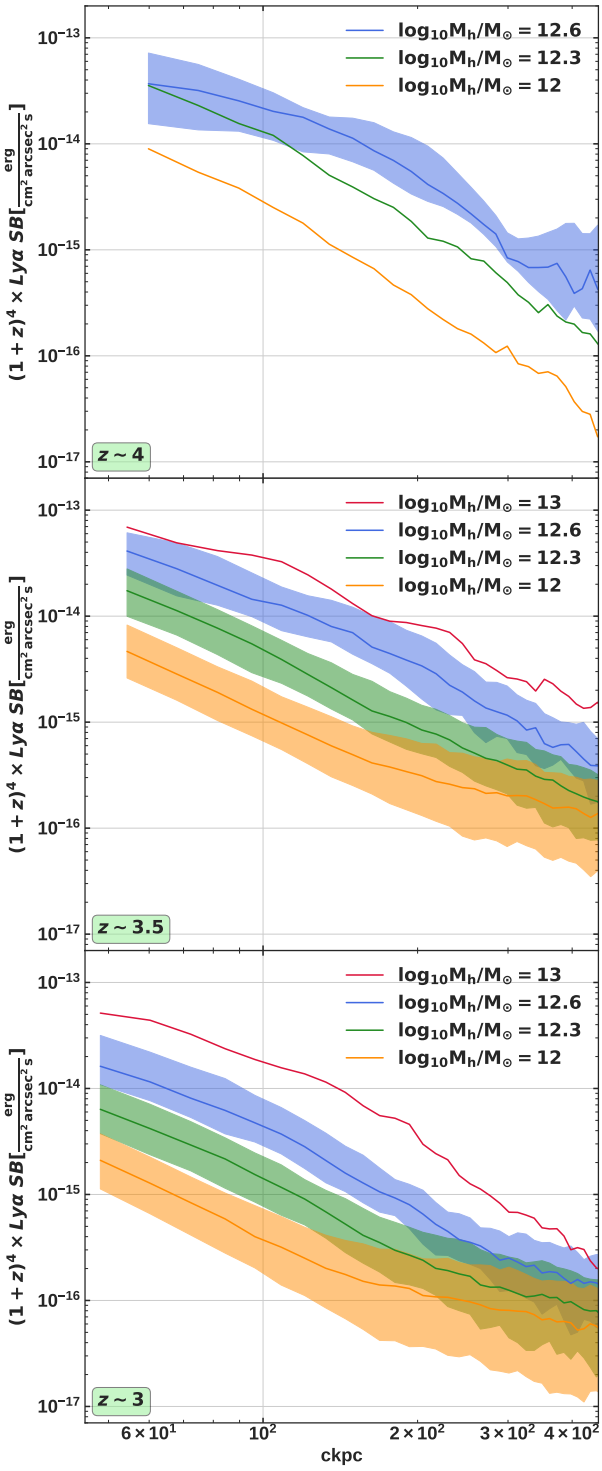

Figure 3.2: The circularly averaged, redshift dimming corrected SB profiles of Lyα nebulae hosted by haloes in mass bins centred on 10^{12}M$_\odot$ (orange), $10^{12.3}$M$_\odot$ (green), $10^{12.6}$M$_\odot$ (blue) and 10^{13}M$_\odot$ (red). The solid lines indicate the medians of each mass bin and the shaded regions denote the 25th and 75th percentiles of the bins. Beginning at the top, the panels refer to the redshifts of the simulation snapshots, which are $z \sim 4$, $z \sim 3.5$ and $z \sim 3$. While the SB values increase with both redshift and halo mass, the shape of the profiles varies little with halo mass (excluding the highest mass bin which suffers from poor number statistics at each of the three redshifts).

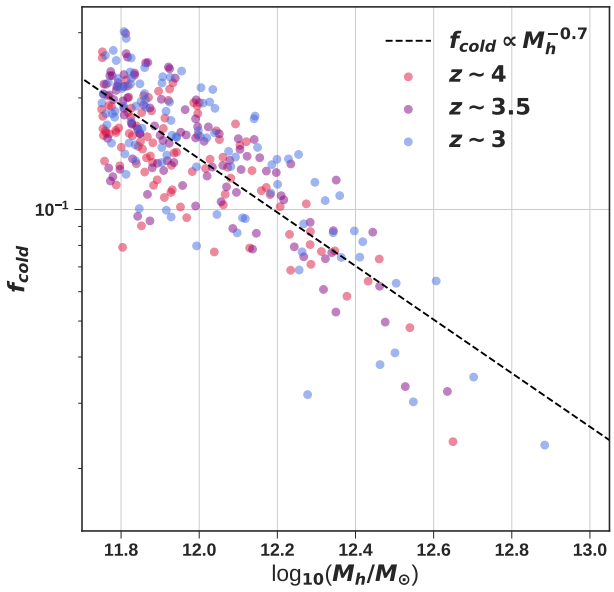

Figure 3.3: The cold gas fraction, as defined in Equation 3.12, for a representative sample of 100 haloes within the mass range $10^{11.75} - 10^{13} \mathrm{M}_\odot$ at the three redshifts considered in this work. As demonstrated by the grey, dashed line, the cold gas fraction scales roughly as $\propto M_h^{-0.7}$ at each redshift.

and Wright et al. (2021) also find a decrease in f_{cold} with halo mass. Interestingly, Ramesh & Nelson (2023) find that the cold gas fraction slightly increases with halo mass for a set of eight zoomed-in ILLUSTRIS-TNG haloes. Figure 3.4 shows the volume filling fraction of the representative sample of haloes at each redshift as a function of halo mass. As with the cold gas fraction, the volume filling fraction also scales strongly with halo mass as $f_v \propto M_h^{-1.6}$. Additionally, Figures 3.3 and 3.4 reveal a negligible evolution of both f_{cold} and f_v with redshift across the whole halo mass range considered. We return to this lack of redshift evolution and its implications in Section 3.3.3.

Combining these scaling relations with Equation 3.13, we obtain the prediction that the SB values should scale as approximately SB $\propto M_h^{2.2}$ at $z \sim 4$ and SB $\propto M_h^{2.1}$ at both $z \sim 3.5$ and $z \sim 3$. To quantify to what extent the mass-scaling of the simulated SB profiles matches our theoretical prediction, we calculate the ratio of the median SB profile in each mass bin and the median SB profile in the lowest mass bin ($10^{12\pm0.15}$ $\mathrm{M}_\odot$). In detail, we calculate this ratio in each radial bin and then take the median of all these ratios. The median ratios are plotted for $z \sim 3$ (blue), $z \sim 3.5$ (purple) and $z \sim 4$ (red) as a function of the ratios' numerator's halo mass, with the errorbars denoting the 25th and 75th percentiles in Figure 3.5. We further indicate the theoretically predicted scaling with red and purple solid lines and a dashed blue line for the three redshifts. The shaded regions mark the uncertainty of the scaling relation based on the exponent β's standard deviation. The actual mass scaling of

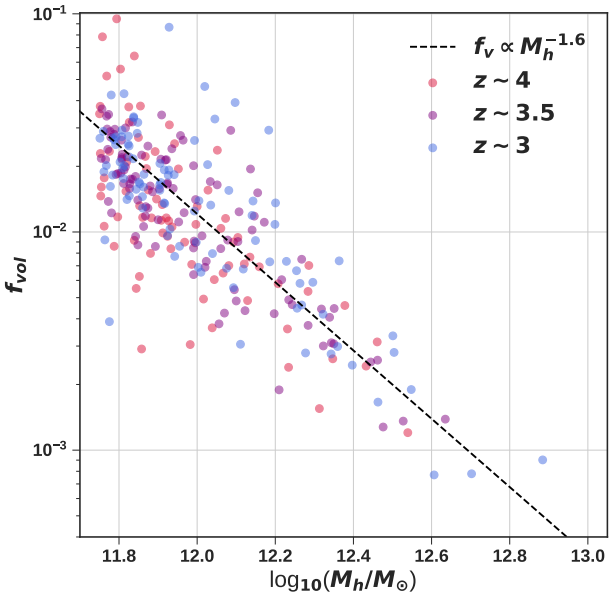

Figure 3.4: The cold gas volume filling fraction, for a representative sample of 100 haloes within the mass range $10^{11.75} - 10^{13} \mathrm{M}_\odot$ at the three redshifts considered in this work. As demonstrated by the grey, dashed line, the cold gas volume filling fraction scales roughly as $\propto M_h^{-1.6}$ at each redshift.

the simulated SB values is indicated with a grey, dashed line and can be written as SB $\propto M_h^{1.7}$. Despite the relative simplicity of our derivation in Section 3.2.4, the actual scaling of the simulated SB values and the predicted scaling are remarkably close to one another. The slight discrepancy between the scaling relations is likely due to a slight variation of β with halo mass and the fact that we assume none of the variables considered vary with distance to the halo centre, which is only valid as a first order approximation.

3.3.2 Density of the Lyα emitting gas

Having established the strong scaling of the SB values with halo mass through theoretical expectations in Section 3.2.4 and simulated Lyα nebulae in Section 3.3.1, we now fix the mass of the haloes in order to compare our simulated SB profiles with the observed profiles. This will allow us to constrain the density of the emitting gas in the CGM.

In Chapter 2 we found that the Lyα nebulae of the combined MAGG and MQN samples are hosted by haloes with a characteristic mass between $10^{12.03}$ $\mathrm{M}_\odot$ and $10^{12.3}$ $\mathrm{M}_\odot$. Hence, we calculate the SB profiles of the simulated Lyα nebulae hosted by haloes within this mass range while varying the SF density threshold i.e., the maximum density of the emitting gas. As already mentioned in Section 3.2.2 and demonstrated in Figure 3.1, the metallicity dependent SF density threshold used in

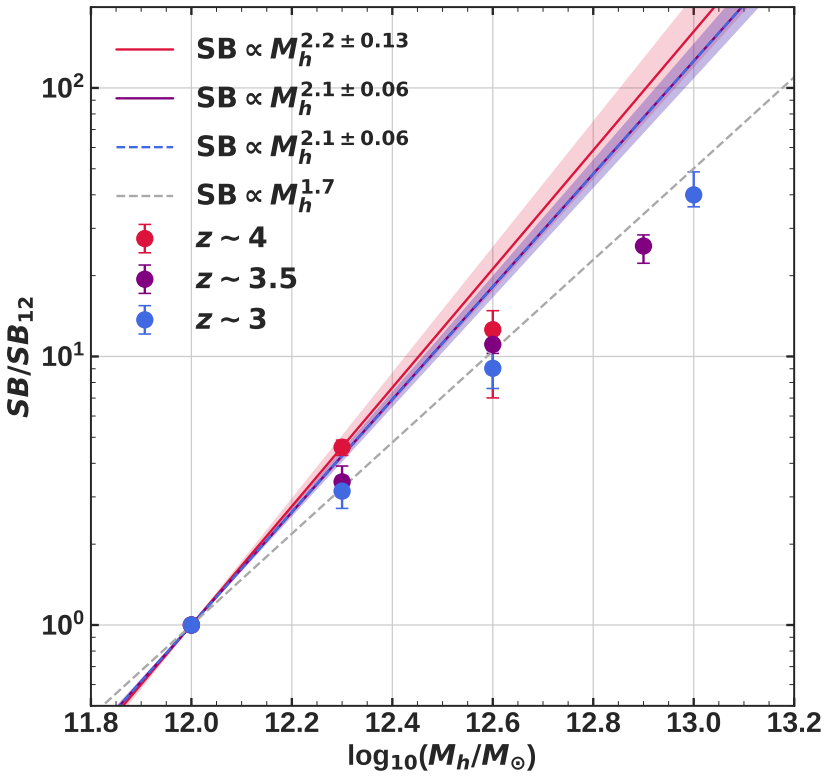

Figure 3.5: The ratios of the median SB profiles in the various mass bins and the median SB profiles in the 10^{12}M$_\odot$ bin as a function of halo mass. The points show the median ratios at $z \sim 4$ (red), $z \sim 3.5$ (purple) and $z \sim 3$ (blue), with the errorbars indicating the 25th and 75th percentiles of the ratios. The solid lines show the scaling of the SB values with halo mass as predicted by Equation 3.13 based on the exponent β of the power-law fitted to the SB profiles and the mass scaling of f_{cold} and f_v. The grey dashed line indicates the redshift independent scaling of the SB ratios with halo mass: SB $\propto M_h^{1.7}$.

the EAGLE simulations is qualitatively equivalent to applying a fixed threshold of 0.1 cm^{-3}. We calculate the SB profiles for this fixed threshold of 0.1 cm^{-3} as well as for the two higher thresholds of 1 cm^{-3} and 10 cm^{-3} for each Lyα nebula hosted by a halo within the relevant mass range at $z \sim 4$, $z \sim 3.5$ and $z \sim 3$. The resultant median SB profiles are plotted in blue ($n_* = 10$ cm^{-3}), magenta ($n_* = 1$ cm^{-3}) and purple ($n_* = 0.1$ cm^{-3}) and in Figure 3.6 we compare them to the median SB profiles of the observed samples at $z \sim 4.1$ (MAGG high redshift sample, dashed red line, top left panel), $z \sim 3.5$ (MAGG low redshift sample, dashed blue line, top right panel) and $z \sim 3$ (MQN and MUSEUM samples, dashed green and yellow lines, bottom left panel). At $z \sim 4$ the MAGG high redshift sample's median SB profile is well matched by the simulated profile where the maximum density of the emitting gas is $n_* = 1$ cm^{-3} and consistently higher than the SB profile with $n_* = 0.1$ cm^{-3}, implying that the cold gas throughout the CGM needs to reach densities of $n_* = 1$

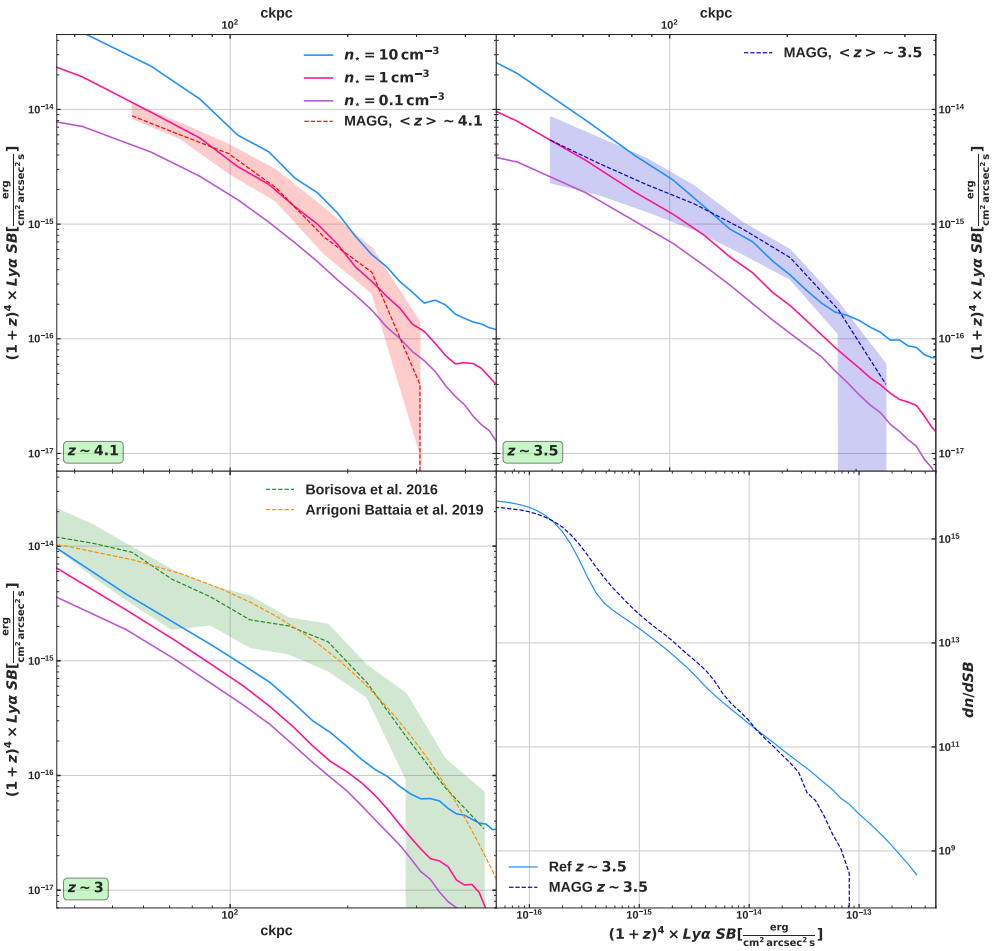

Figure 3.6: The top panels and the lower left panel show the simulated SB profiles, corrected for redshift dimming, of the Lyα nebulae hosted by halos within the mass range $10^{12.03} - 10^{12.3}\mathrm{M}_\odot$ plotted with solid lines, with the different colours refering to the three SF density thresholds applied: $n_\star = 10\mathrm{cm}^{-3}$ (blue), $n_\star = 1\mathrm{cm}^{-3}$ (pink) and $n_\star = 0.1\mathrm{cm}^{-3}$ (purple). The dashed lines show the SB profiles of the samples of observed Lyα nebulae considered. The MAGG $z \sim 4$ profile is in red, the MAGG $z \sim 3.5$ in blue, the MQN sample is plotted in green and the QSO MUSEUM sample in orange. The lower right panel shows the average, normalised histograms of the SB values from the low redshift MAGG sample (dashed, dark blue line) and the simulated Lyα nebulae at $z \sim 3.5$ (solid, light blue line). Although the simulations reproduce the average SB values, they overpredict the amount of pixels at the bright end of the distribution and underpedict the amount of pixels with values of $2 \times 10^{-16} - 10^{-14}$ erg/(s cm^2 arcsec^2). This is indicative of the fact that the simulations do not adequately resolve the CGM, leading to an underprediction of the amount of cold, dense clouds distributed throughout the CGM.

cm^{-3} at $z \sim 4$ to explain the observations. The low redshift MAGG sample's median SB profile's values are consistent with an SF density threshold of $n_* = 1$ cm^{-3} near the centre, but then become more compatible with a threshold of $n_* = 10$ cm^{-3} as one moves towards the outer region of the nebulae. As for z$\sim$ 3, the median SB profiles of both the MQN and MUSEUM samples are significantly higher than even the simulated SB profile for $n_* = 10$ cm^{-3}. Taken together, these three results imply that at $z \sim 3-4$ the cold gas reaches densities of 1 - 10 cm^{-3} throughout the CGM of bright quasars. As we show in Appendix G this result is unaffected by the exact resolution of the cosmological simulations. In the lower right panel of Figure 3.6 we plot the average, normalised SB histogram of the Lyα nebulae from the low redshift MAGG sample with a dashed, dark blue line and the average, normalised SB histogram of the Lyα nebulae hosted by haloes in the $10^{12.03}\mathrm{M}_\odot$ to $10^{12.3}\mathrm{M}_\odot$ mass range in the EAGLE Ref simulation at $z \sim 3.5$ with a solid, light blue line. While the simulated nebulae generated with a SF density threshold of 10 cm^{-3} reproduce the circularly *averaged* SB profiles from observations well, the SB value distributions differ in two keys aspects. The simulated Lyα SB maps underpredict the amount of pixels with values in the range of $2\times10^{-16}-10^{-14}$ erg/(s cm^2 arcsec^2), but overpredict values above 10^{-14} erg/(s cm^2 arcsec^2). This discrepancy is due to differences between the cold gas density distribution in the simulated and observed CGM and we discuss its implications in Section 3.4.2.

Although Rosdahl & Blaizot (2012) find that lower density values are sufficient to power Lyα emission in their simulations, our density estimates are in good agreement with other density estimates obtained from observations of Lyα nebulae around bright quasars (Hennawi et al. 2015; Arrigoni Battaia et al. 2015; Cai et al. 2018; Arrigoni Battaia et al. 2019b; González Lobos et al. 2023). Interestingly, while the shapes of the simulated and observed profiles are somewhat consistent with each other at $z \sim 4$, they seem to become more dissimilar with decreasing redshift. This could mean, that in addition to the maximum of the cold gas density increasing with time, the shape of the cold gas density profiles could also evolve with time. We explore this further in the next Section. As we do not include any local radiative transfer effects, it is possible that the difference between the observed and simulated SB profile could also be due to the latter and we leave a detailed analysis of the shape of the SB circularly averaged radial profiles to future work.

3.3.3 Redshift evolution

A visual comparison of the SB profiles in Figure 3.6's three panels indicates that while the values of the simulated SB profiles seem to increase with redshift as predicted by Equation 3.14, the observed ones remain constant. This is demonstrated more clearly in Figure 3.7. We calculate the ratios of the SB profiles with respect to those at $z \sim 4$ for both the simulated and observed nebulae, where for the simulated SB profile we use those generated with a SF density threshold of $n_* = 1$ cm^{-3}. The values of the simulated SB profiles do indeed increase with redshift, although at a higher rate than predicted by Equation 3.14. Given the simplicity of the derivation of the expected redshift scaling in Section 3.2.4, this level of agreement between

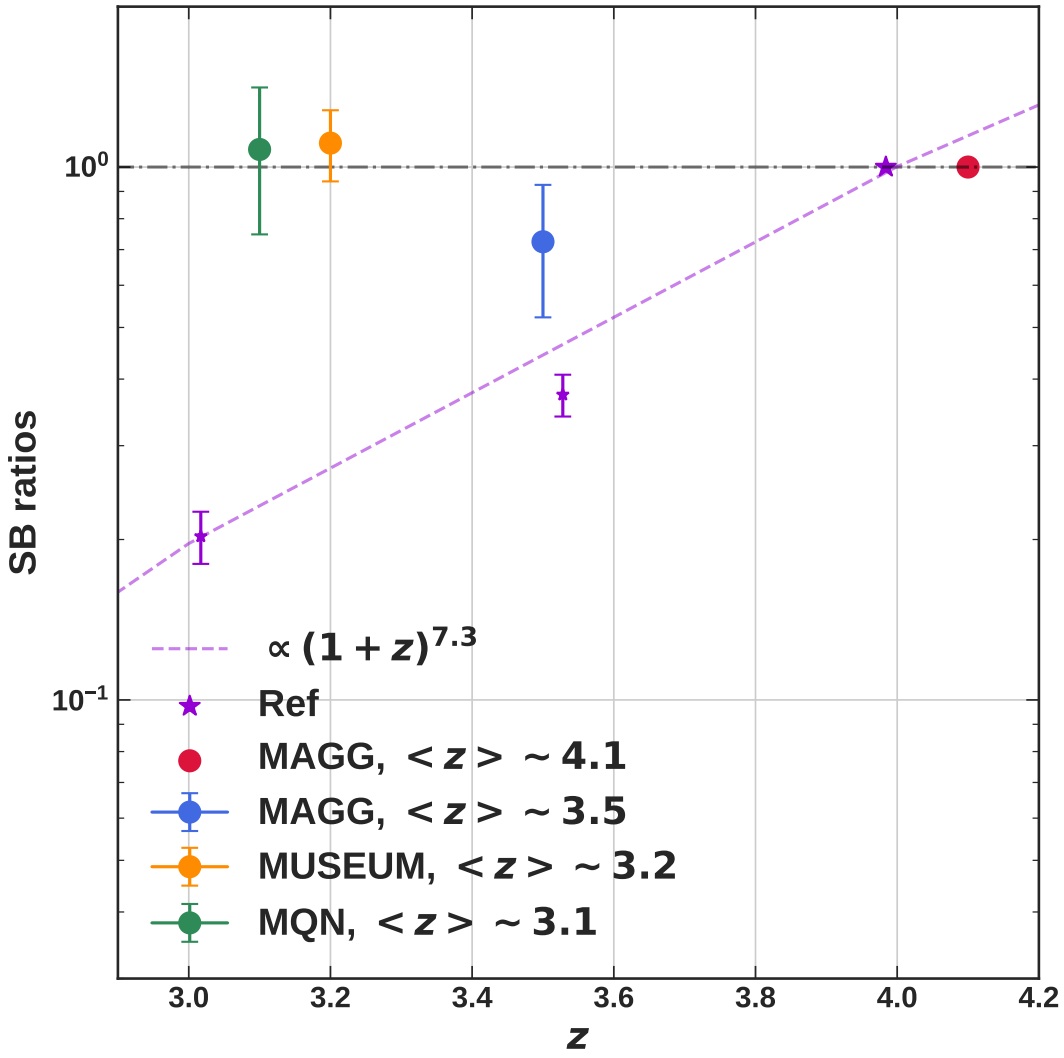

Figure 3.7: The ratios of the observed and simulated SB profiles at the various redshfit and those at $z \sim 4$. The coloured circles and error bars indicate the SB ratios for the MAGG $z \sim 4.1$ (red), MAGG $z \sim 3.5$ (blue), QSO MUSEUM (yellow) and MQN (green) samples. The purple stars and error bars show the simulated ratios. The purple, dashed line indicates the redshift evolution of the simulated SB values, which is proportional to $(1 + z)^{7.3}$. In contrast, the observed ratios remain roughly constant at a value of one (marked by the grey, dash-dotted line) indicating a negligible evolution of the observed SB values with redshift.

the evolution of the simulated SB profiles and the theoretical expectation is quite remarkable. One could ask, however, whether this slight discrepancy is due to an evolution of the simulated cold gas fraction or volume filling fraction, which were assumed to be constant when driving Equation 3.14. We investigate the possible redshift evolution of f_{cold} in Figure 3.8, where we show the f_{cold} histograms of each halo in the mass range considered for each redshift. There is marginal evidence that the simulated cold gas fraction actually decreases with redshift, which would increase the tension between the theoretical redshift scaling and that of the simulated SB profiles. However, we note that this increase is subtle: the median cold gas fraction goes from ~ 0.9 at $z \sim 4$ to ~ 0.125 at $z \sim 3$. When calculating the cold gas fraction for each halo, we use the definition given in Equation 3.12. Although the precise values of f_{cold} depend on how it is defined, we find that the trends with both halo mass and redshift as reported in Figures 3.3 and 3.8 remain unchanged irrespective of the exact definition of f_{cold}. The histogram of the simulated CGM's volume filling fraction at all three redshifts in Figure 3.9 reveals even less of a trend with redshift and the median f_v at each redshift is consistent with the other redshifts within their 25th to 75th percentiles at about 6×10^{-3}. The marginal evolution of f_{cold} and the non-evolution of f_v thus imply that the increase of simulated SB values with redshift is primarily driven by changes in the cold gas density distribution with redshift. Indeed, we find that the average density of the cold gas in the CGM increases with redshift at a rate of $(1+z)^{4.13}$ within the redshift range considered (see Appendix H), in good agreement with the derivation in Section 3.2.4 and the SB scaling shown in Figure 3.7. As it is the square of the density which primarily drives the Lyα emission (see Equation 3.2), we plot the probability density distribution (PDF) of the density squared in Figure 3.10. The PDFs in Figure 3.10 reveal that in addition to the average density increasing with redshift, the distribution of the density also becomes broader with redshift, thus causing the increase in SB values with redshift.

The behaviour of the observed SB values is in stark contrast to that of the simulated nebulae described above. The observed SB ratios remain close to one, irrespective of redshift, indicating that the observed SB values of Lyα nebulae around bright quasars remain constant with redshift, as previously reported in Fossati et al. (2021). This non-evolution of the SB values could be caused by an increase of one of the following factors with time: the average density of the cold CGM, its cold gas fraction, volume filling fraction, the broadness of the cold gas density distribution (i.e. the CGM's clumping factor) or the mass of the halo hosting the quasar and its associated nebulae. We find it unlikely that the average density of the cold gas increases with time, contrary to standard cosmology and thus discard that hypothesis. There are currently few observational constraints on the CGM cold gas fraction as well as its volume filling fraction and none known to us which track their evolution over time. As already mentioned above, Figures 3.8 and 3.9 indicate a negligible evolution with redshift for a fixed halo mass for both properties in simulations. For now we assume that this is also the case in the real Universe. This leaves an increase in halo mass or clumping factor with time as the two remaining causes driving the unexpectedly high SB values at $z \sim 3$ and $z \sim 3.5$. In Chapter 2 we demonstrate

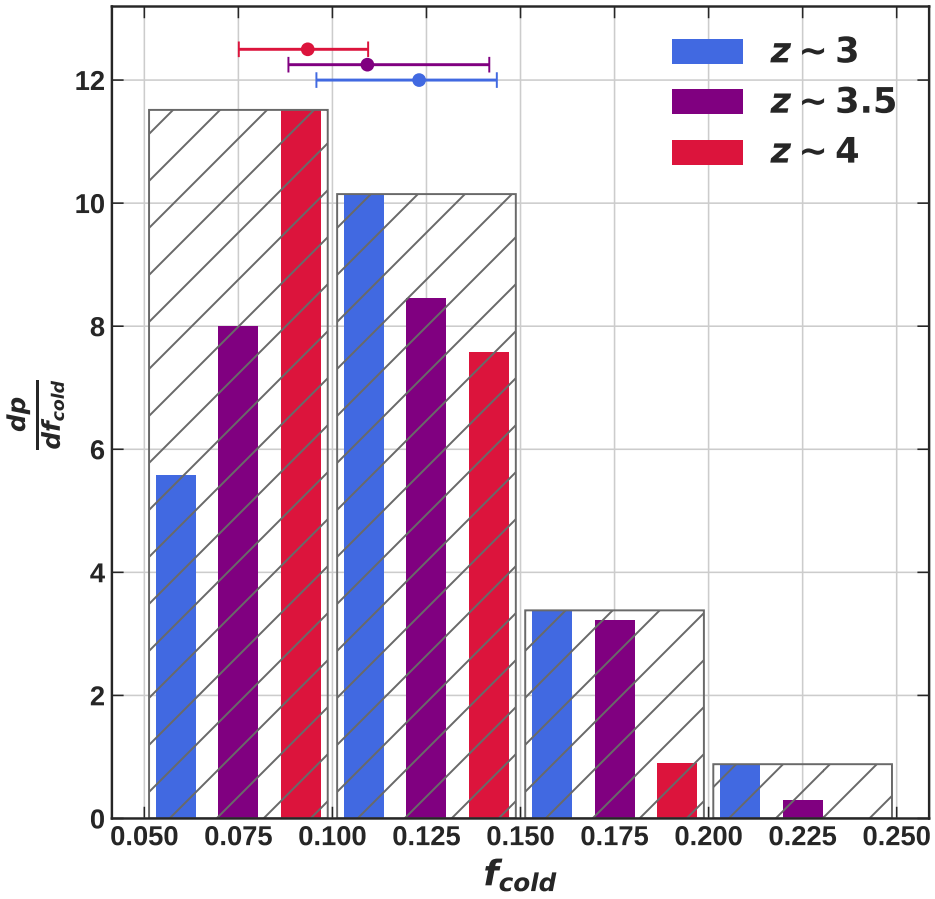

Figure 3.8: Normalised histograms of the cold gas fraction as defined in Equation 3.12 of the haloes within the mass range $10^{12.03} - 10^{12.3}\mathrm{M}_{\odot}$ at $z \sim 3$, $z \sim 3.5$ and $z \sim 4$. The grey, hatched bars mark the cold gas fraction bins and the three coloured bars inside the hatched bins correspond to the three different redshifts. The three points and errorbars at the top of the figure indicate the median, 25th and 75th percentile of the cold gas fraction for each redshift. Although there is a negligible evolution in the cold gas fraction with redshift, it is not sufficient to explain the deviation of the simulated SB values redshift scaling from the theoretically predicted scaling of $(1+z)^5$.

that the halo masses in the sample considered here (with the exception of the MUSEUM sample) stay almost constant with redshift and, if anything, actually slightly decrease with time. Setting aside our results, quasar galaxy and Lyα forest cross-correlation results indicate no redshift evolution (Steidel et al. 2011; Font-Ribera et al. 2013; He et al. 2017; Fossati et al. 2021). As for halo mass estimates obtained through quasar auto-correlation results, these would imply, if any, an increase in halo mass with redshift (Shen et al. 2007; Eftekharzadeh et al. 2015; Timlin et al. 2018). As there is also no observational evidence that an increase in halo mass is driving the high SB values, we conclude that they are due to the cold CGM's clumping factor increasing with time. This is a significant result as it is the first observational evidence that the density distribution of the cold gas in the CGM of

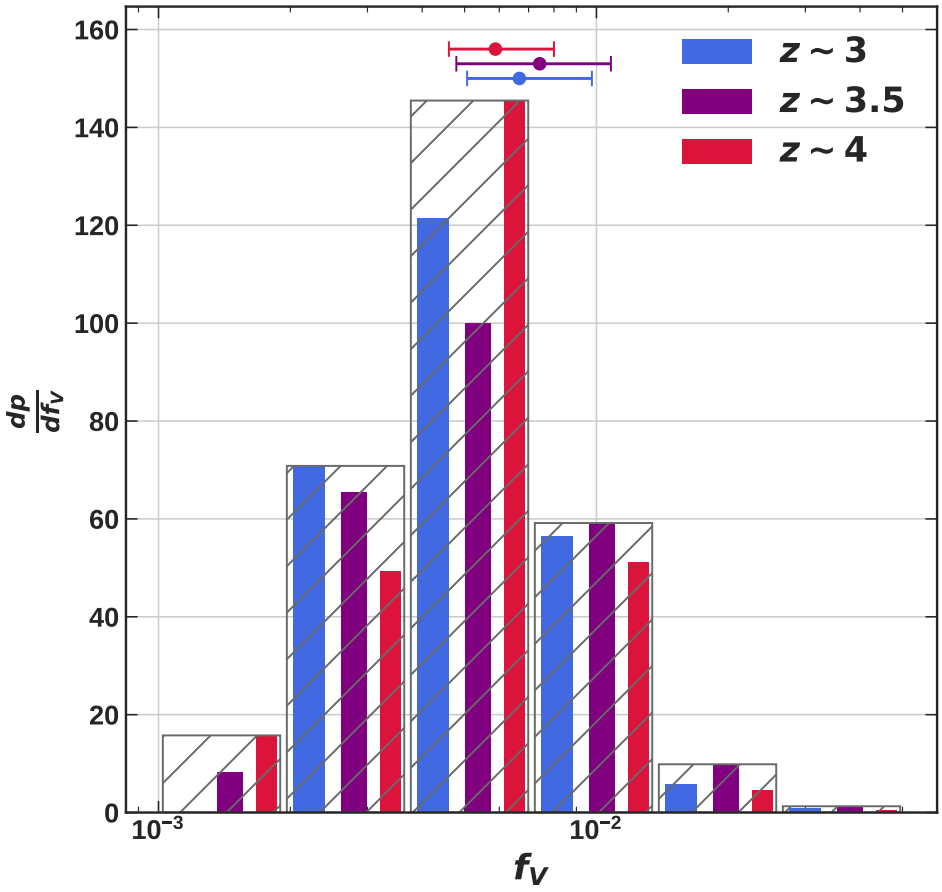

Figure 3.9: The normalised histograms of the volume filling fraction of the haloes within the mass range $10^{12.03} - 10^{12.3} \mathrm{M}_{\odot}$ at $z \sim 3$, $z \sim 3.5$ and $z \sim 4$. The colours and formatting are analogous to those of Figure 3.8. The median volume fractions at each redshift marked at the top of the figure show no evidence for any redshift evolution. As with the cold gas fraction, the volume filling fraction is therefore not responsible for the deviation of the simulated SB values' redshift scaling from the theoretically predicted scaling of $(1 + z)^5$.

quasars increases with time. We discuss what physical mechanisms could be causing this increase and its implications in Sections 3.4.2 and 3.4.3.

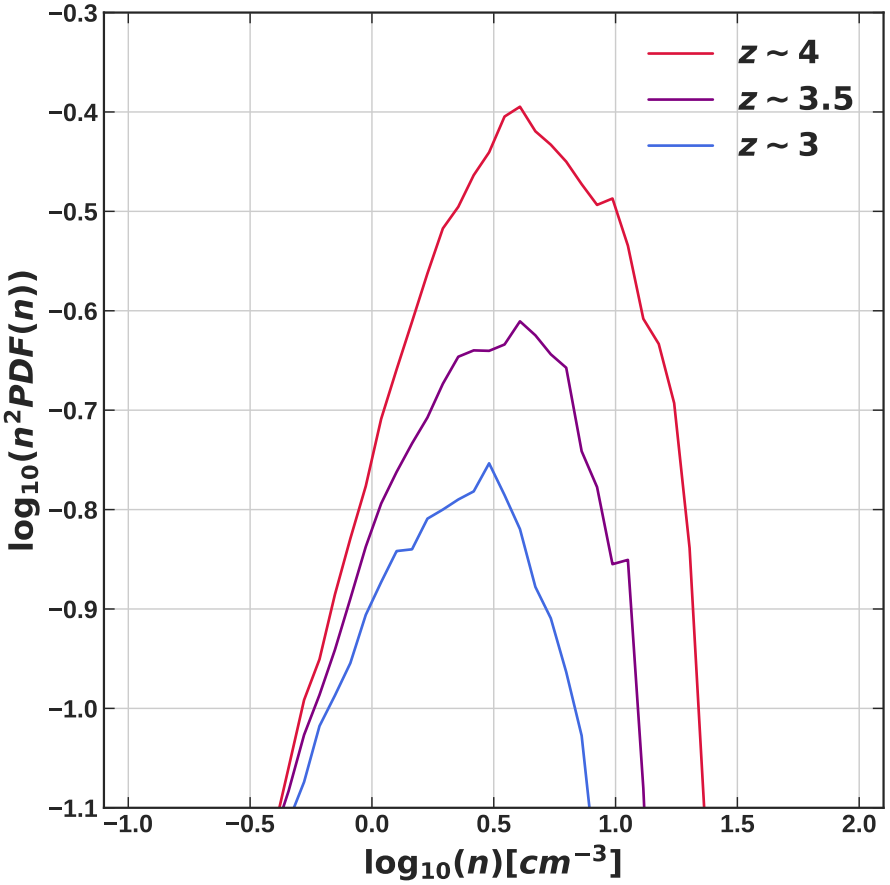

Figure 3.10: The average, normalised distributions of the squared density of the cold gas in the CGM of simulated haloes with masses between $10^{12.03}$M$_\odot$ and $10^{12.3}$M$_\odot$ at $z \sim 3$, $z \sim 3.5$ and $z \sim 4$. The broadness of the density distribution clearly increases with redshift, driving the increase in SB values with redshift.

3.4 Discussion

3.4.1 Modelled Lyα emission

As already explained in Section 3.2.2, we model the Lyα emission from the cold CGM under the assumption of maximal fluorescence and that recombination radiation dominates with respect to contributions from collisional excitation and photon pumping. The plausibility of the first assumption depends on the cold gas in the CGM not being self-shielded to the ionising radiation from the central quasar. Based on the derivation in Pezzulli & Cantalupo (2019), we argue in Chapter 2 that the MQN sample's median SB profile translates to a neutral column density ($N_{\rm HI}$) of cold gas clouds in the CGM that can be expressed in terms of the covering factor as seen by the quasar (f_c), the total halo mass in units of 10^{12}M$_\odot$ (M_{12}) and the gas's

temperature in units of 10^4 K

$$N_{\rm HI} \simeq 1.6 \times 10^{15} \left[\frac{r}{30{\rm kpc}}\right]^{-0.5} T_4^{0.21} f_c^{-1} M_{12}^{1/3} {\rm cm}^{-2}. \tag{3.15}$$

The two key ingredients that go into this calculation of $N_{\rm HI}$ are that the SB profile can be de-projected to a density profile $n(r)$ that depends on the volume filling fraction (f_v) and clumping factor of the gas clouds and that the photoionization rate of the central quasar Γ_i fulfils $\Gamma_i >> n \times \alpha(T)$, where n is the cold gas density and $\alpha(T)$ is the temperature dependent recombination coefficient. The density profile obtained by Pezzulli & Cantalupo (2019) from the MQN sample's median SB profile is

$$n(r) = 1.2\, C_l^{-0.5} T_4^{0.48} \left[\frac{f_v}{10^{-3}}\right]^{-0.5} \left[\frac{r}{30{\rm kpc}}\right]^{-1.25} {\rm cm}^{-3}. \tag{3.16}$$

As the de-projection of the SB profiles is applicable irrespective of redshift and the observed SB values also remain constant with redshift (see Figure 3.7), the cold gas density profile quoted above can be used to describe the cold gas density of the nebulae in the MAGG and MUSEUM samples as well. As for the intensity of the ionising radiation, following the calculation in Arrigoni Battaia et al. (2015), Pezzulli & Cantalupo (2019) convert the MQN sample's i-band magnitudes to a photoionization rate of $\Gamma_i \simeq 10^{-7}(r/30{\rm kpc})^{-2}{\rm s}^{-1} >> n \times \alpha(T)$. As the i-band magnitudes of the quasars contained in the MAGG and MUSEUM samples are comparable to those of the MQN quasars, their photoionization rates plausibly satisfy this assumption. The implication being, that for covering factors $f_c > 10^{-2}$ the neutral column density of the cold gas in all three of the samples is well below the self shielding limit of $\log_{10}(N_{\rm HI}) = 17.2$. From there it follows that the gas clouds in the CGM are transparent to the quasar's ionising radiation and can efficiently emit recombination radiation, implying our initial assumption of maximal fluorescence is self-consistent. In Section 3.4.5 we explore the consequences of relaxing the assumption of maximal fluorescence by varying the opening angle of the ionisation cone.

As already mentioned in Section 3.2.2, the contribution to the emission due to collisional excitation is negligible compared to that of the recombination radiation. Costa et al. (2022) include collisional excitation when modelling Lyα emission from the CGM around quasars at $z \sim 6$ and find that collisional excitation is subdominant in the central regions of the nebulae but leads to a flattening of the SB profile at larger radii. Whether the inclusion of collisional excitation would have the same effect on the SB profiles at $z \sim 3$, ~ 3.5 and ~ 4 is not clear. Furthermore, it is interesting to note that a flattening of the simulated Lyα SB profiles shown in Figure 3.6 would lead to a greater tension with the observed profiles of the MAGG sample, as these match the shape of the simulated profiles surprisingly well. Concerning the effect of photon pumping, incorporating the scattering of Lyα photons from the broad line region of the quasar to scales of above 10 kpc can have the effect of flattening the central region of the simulated SB profiles, see Figure 4 in Costa et al. (2022) and Gronke & Bird (2017). Based on the more convex shapes of the observed Lyα SB profiles at $z \sim 3$ with respect to the simulated ones in

Figure 3.6, including a treatment of the photon pumping could potentially yield a better agreement between simulated and observed profiles. However, Langen et al. (2023) measure Lyα/Hα flux ratios of three Lyα nebulae at $z \geq 2$ and find that they are constant as a function of projected distance to the central, ionising source. This, coupled with the low values of the ratios indicates that the distance dependent mechanism of photon pumping is not strong enough to plausibly alter the shape of the SB profiles. Leibler et al. (2018) also measure a low overall Lyα/Hα flux ratio for the Slug Nebulae (Cantalupo et al. 2014), indicating that recombination and not photon pumping is the dominant source of emission.

3.4.2 Density distribution of the cold CGM

The comparison of simulated and observed SB profiles hosted by haloes within a fixed mass range of $10^{12.03}$M$_\odot$ - $10^{12.3}$M$_\odot$, shown in Figure 3.6, implies that to reproduce the observed SB values the density of the Lyα emitting gas needs to reach values as high as 1 cm^{-3} at $z \sim 4$ and density values above 10 cm^{-3} at $z \sim 3.5$ and $z \sim 3$. At this point we stress again that the density values obtained in Section 3.3.2 are the maximum values that the density of the Lyα emitting gas must reach and not the overall average density of the emitting gas. Therefore, the density distribution of the cold gas should not be thought of as a delta function, as is often done to simplify matters.

According to the central limit theorem, a log-normal density distribution is the natural outcome of multiplicative, random processes, making it at an excellent starting point to describe the density distribution of a medium which is most likely subject to instabilities and turbulent processes (Vossberg et al. 2019; Augustin et al. 2021; Gronke et al. 2022). Indeed, Vossberg et al. (2019) show that the density distribution of cold, accreting filaments in a hot medium experiencing Kelvin-Helmholtz instabilities is well described by a skewed log-normal density distribution with an additional high density tail. Interestingly, the modified log-normal power law (MLP) introduced in Basu & Jones (2004) as a stellar initial mass function also consists of a log-normal distribution with a high density tail in the form of a power law. While the central limit theorem is what governs the starting distribution of the masses, interactions with the surrounding medium over varying timescales skew the distribution and lead to the power law at higher densities (Basu & Jones 2004; Basu et al. 2015). In the case of the stellar initial mass function such interactions are thought to be accretion from the ambient medium, with stellar feedback being able to shut off the accretion and thus vary the timescales over which it occurs. It is clear how this framework could also be applicable to the cold accreting gas in the CGM: The initially log-normal density distribution gains its high density tail by interacting with the hot medium through accretion via condensation and thermal instabilities (Banerjee et al. 2009; McCourt et al. 2018; Gronke & Oh 2018, 2020; Gronke et al. 2022) and loss of mass via evaporation and disruption of the cold gas (Zhang et al. 2018; Mandelker et al. 2018; Padnos et al. 2018; Mandelker et al. 2019a). And as the cold gas does not start at an initial, uniform density, it is almost guarantied that these processes occur over varying timescales. Thus the broadness of the cold gas's

density distribution, and therefore its clumping factor, would increase with time, driven by inherently random and turbulent processes.

On the observational side, Travascio et al. (in Prep.) show that the HeII/Lyα line ratios observed for the MAGG sample are predominantly consistent with a log-normal or skewed log-normal density distribution for the cold gas with an average density of 0.5 cm^{-3}. This value is consistent with the average density of the cold CGM in the EAGLE simulations (see Appendix H), indicating that although the simulations reproduce the average densities of the cold CGM, they lack the resolution to capture the physical mechanisms powering the formation of cold, high density clouds mentioned above. This conclusion is further strengthened by comparing the normalised histograms of the observed SB values and the simulated SB values. As already remarked upon in Section 3.3.2, the simulated Lyα SB maps underpredict the amount of pixels with an "intermediate" brightness ($2 \times 10^{-16} - 10^{-14}$ erg/(s cm^2 arcsec^2)), but overpredict the amount of bright pixels ($> 10^{-14}$ erg/(s cm^2 arcsec^2)). This mismatch is due to the cold gas density distribution in the simulation. In order to obtain the maximum density estimates presented in Section 3.3.2 we vary our imposed, constant SF density threshold to best match the observed Lyα SB profiles. As the metallicity dependent SF density threshold with which the EAGLE simulations differentiate the CGM from the ISM corresponds to roughly 0.1 cm^{-3} (see Figure 3.1), we are technically including cold gas from the simulated star-forming ISM when generating the mock observations. As this gas in the ISM is located in the satellite galaxies distributed throughout the host haloes, the emission from this gas becomes concentrated in a few overbright pixels leading to the overprediction of values above 10^{-14} erg/(s cm^2 arcsec^2). It is important to stress at this point, that we do not claim that emission from the ISM actually contributes to the observed SB profiles, but that the simulations lack the resolution to capture the physical mechanisms responsible for the formation of cold, high density clouds in the CGM and thus underestimate the broadness of its density distribution, as has been shown in numerous other studies (Cantalupo et al. 2014; Vossberg et al. 2019; Hummels et al. 2019; Liang & Remming 2020; Corlies et al. 2020; Augustin et al. 2021; Gronke et al. 2022). Thus, if the CGM was properly resolved it would contain cold, dense clouds diffusely distributed, which contribute to the SB values in the range of $2 \times 10^{-16} - 10^{-14}$ erg/(s cm^2 arcsec^2) and the gas in the ISM of the satellite galaxies would not need to be included in order to match observations.

3.4.3 Formation of cold gas clouds in the CGM

As already mentioned in the Introduction, the existence of cold, inflowing filaments of gas penetrating deep into the CGM of haloes within our mass range at $z > 2$ is predicted in theory (Dekel & Birnboim 2006; Dekel et al. 2009) and confirmed by both simulations (Kereš et al. 2005; Ocvirk et al. 2008; van de Voort et al. 2011a; Faucher-Giguère et al. 2011) and observations (e.g., Cantalupo et al. 2014; Martin et al. 2014; Borisova et al. 2016; Fumagalli et al. 2017; Augustin et al. 2021). At the interface between these cold filaments and the surrounding, virialised medium,

Kelvin-Helmholtz instabilities are expected to form. Depending on the diameter of the cold gas filaments, these instabilities can completely disrupt the filaments or merely disturb the outer layers of the filaments (Mandelker et al. 2016; Padnos et al. 2018; Mandelker et al. 2019a), resulting in the formation of individual clouds and a broader density distribution (Vossberg et al. 2019). Turbulent compression within the cold filaments themselves can also lead to the formation of colder, denser clumps which grow through accretion via condensation or mergers (Banerjee et al. 2009). In addition to the cold gas clouds originating in the filaments, multiple simulations show that cold gas clouds can form through thermal instabilities in hot outflows powered by feedback events (McCourt et al. 2018; Gronke & Oh 2018, 2020; Gronke et al. 2022) and then fall back towards the central galaxy (Nelson et al. 2020). However, the majority of studies find that the cold gas clouds formed in this way exhibit low densities in the range of 0.01 - 0.1 cm^{-3}. Intriguingly, Mohapatra et al. (2022) show that the inclusion of compressive turbulence, in addition to the more commonly implemented solenoidal turbulence, when modelling hot, turbulent outflows driven by stellar and AGN feedback leads to the formation of cold clouds with densities of the order of 1 - 10 cm^{-3}. It is therefore possible, that the increase of the clumping factor with time inferred in Section 3.3.3 is caused by an increase in turbulence of the hot CGM with time.

We find it plausible that both filamentry accretion with subsequent instabilities and thermal instabilities in a hot turbulent medium contribute to the cold, emitting gas in the CGM, though in different regions. Close to the central galaxy, cold gas from both the surviving filaments and thermal instabilities could contribute equally to the Lyα emission. However, unless feedback is so strong that it drives turbulence throughout the hot phase of the CGM, on larger scales the main source of cold gas is cosmic accretion at the redshifts considered in this work (Kereš et al. 2005; Dekel & Birnboim 2006; Brooks et al. 2009; Joung et al. 2012b). This picture is also favoured by the fact that the asymmetry of Lyα nebulae around bright quasars is positively correlated with the extent of the nebulae (Arrigoni Battaia et al. 2019a; den Brok et al. 2020). Indicating that at larger scales the emission traces the inherently asymmetric accretion from the cosmic web.

3.4.4 Survival of cold gas clouds in the CGM

Having discussed possible origins and formation mechanisms for the cold gas, we now turn to its survival. Mandelker et al. (2019a) estimate that the cold gas filaments' radii need to exceed 0.5 - 5% of the halo's virial radius in order to survive. Conservatively, the radii of the cosmic web filaments would therefore need to be larger than 5 kpc. Visual inspection of the SB maps of the Lyα nebulae included in this study reveals that extended, asymmetric emission (see e.g., nebulae 1 and 3 in Borisova et al. 2016) tracing the filaments typically has widths an the scale of multiple MUSE resolution elements, which are roughly 5 kpc. It is therefore likely that the filaments generally survive within the CGM and contribute to the Lyα emission.

The survival times of cold, low density clouds in a hot wind pose more of a

problem (Zhang et al. 2018), although the presence of magnetic fields (McCourt et al. 2015) and mixing layers (Gronke & Oh 2018) has been shown to extend their survival. However, as the results presented in Section 3.3.2 indicate that high density gas clouds are required to explain the observed SB values, we focus on their survival. To do so, we model the CGM as a hot and cold phase in pressure equilibrium as first proposed by Spitzer (1956). The hot phase of the simulated CGM around haloes in our estimated mass range has an average temperature and density of $\sim 2.5 \times 10^6$ K and 6×10^{-4}cm^{-3} (see Appendix I). As the virial temperature of haloes within the mass range considered is $\sim 1.7 - 2.6 \times 10^6$ K, the hot phase of the CGM is roughly at virial temperature. The cold phase's temperature is fixed by the quasar photoionization temperature floor, which we set to 5×10^4 K. For the cold phase to be in pressure equilibrium with the hot phase, a density of $\sim 3.5 \times 10^{-2}$cm^{-3} is required. Therefore, the cold gas densities of 1 - 10 cm^{-3}, needed to explain observed SB profiles, would imply that these cold, dense clouds are out of pressure equilibrium and actually over-pressurised with respect to the hot phase of the CGM by a factor of 10 -100. Clearly, this result directly depends on the photo-ionization temperature floor we set for the cold gas. Although the exact value of the minimum temperature of the emitting gas due to photo-heating likely varies slightly from halo to halo and may even vary within the CGM of a single halo, the temperature of the cold phase would have to be as low as $\sim 1.7 \times 10^3 K$ for the cold, dense gas to be in pressure equilibrium with the hot phase. Increasing the temperature and/or density of the the hot phase could result in the cold, dense gas being in pressure equilibrium with the hot phase, however, the temperature of the hot gas is comparable to the virial temperature, making an even higher value unlikely. Indeed, Lochhaas et al. (2021) find that in the FOGGIE simulations (Peeples et al. 2019) the temperature of the hot gas of halos which is in hydrostatic equilibrium is lower than the theoretical virial temperature by a factor of roughly 2. They show that the kinetic energy of non-thermal motions, such as turbulence and bulk-outflows, significantly contributes to the halo's total kinetic energy, thus lowering the required contribution from thermal motions necessary to maintain virial equilibrium. Within this context, non-thermal motions such as turbulence could be an additional, significant source of pressure support in the hot phase of the CGM (Padnos et al. 2018), as has already been shown to be the case for the intra-cluster medium (Vazza et al. 2009; Iapichino et al. 2011; Parrish et al. 2012). There is also evidence that pressure from cosmic rays can dominate over the thermal pressure in the CGM (Girichidis et al. 2018; Ji et al. 2020). Though the majority of studies find that they lend pressure support to the low density, cold gas in the CGM and prevent it from contracting, accreting onto the central galaxy and forming stars, in addition to decreasing the density contrasts within the CGM (e.g., Buck et al. 2020; Butsky et al. 2020), Owen et al. (2019) find that advected cosmic rays could plausibly introduce an additional source of pressure to the CGM's hot phase and thus effect the hydrostatic equilibrium. It is, however, worth noting at this point, that in the FIRE-2 simulations (Hopkins et al. 2018) with additional modelling of cosmic rays Hopkins et al. (2020) only find evidence of cosmic rays measurably affecting the CGM of galaxies at $z < 1$. Further complicating the matter, these models of cosmic rays only include supernovae as sources, although

AGNs are also thought to be likely sources of cosmic rays (Berezhko 2008; Aleksić et al. 2011; Blandford et al. 2019; Matthews et al. 2019; Becker Tjus et al. 2022). Hence, these findings may not be applicable to our sample of quasars and their environments.

As we are considering the survival of cold gas clouds in the vicinity of a bright QSO, it is also worth considering the effect of the radiation pressure from the QSO's broad line region. While the cold gas in the CGM is optically thin to the ionising radiation from the QSO, it is optically thick with regards to the Lyα emission both from the in-situ recombination radiation and the from the QSO's broad line region. In Chapter 2 we show that the optical depth, as seen by the Lyα photons, τ is plausibly within the range $1 << \tau < 10^4$. Thus, the typical broadening of the Lyα line is due to the Lyα photons, produced within the cloud through recombination, scattering in the cloud until they are sufficiently far away from the Lyα line centre. This high optical depth also leads to the Lyα photons from the broad line region interacting with the cold, dense gas clouds (Travascio et al. in Prep.) and therefore results in the clouds experiencing pressure due to the radiation. The ratio of this radiation pressure $P_{\mathrm{Ly}\alpha}$ and the thermal pressure P_{th} of the clouds can be written as

$$\frac{P_{\mathrm{Ly}\alpha}}{P_{th}} = \frac{EW_{\mathrm{Ly}\alpha} L_{\mathrm{Ly}\alpha}}{4\pi r^2 c} \frac{1}{n k_B T} \simeq 0.57 \left[\frac{10\ \mathrm{kpc}}{r}\right]^2 \left[\frac{0.1\ \mathrm{cm}^{-3}}{n}\right] \left[\frac{5\times10^4\ \mathrm{K}}{T}\right]. \quad (3.17)$$

Where we set the equivalent width of the Lyα line coming from the broad line region to $EW_{\mathrm{Ly}\alpha} = 0.2\mathring{A}$ and the QSO's Lyα luminosity to 4.67×10^{44} erg s^{-1}. The radial distance to the central QSO is denoted by r, c is the speed of light, n is cold gas cloud's number density, k_B the Boltzmann constant and T is the cold gas's temperature. When inserting some typical distance, density and temperature values into Equation 3.17, it becomes clear that the radiation pressure only becomes comparable to the thermal pressure in the inner CGM for the lower density clouds. Hence, while the radiation pressure may be relevant to the clouds with lower densities close to the QSO, it is not sufficient to balance the thermal pressure of the cold clouds throughout the whole CGM.

Alternatively, if the cold gas is indeed over-pressurised with respect to the hot phase of the CGM, one would expect these dense regions to expand until they are in pressure equilibrium. In Chapter 2 we show that in the EAGLE simulations the cold, Lyα emitting gas is inflowing throughout the CGM and that this scenario is compatible with the observed samples studied here. It is therefore informative to compare the expansion time t_{exp} that it would take the cold gas cloud to reach pressure equilibrium with the host halo's free fall time t_{ff}. As we are operating under the assumption of maximal fluorescence, the cold gas is continually ionised and heated (see Section 3.2.2) and would therefore expand isothermally. We follow the definition of Robinson et al. (2002), who derive the expansion time for ionised, over pressurised clouds using the Lagrangian motion for isothermal flow

$$t_{exp} = \frac{1}{\sqrt{3}} \frac{r_0}{c_s} \left(\frac{\ln f}{\ln \epsilon}\right)^{1/2}, \quad (3.18)$$

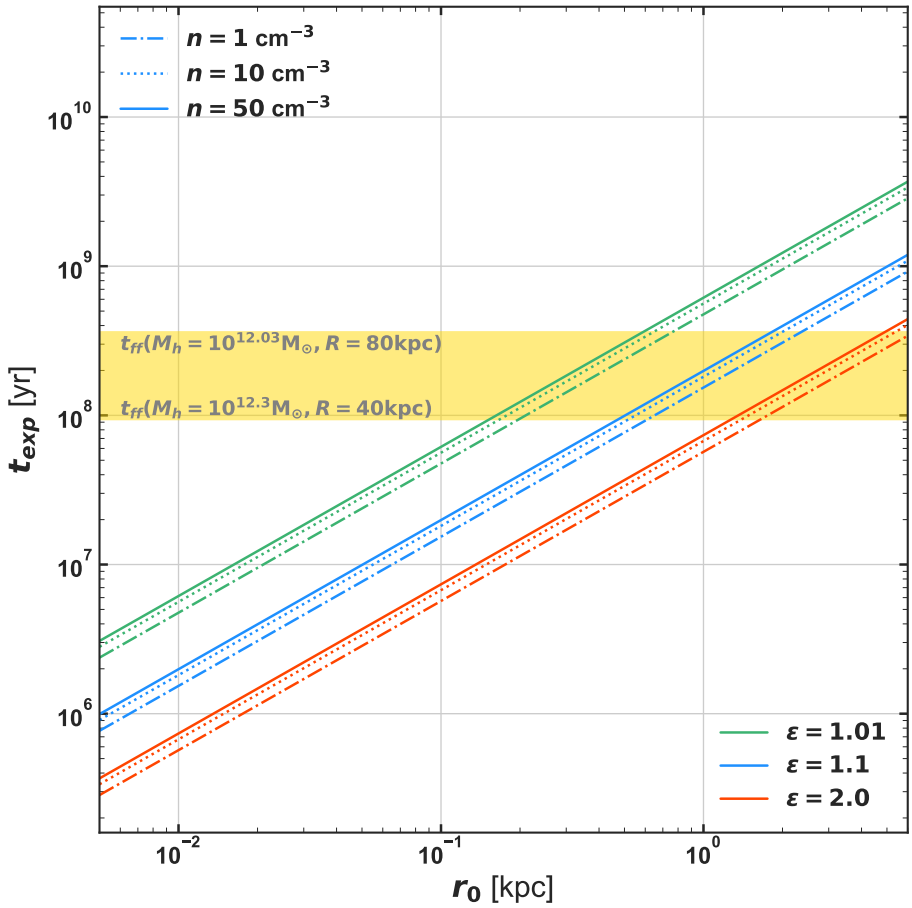

Figure 3.11: The expansion time of an over-pressurised, dense, cold (5×10^4 K) gas cloud surrounded by a warm medium as defined by Equation 3.18. We calculate the expansion time for the three initial densities $n = 1$ cm^{-3} (dash-dotted), $n = 10$ cm^{-3} (dotted) and $n = 50$ cm^{-3} (solid), as well as for three different initial density ratios $\epsilon = 1.01$ (green), $\epsilon = 1.1$ (blue) and $\epsilon = 2$ (red). We also mark the free fall times typical for the halo mass range we examine with the yellow shaded region.

where r_0 is the initial radius of the gas cloud, $c_s = \sqrt{2k_B T m_H}$ the sound speed of the cold gas, f is the ratio of the cold gas density before and after expansion and ϵ is the ratio of the cold gas density in the centre and at the edge of the cloud before expansion. In Figure 3.11 we plot t_{exp} as a function of the initial radius r_0 for three different ϵ values (plotted in green for $\epsilon = 1.01$, blue for $\epsilon = 1.1$ and orange for $\epsilon = 2.0$) and three different initial density values (plotted with a solid line for $n = 50$cm^{-3}, dotted for $n = 10$cm^{-3} and dash dotted for $n = 1$cm^{-3}). Interestingly, the density contrast between the centre of the cloud and its edge ϵ has a greater effect on the expansion time than the initial, inner density. The range of realistic free fall times for the haloes considered (free fall in a $10^{12.3}$M$_\odot$ halo from $\sim 0.5 r_{vir}$ to free fall in a $10^{12.03}$M$_\odot$ halo from $\sim r_{vir}$) are indicated by the yellow shaded region. Comparing these to the expansion times reveals that for them to be

similar, either the density profile of the cloud needs to be very flat (1 - 10% drop) or, likely more realistically, the density profile can decrease at a higher rate, but the cloud sizes need to be roughly 1 kpc. In Chapter 2 we argue that the cold gas clouds have sizes of a few 100 pc, indicating that the cold gas clouds expand on a time scale $\sim$ 10 times shorter than their free fall time. However, this does not necessarily prevent such high density clouds from significantly contributing to the observed high SB values. Firstly, the expansion time calculated with Equation 3.18 applies to an isolated cold cloud in a warm medium. While this scenario is applicable to cold clouds formed via thermal instabilities in the hot CGM, it does not apply to the cold gas clouds forming at the interface between the cold filaments and the hot CGM or to the clouds forming within the filaments due to turbulence. As a lower temperature for the surrounding medium results in a longer expansion time for the cold clouds, the times shown in Figure 3.11 should be thought of as a lower limit. Secondly, it is not necessary that the clouds survive their entire infall as long as the cloud formation mechanisms are such that they continuously replenish the cloud population. Clearly, all three mechanisms described in Section 3.4.3 fulfill this criterion. It is therefore plausible, that such over-pressurised clouds can contribute significantly to the observed Lyα emission.

3.4.5 Caveats

When deriving the density constraints of the cold gas in the CGM around quasars, we make various simplifying assumptions which allow us to compare the simulations to the observations. However, this means that there may be some caveats to our results. In particular, we assume a constant photo-heating floor, a certain halo mass range and maximal fluorescence. In this section we discuss the effects relaxing these three assumptions would have on our results and show that the density constraints obtained are indeed fairly conservative lower limits.

Constant photo-heating floor: When modelling the Lyα emission from the cold CGM, we impose a constant temperature floor of 5×10^4 K on the gas due to photo-heating from the central, ionising quasar. This is a simplifying assumption, as the temperature at which an equilibrium between heating due to photo-ionisation and cooling due to recombination radiation is reached is unlikely to be constant throughout the entire CGM. Indeed, as Pezzulli & Cantalupo (2019) show through CLOUDY modelling (Ferland et al. 2013), this equilibrium temperature depends on multiple variables, such as the gas's metallicity, density, distance to the ionising source and the shape of the ionising spectrum. As already mentioned, our simulated SB profiles should be thought of as an upper limit due to the assumption of maximal fluorescence when generating them. The recombination coefficient $\alpha(T)$ scales inversely with temperature, meaning that only an overestimation of the photo-heating floor would effect our results and conclusions presented in Sections 3.3.2 and 3.4.2. The equilibrium temperature scales inversely with metallicity for densities above $n \sim 0.2$ cm^{-3} and the temperature floor we impose corresponds to a metallicity of 0.1 Z$_\odot$ (Pezzulli & Cantalupo 2019). Therefore, a lower photo-heating floor would correspond to even higher metallicites, which seems unlikely in the cold CGM at $z > 3$.

As for gas densities below $n \sim 0.2$ cm^{-3}, these exhibit equilibrium temperatures above 7×10^4 K, again indicating that our imposed photo-heating floor underestimates the equilibrium temperature rather than overestimating it. The equilibrium temperature also scales inversely with gas density. Hence, as our imposed floor is derived for a density of $n = 1$ cm^{-3}, we are potentially overestimating the temperature of the denser gas ($n > 10$ cm^{-3}). This will have no effect on the SB profiles generated with SF density thresholds of $n_* = 0.1$ cm^{-3} and $n_* = 1$ cm^{-3} but could affect those with $n_* = 10$ cm^{-3}. However, as the majority of the cold gas exhibits densities below $n = 1$ cm^{-3} (see Appendix I) the underestimation of the lower density gas's equilibrium temperature far outweighs the overestimation of the denser gas's equilibrium temperature. For this reason, the SB profiles can still be considered an upper limit, no matter which SF density threshold is applied.

Halo mass range: In Chapter 2 we find that the kinematics of the Lyα emitting gas are consistent with a host halo mass between $10^{12.03}$ M$_\odot$ and $10^{12.3}$ M$_\odot$ or a minimum halo mass of $10^{11.97}$ M$_\odot$. In this chapter, we obtain constraints on the density of the emitting gas by comparing the observed SB profiles with those generated from haloes within the narrow mass window. This is equivalent to assuming the probability of a halo with a given mass hosting a bright quasar can be described by a top hat function. In Figure F.7 in Appendix F we compare the SB profile generated using a top hat probability function with the SB profiles generated using a step function and a Gaussian as a probability function. We set the step function to coincide with the minimum halo mass derived in Chapter 2 and the Gaussian is centred on $10^{12.16}$ M$_\odot$ with a standard deviation chosen to coincide with the upper and lower limits of $10^{12.03}$ M$_\odot$ and $10^{12.3}$ M$_\odot$. The three SB profiles are indistinguishable. Hence, simply including Lyα nebulae hosted by higher mass haloes in the sample is not sufficient to increase the brightness of the simulated profiles to that of the observed profiles. This also means, that the SB profiles of the observed nebulae cannot be used to distinguish between the top-hat and step-function scenarios. Another observable that may provide a constraint is the size distribution of the observed nebulae, as this is expected to scale with halo mass at a fixed redshift due to the SB values scaling with halo mass (see Equation 3.13). Hence, one would expect a narrow size distribution with a few outliers in the case of a narrow mass window. Whereas in the case of a minimum mass, one would expect a wide range nebula sizes, with the number of smaller nebulae outweighing that of the larger nebulae due to the shape of the halo mass function. Figure 3 of Borisova et al. (2016) shows the sizes of the Lyα nebulae considered in that work. All nebulae, bar two outliers, have sizes between 120 kpc and 180 kpc and there is no indication that there are significantly more smaller nebulae than larger ones in the sample. Considering the scatter in nebula size that is introduced by projection effects, this size range and distribution would therefore favour the scenario where quasars are hosted by haloes in a narrow mass window. However, as the sample only contains 17 nebulae, the nebula size distribution may not be adequately sampled and thus lead to the wrong conclusions. In Figure 4 of Arrigoni Battaia et al. (2019a) the distribution of the QSO MUSEUM nebulae sizes is shown. Despite the broader area distribution of these nebulae compared to the size distribution of the MQN sample, there is no evidence for a bottom heavy

distribution. Hence, the scenario of a top-hat function would seem to better match observations. Turning to the higher redshift samples, Fossati et al. (2021) provide no direct measurements of the size of Lyα nebulae in the MAGG sample, however, visual inspection of their Figures 1 and 4 indicates a size distribution consistent with that of the MQN and QSO MUSEUM samples. This suggests that a halo mass distribution characterised by a top-hat function rather than a step-function is also more likely at higher redshift. However, as already stated, a larger sample size is necessary to make a more definitive statement. We therefore do find it more likely that the quasars are hosted by haloes within a narrow mass window, but note that even if this were not the case, high gas densities and a broad density distribution throughout the cold CGM are still necessary to explain the observed SB values.

Maximal fluorescence: When generating the mock observations and subsequent SB profiles, we make the assumption of maximal fluorescence. This is akin to assuming that the opening angle of the ionising cone due to the central quasar is 180°. At lower redshift there is evidence for opening angles that vary from object to object in the range of $60° - 120°$ (Schmitt & Kinney 1996; Fischer et al. 2013; Ezhikode et al. 2017; Zhang 2023; Li & Shen 2023). At higher redshift the picture is even less clear. Obreja et al. (2023) find tentative evidence for an opening angle of at least 60° by comparing mock observations of the CGM with observational constraints on the Lyα, HeII and CIV SB profiles, as well as optically thick absorbers. However, as they note, the black hole masses and Eddington ratios of the central AGNs also have an effect on the observables. To gauge the effect of a lower opening angle on our results, we generate SB profiles from mock observations of the haloes in the relevant mass range for a variety of opening angles between 60° and 120°. Unsurprisingly, lower opening angles result in lower SB values as can be seen in Figure J.11. Opening angles below 120° also result in slightly steeper SB profiles. As already stressed in Section 3.3.1, the simulated SB profiles produced in this work are upper limits. Even if the opening angle were less than 180°, the density constraints obtained would still be valid, as a lower opening angle implies lower simulated SB values and would thus imply even higher densities in the cold CGM than those obtained.

3.5 Conclusion

The wealth of spectroscopically observed Lyα nebulae at $z \gtrsim 3$ associated with bright quasars presents an opportunity to constrain the physical properties of the cold CGM at high redshifts, specifically, the cold gas's density and kinematics. Apart from the standard limitations of observations (i.e., faintness of the emission, noise and seeing conditions), the spatial and spectral resolution of the current generation of telescopes is such that the emitting structures are unresolved. This results in the unresolved gas's clumping factor being greater than one, but still unconstrained. Thus it is not possible to derive the emitting gas's density directly from its emissivity. Additionally, the resonant nature of the Lyα line hampers the interpretation of the observed kinematics. On the other hand, even though simulations supply the density and kinematics of each individual simulated element, the current generation of large

scale simulations also lack the resolution to entirely resolve the cold gas structures in the CGM. Hence, density variations on small scales cannot be captured by the simulations and they are unable to capture the physical mechanisms which govern the physical state of the cold CGM. While small scale hydrodynamic simulations have made significant strides in constraining both the smaller scale properties of the gas and the physical mechanisms shaping these properties, they do not simulate the cosmological context in which these processes occur.

Individually, both observations and simulations posses specific limitations which hamper the precise characterisation of the cold CGM's properties. Therefore, instead of focusing solely on observations or simulations, we utilise both methods in tandem to constrain the density of the cold, emitting CGM by comparing the brightness of the observed Lyα nebulae to the brightness of the simulated Lyα nebulae. Such a comparison only becomes meaningful once the mass of the haloes hosting the quasars and their associated Lyα nebulae is sufficiently constrained. This is due to the degeneracy between the nebulae's SB, clumping factor and host halo mass, as explained in Section 3.2.4. Chapter 2 is dedicated to developing a new method of constraining quasar halo masses using the kinematics of the Lyα emitting gas. With this novel method we show that the characteristic halo mass of bright quasars at $z \sim 3-4$ is in the range of $10^{12.03}$ $M_\odot$ - $10^{12.3}$ $M_\odot$. With this halo mass range in hand, the entirety of this chapter is dedicated to constraining the physical characteristics of the high redshift, cold CGM by comparing observations and simulations of Lyα nebulae.

Taking advantage of the range of halo masses and redshifts afforded by the EAGLE simulations, we first investigate in which way the nebulae's SB, the CGM's cold gas fraction, cold gas volume filling fraction and clumping factor scale with halo mass and evolve with redshift in the EAGLE simulations. In Section 3.3.1 we show that the CGM's cold gas fraction scales as $f_{cold} \propto M_h^{-0.7}$ and that the cold gas volume filling fraction scales as $f_v \propto M_h^{-0.16}$, resulting in the simulated SB values scaling as SB $\propto M_h^{1.7}$ regardless of redshift. Focusing on the simulated SB values of haloes within the mass range obtained in Chapter 2, we generate Lyα SB profiles from the simulations applying three different density thresholds which differentiate the CGM from the ISM. We compare the samples of observed Lyα nebulae at $z \sim 3-4$ presented in Borisova et al. (2016), Arrigoni Battaia et al. (2019a) and Fossati et al. (2021) with the simulated SB profiles at the corresponding redshifts. The comparison in Section 3.3.2 reveals that the cold gas in the CGM needs to reach densities of 1 - 10 cm^{-3} to explain the observed SB values. Additionally, we show that while the simulated SB values roughly evolve with redshift as theoretically predicted, the observed SB values exhibit a negligible redshift evolution and that they are unexpectedly bright at $z \sim 3$ with regard to $z \sim 4$. We argue that this "increase" in SB is due to the cold CGM's clumping factor increasing with time. An increase in the clumping factor means an increase in the broadness of the cold gas's density distribution, which in turn translates to an increasing maximum density of the cold, emitting CGM with time. As already mentioned in Vossberg et al. (2019), one physical mechanism linked to the CGM's clumping factor is its turbulence. An increase in the CGM's turbulence with time is therefore one plausible driver of the

apparent increase in clumping factor and the unexpectedly bright SB values. The high density values implied by the brightness of the observed nebulae naturally lead to questions concerning to formation of such high density gas clouds and their survivability. In Section 3.4.3 we argue that the high density gas forms from the cold, accreted gas due to Kelvin-Helmholtz instabilities and turbulent compression, as well as from the turbulent, hot medium due to thermal instabilities. The combination of multiple formation mechanisms is compatible with the broad, log-normal density distribution of the cold gas indicated by the observed SB values and SB histograms (see Figure 3.6). Concerning the survival of the gas clouds, we show that although they are likely over-pressurised with respect to the hot CGM and thus expand while accreting from the Cosmic Web, they do so on timescales of 1-10 % of their free fall time. As the population of gas clouds is continually replenished due to Kelvin-Helmholtz and thermal instabilities, these high density gas clouds can plausibly contribute to the Lyα emission throughout the entire CGM. Taken together, these results imply that at $z \sim 3-4$ the cold CGM exhibits density variations below the current resolution scales of both observations and simulations, that it reaches high densities and is turbulent, with the turbulence increasing with time.

Further analysis is necessary to confirm the picture of an increase in the cold CGM's clumping factor driven by an increase in turbulence. Future, high resolution zoom-in simulations of the high redshift CGM will help us understand how gas accretes from Cosmic Web filaments into the CGM and onto the galaxies themselves, as well as the state of the accreted gas. Similar insights concerning the low redshift CGM have already been obtained using such zoom-in simulations at low redshifts (Peeples et al. 2019; Lochhaas et al. 2021; Nelson et al. 2020; Lochhaas et al. 2023). Observations of non-resonant emission lines such as H-Hα or HeII from the CGM at high redshift will also contribute to a clearer picture. Specifically, the ratios of resonant and non-resonant lines can be used to constrain the clumping factor of the emitting gas (Cantalupo et al. 2019, Travascio et al. in Prep.). The turbulence of the gas can be measured by calculating the structure functions of velocity maps obtained from sufficiently bright non-resonant emission, as is done in Chen et al. (2023) for OII and OIII emission nebulae around bright quasars at $z \lesssim 1$. Current, ground based observations of HeII nebulae around bright quasars at $z \gtrsim 3$ still lack the depth to perform such precise kinematical measurements of the turbulence, but hopefully this situation will change in the near future with upcoming, large programs. Observations of Hα emission by the James Web Telescope will also provide an excellent opportunity to further constrain the dominant emission mechanism of the cold gas, its clumping factor and kinematics.

Chapter 4

Concluding Remarks

Without a doubt, future, higher resolution simulations and observations will be important in furthering our understanding of how gas flows from the Cosmic Web filaments into the CGM of galaxies. Specifically on the observational side, detections of non-resonant emission will be essential to future studies. The way in which these future observations and simulations could resolve the gaseous structures and the physical processes shaping them has already been discussed in the previous chapters, as well as how observations of non-resonant lines will further our understanding of the gas's clumping factor, kinematics and the dominant emission mechanism. In this final chapter I discuss possible future avenues of inquiry that do not involve increasing the resolution of previous studies or turning to other emission lines.

In Chapter 2, specifically Section 3.3, I show that the kinematics of the simulated Lyα nebulae are consistent with observed HeII kinematics, indicating that the EAGLE simulations reproduce the large scale kinematics of the high redshift, cold CGM. In Appendix D, I also show that the AGN-feedback implementation in the EAGLE simulations has a negligible effect on the large scale kinematics and properties of the cold CGM. At the same time, in Section 3.4.3 I argue that turbulence on scales below the resolution level is a likely cause of the cold gas's broad density distribution, inferred from the observed Lyα SB values. Some of the inferred high density gas clouds are associated to turbulence in the cold, Cosmic Web filaments themselves in the form of turbulent compression and Kelvin-Helmholtz instabilities at the surface of the filaments. On the other hand, turbulence driven by stellar and/or AGN feedback can also cause thermal instabilities which lead to formation of cold, dense gas clouds within the hot phase of the CGM. As the Lyα nebulae studied in this work are all associated with bright quasars, it is possible that in addition to the boost in emission due to the quasar fluorescence, the high brightness levels of the nebulae are also due to the presence of additional cold gas clouds in the hot CGM, who's formation is facilitated by feedback from the quasar itself. Thus, while feedback from the central quasar may not affect the large scale kinematics or properties of the cold gas, it could potentially be the driver of the small scale kinematics in the hot phase and thus crucial to the formation of part of the population of high density cold gas clouds. Although AGN and AGN-feedback have become crucial ingredients in our understanding and modelling of the evolution of galaxies

and their environments, the precise details of the lifetime of quasars and AGN are still not precicely understood. For example, the role that thermal, mechanical and radiative feedback from AGN plays in quenching star formation by disrupting the cold gas accretion from the Cosmic Web is well established. However, there is also evidence that bright quasars preferentially reside in strongly star forming galaxies, implying that the cold gas fuelling star formation is also responsible for fuelling the central black hole's accretion and thus powering the bright emission from quasars. One possible interpretation of this, is that the luminous and feedback phases of a quasar's life cycle do not occur concurrently, but one after another. As the Lyα nebulae are observed during the luminous phase of the associated quasars's life cycle, the supposed feedback driving the turbulence in the hot CGM may in fact be qualitatively different to the AGN-feedback commonly invoked to regulate star formation. Alternatively, it could be stellar feedback driving turbulence in the hot phase in the CGM which leads to the formation of cold, dense gas clouds. One way of differentiating between the two scenarios, would be to constrain the density distribution of Lyα emitting gas in nebulae associated with star forming galaxies that host neither an AGN nor quasar. However, this is complicated by the fact that the assumption of maximal fluorescence is not valid around such star forming galaxies. Another approach could be to turn to smaller scale simulations of quasars which specifically track the evolution of quasars and the effect on their surroundings. Such an analysis would help us understand whether the UV-bright quasars solely ionise their entire CGM or whether they also lead to a broadening of the CGM's cold gas density distribution and thus additionally boost the brightness of the associated Lyα nebulae.

Another avenue to be explored in the future, is the effect of the orientation of the Cosmic Web on the properties on the observed Lyα nebulae. For instance, if the filament is oriented along the line of sight towards the observer, one expects the observed nebulae to be close to spherically symmetric and to only extend as far as the diameter of the filament. In contrast, I would expect the observed velocity dispersion values to be higher than average. This is because the velocity of gas accreting along the filaments from both "behind" and "in front" of the central galaxy is completely along the line of sight, leading to high velocity dispersion values. Conversely, if the same filament is oriented perpendicularly to the line of sight, the observed Lyα nebula would be more elongated and extend as far as the ionising radiation reaches. As the gas predominantly flows along the filaments, and therefore perpendicular to the line of sight, the observed velocity dispersion values would be lower than average. Thus, the same object viewed from two different angles may exhibit differing morphologies and velocity dispersion values. Additionally, based on the arguments outlined above, I would expect the measured velocity dispersion values to be anti-correlated with both the extent and symmetry of the Lyα nebulae. This hypothesis is worth investigating with both simulated and observed Lyα nebulae as it could be possible to develop a method of constraining the orientation of the Cosmic Web filaments hosting the haloes and quasars with the observed velocity dispersion values and observed morphology of the Lyα nebulae.

In the same vein, the scatter evident in Figure 2.5 also shows that projection ef-

fects can lead to differing velocity dispersion ratios $\eta_{40-100}^{140-200}$ for the same halo viewed from a different angle. This is the reason why the mass estimation developed in Chapter 2 can currently only be applied to a population of Lyα nebulae to obtain a characteristic halo mass for the whole sample. This limitation could be overcome if the underlying cause of the scatter were better understood. In Figure 2.5, only two parameters are investigated: The velocity dispersion ratio $\eta_{40-100}^{140-200}$ and the host halo's mass. Thus, by extending the analysis to more dimensions by including, for instance, the area, asymmetry and velocity dispersion values of the Lyα nebulae one could constrain the cause of the aforementioned scatter. This would be the case if the scatter in the relation between halo mass and $\eta_{40-100}^{140-200}$ is actually caused by projecting the data points from the manifold created by the area, morphology, velocity dispersion values, ratio and halo mass down to the lower dimensioned manifold made up of the ratio $\eta_{40-100}^{140-200}$ and halo mass. Complicating matters, it is not trivial to derive a theoretical or empirical relation between five variables. One possible way around this difficulty is to apply various machine learning techniques to the data set. The simplest approach would be to encode the individual nebulae's asymmetry and size into individual variables and then use a deep neural network to derive a relation between the four input variables and the quasar halo mass. A more sophisticated approach would be to directly apply a convolutional neural network to the two dimensional SB maps of the simulated Lyα nebulae to analyse their morphology and then combine this with a neural network which takes the velocity dispersion values and ratios as an input. Clearly, any other observable trait could additionally be included as an input variable. Developing a better understanding of how all these variables relate to one another will lead to a more precise mass estimation method, that could even be applied to individual Lyα nebulae.

The lines of inquiry suggested above are only three of the innumerable ways in which the research presented in this work could be continued. What is clear, is that our understanding of the Cosmic Web and its interface with galaxies, the CGM, will not be furthered by only observations or only simulations, but a synergy of the two. It is also evident, that this field is still in its infancy with much still to be discovered. I look forward to the future revelations of the field and discovering what the community got right about the Cosmic Web, but even more so, I look forward to learning which assumptions and deductions will have to be revised.

A Effect of Star-Formation density threshold on η

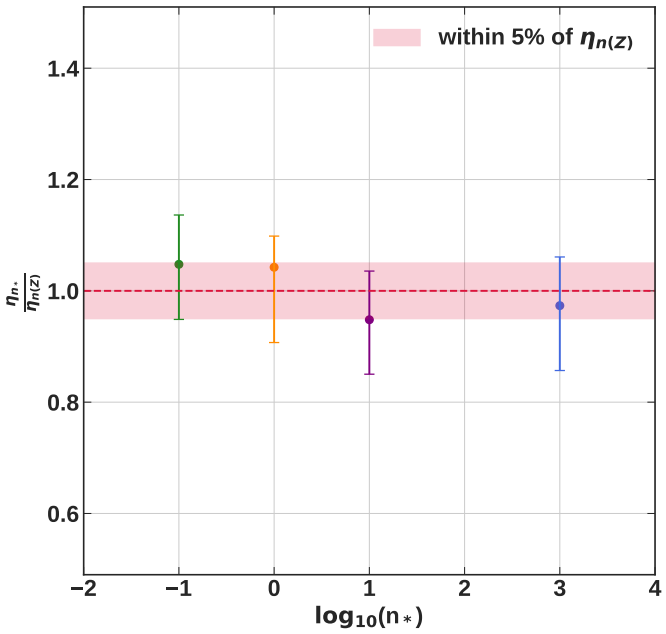

Figure A.1: The median ratios between $\eta_{40-100}^{140-200}$ calculated for Lyα nebulae with a fixed star-formation density threshold and $\eta_{40-100}^{140-200}$ using a metallicity dependent star-formation density threshold. The dotted line marks the ratio 1.0 and the red shaded area marks the region between 0.95 and 1.05. The points mark the median ratios for $n_* = 0.1$ cm^{-3} (green), $n_* = 1$ cm^{-3} (orange), $n_* = 10$ cm^{-3} (purple) & $n_* = 10^3$ cm^{-3} (blue), with the error bars marking the extent of the 25th and 75th percentiles.

As explained in Section 3.2.1, the gas in the multi-phase ISM is not resolved in cosmological simulations. The EAGLE and ENGINE simulations deal with this by allowing the gas above a metallicity dependent density threshold (see Equation 3.1) to be star-forming and deriving its properties from an effective equation of state and not from its hydrodynamics. To check whether our empirical relation depends on the star-formation density threshold chosen, we re-generate the mock cubes for a random subset of halos at $z \sim 3.5$ in the mass bin 10^{12}M$_\odot$ - $10^{12.4}$M$_\odot$ using various star-formation density thresholds. We find that the median $\eta_{40-100}^{140-200}$ of the Lyα nebulae generated using the star-formation density thresholds 0.1, 1, 10 and 10^3 cm^{-3} are all within 5 % of the median $\eta_{40-100}^{140-200}$ of the Lyα nebulae generated using the metallicity dependent star-formation density threshold, as demonstrated in Figure A.1. Our results are thus independent of this particular choice, which would be however very relevant for the SB values as will be discussed in detail in Paper II.

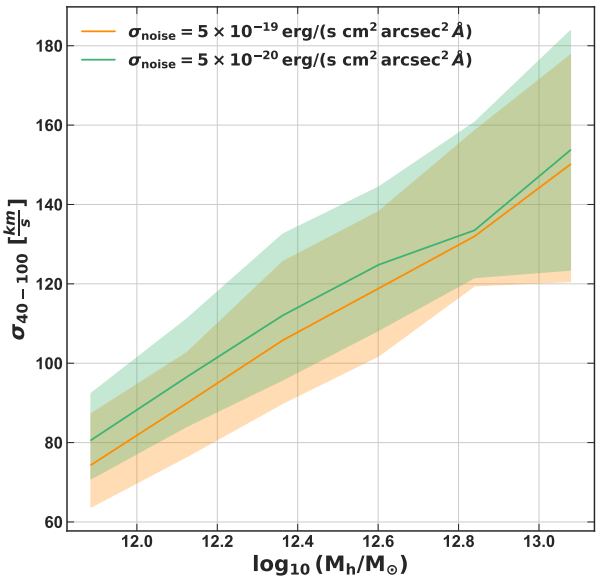

Figure B.2: The median intrinsic velocity dispersion in the inner annulus, σ_{40-100}, as a function of halo mass for all three simulations and both redshifts ($z \sim 3.5$ and $z \sim 3$) included in this analysis. We calculate σ_{40-100} for Lyα nebulae extracted from mock cubes with $\sigma_{\rm noise} = 5 \times 10^{-19}$ erg/(s cm^2 arcsec^2 Å) (orange line) and $\sigma_{\rm noise} = 5 \times 10^{-20}$ erg/(s cm^2 arcsec^2 Å) (green line). The shaded regions indicate the 25th and 75th percentiles. Despite $\sigma_{\rm noise}$ varying by an order of magnitude the two median σ_{40-100} are consistent with each other.

B Effect of observational noise on the intrinsic velocity dispersion

We quantify the effect of varying the amount of noise added to the mock cubes, as described in Section 2.2.2, by comparing the median intrinsic velocity dispersion in the inner annulus, σ_{40-100}, of Lyα nebulae extracted from mock cubes generated using Gaussian noise with a standard deviation of $\sigma_{\rm noise} = 5 \times 10^{-19}$ erg/(s cm^2 arcsec^2 Å) and $\sigma_{\rm noise} = 5 \times 10^{-20}$ erg/(s cm^2 arcsec^2 Å). The inner annulus extends from ∼40 ckpc to ∼100 ckpc. In Figure B.2 we plot the median σ_{40-100} of all three simulations and both redshifts ($z \sim 3.5$ & $z \sim 3$) included in this analysis as a function of halo mass. The orange solid line denotes the median σ_{40-100} calculated from mock cubes with $\sigma_{\rm noise} = 5 \times 10^{-19}$ erg/(s cm^2 arcsec^2 Å) and the green solid line corresponds to the $\sigma_{\rm noise}$ used in this analysis: 5×10^{-20} erg/(s cm^2 arcsec^2 Å). The shaded area denotes the 25th and 75th percentiles. Despite a slight decrease in σ_{40-100} with the higher $\sigma_{\rm noise}$, the behaviour of σ_{40-100} as a function of halo mass is independent of the noise level chosen and the two median σ_{40-100} are consistent with each other, indicating that the behaviour of the intrinsic velocity dispersion is not dominated by the Gaussian noise added to the mock cubes.

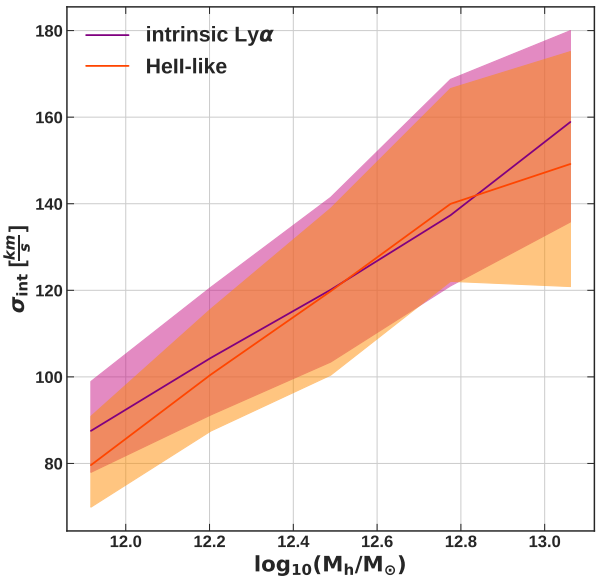

Figure C.3: The median intrinsic velocity dispersion in the inner annulus, σ_{40-100}, with (orange line) and without (purple line) a re-normalisation of the SB values in the mock observations by a factor of 0.2. The shaded areas indicate the extent of the 25th and 75th percentiles. The re-normalisation leads to fainter, "HeII-like" nebulae. The good agreement of the two median σ_{40-100} as a function of halo mass demonstrates that the intrinsic velocity dispersion is not qualitatively affected by any normalisation of the surface brightness, provided the nebula is still detected with two spectral layers.

C Effect of SB normalisation on the intrinsic velocity dispersion

As discussed in the Introduction and Section 2.2.2, the actual value of the Lyα SB depends on several factors, including the sub-grid clumpiness of the medium which is in turn dependent on the simulation's spatial resolution and physics included in the model. On the other hand, some of the observations used here have noise values which would make part of the CGM undetectable with respect to the mock observations presented in this work. Similarly, the HeII-Hα emission is a factor of a few fainter than Lyα emission. How do these SB variations affects the velocity dispersion maps used in this work? In order to address this question, we re-generate a subset of the mock observations with a lower SB normalisation. In particular, we produce "HeII-like" nebulae in the mock observations by re-normalising the calculated emissivity values by a factor of 0.2 before adding Gaussian noise and applying Gaussian smoothing as detailed in Section 2.2.2. We then compare the median intrinsic velocity dispersion in the inner annulus, σ_{40-100}, of the simulated Lyα nebulae with the σ_{40-100} of the "HeII-like" nebulae. This comparison is shown in Figure C.3, where the median σ_{40-100} of the Lyα nebulae as a function of halo mass is plotted with

a solid purple line and the median σ_{40-100} of the "HeII-like" nebulae as a function of halo mass is plotted with a solid orange line. The respective 25th and 75th percentiles are indicated by the shaded areas. The close agreement of the two medians indicates that the behaviour of the intrinsic velocity dispersion is not affected by a re-normalisation of the SB values, provided the nebula is still detected with two spectral layers.

D Effect of AGN-feedback on the Gas Kinematics

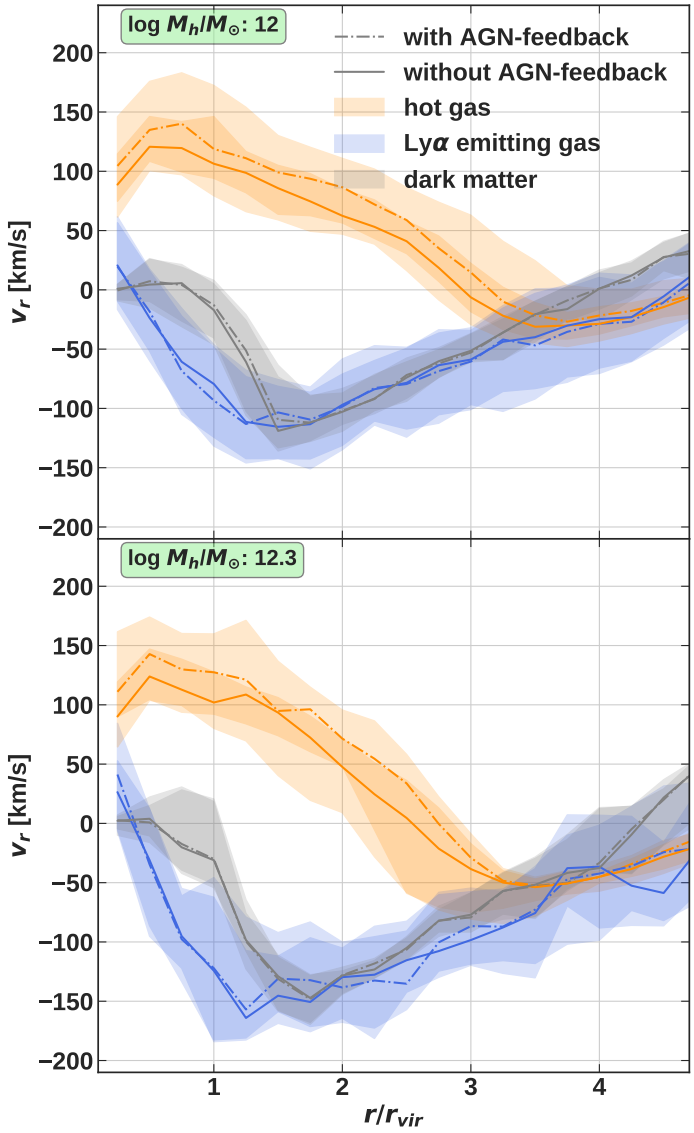

Figure D.4: Spherically averaged radial velocity profiles of the dark matter (grey), Lyα emitting gas (blue) and hot ($> 10^5 K$) gas (orange) with (dash-dotted line) and without (solid line) AGN-feedback at redshift $z \sim 3.5$.

To quantify the effect of the AGN-feedback on the kinematics of the gas in the ENGINE simulations, we directly compare the radial velocity profiles of the gas and dark matter in the NoAGN and RECAL simulations at redshifts $z \sim 3.5$ (Figure D.4) and $z \sim 3$ (Figure D.5). Analogously to Figure 2.2, the median radial velocity profiles for different halo mass bins of the hot gas ($> 10^5 K$) are shown in orange, those of the Lyα emitting gas in blue and those of the dark matter in grey. The 25th and 75th percentiles are indicated by the shaded regions. The profiles with the dash-dotted lines are extracted from the RECAL simulation (where AGN-feedback is implemented) and those with solid lines from the NoAGN simulation. Unsurprisingly, the radial profiles of the dark matter are completely unaffected by the change in baryonic physics implementation. Although stellar feedback is main cause for the hot outflows at these redshifts and at these halo masses, the AGN-feedback leads to higher outflow velocities for the hot gas and this effect increases with increasing halo mass. In contrast, the radial velocity profiles of the Lyα emitting gas are not significantly altered by the inclusion of AGN-feedback, implying that the AGN-feedback, as implemented in the ENGINE (and EAGLE) simulations has little to no effect on the kinematics of the Lyα emitting gas. As we are only looking at the ENGINE simulations here (NoAGN and RECAL), the highest halo mass bins are only $10^{12.3}$ and $10^{12.6}$ $M_\odot$ at redshifts $z \sim 3.5$ and $z \sim 3$ due to the smaller box sizes of the NoAGN and RECAL simulations compared to the EAGLE Ref simulation box.

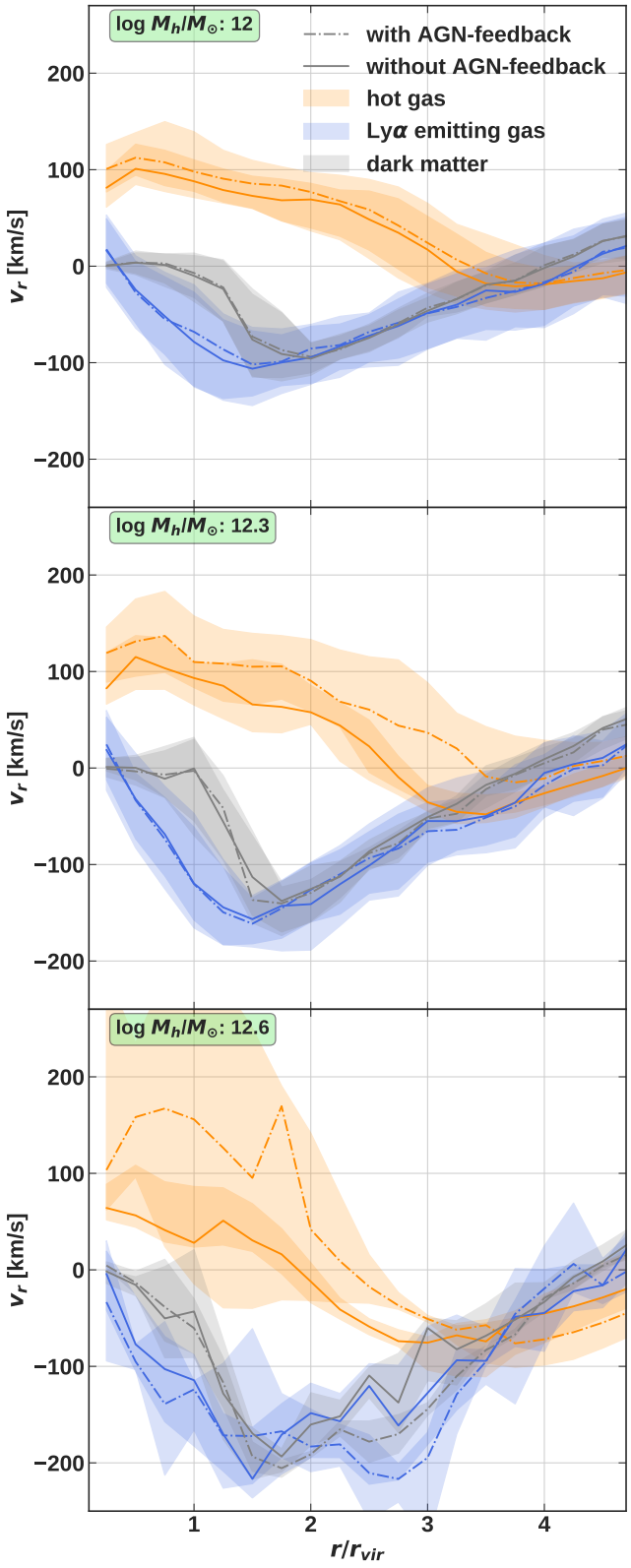

Figure D.5: Spherically averaged radial velocity profiles of the dark matter (grey), Lyα emitting gas (blue) and hot ($> 10^5 K$) gas (orange) with (dash-dotted line) and without (solid line) AGN-feedback at redshift $z \sim 3$.

E Number of detected LAEs compared to η

Here we compare the $\eta_{40-100}^{140-200}$'s with the number of detected LAEs in each field of the MAGG $z \sim 3.5$ sample, where $\eta_{40-100}^{140-200} < 1$. We exclude Ly$\alpha$ nebulae with $\eta_{40-100}^{140-200} > 1$ as this implies that the velocity dispersion of that nebulae increases with the distance to the centre of the halo, indicating superposition effects and not high halo masses, as already mentioned in Sections 2.2.4 & 2.3.2. We do not include the MAGG $z \sim 4.1$ sample in this analysis, as the number of LAEs detected decreases strongly with redshift, see Fossati et al. (2021) for a discussion on the causes for this. As can be seen in Figure E.6, the number of detected LAEs does increase slightly with the measured $\eta_{40-100}^{140-200}$ value of the individual Lyα nebulae.

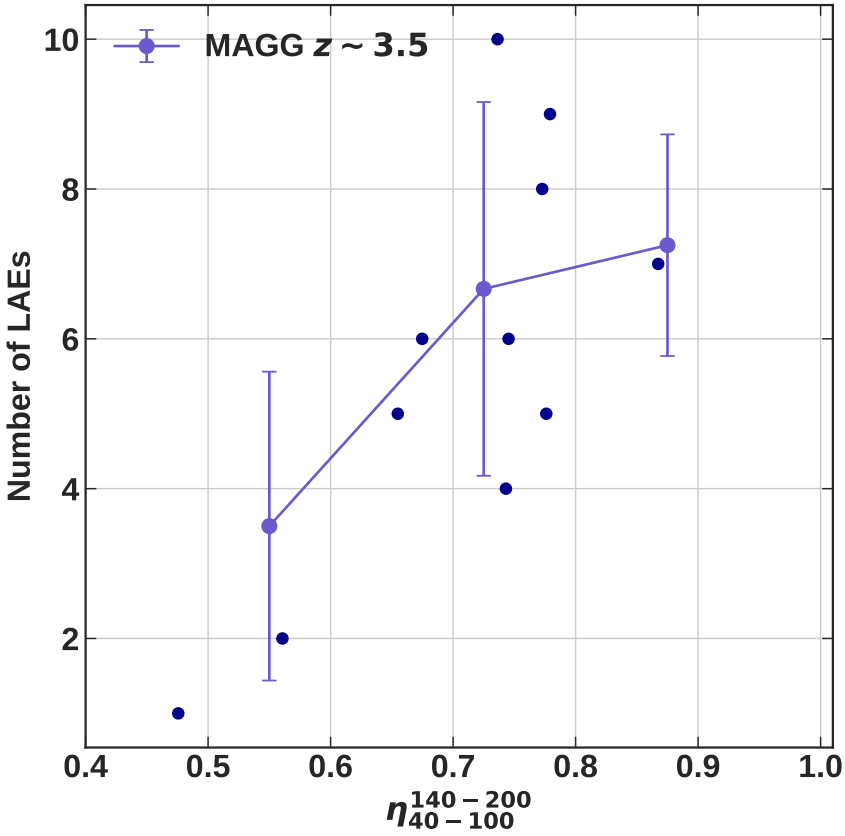

Figure E.6: The number of LAEs detected in the MUSE field of view for each Lyα nebulae in the MAGG $z \sim 3.5$ sample as a function of the nebulae's measured $\eta_{40-100}^{140-200}$. The dark blue points represent the individual nebulae and solid line with errorbars shows the median number of LAEs if the Lyα nebulae are binned in $\eta_{40-100}^{140-200}$.

F Effect of HOD on SB profiles

To asses how the mass range of halos hosting the Lyα nebulae affects the average SB profile of the nebulae, we compare the average SB profiles at $z \sim 3.5$ of three different halo mass distributions that are compatible with the kinematics of the observed Lyα nebulae. The standard halo mass range used throughout this work spans from $10^{12.03}$ $M_\odot$ to $10^{12.3}$ $M_\odot$ and is equivalent to assuming a tophat function centred on $10^{12.16\pm0.14}$ $M_\odot$ as the mass dependent probability function of a halo hosting a quasar. The average SB profile of simulated nebulae hosted by haloes within this mass range is plotted in green in Figure F.7. The average SB profile plotted in blue corresponds to a Gaussian probability function centred on $10^{12.16}$ $M_\odot$ with the standard deviation such that it coincides with $10^{12.03}$ $M_\odot$ and $10^{12.3}$ $M_\odot$. The third probability function which is compatible with observations is a step function which goes from zero to one at $10^{11.94}$ $M_\odot$. The corresponding average SB profile is plotted in yellow. The three average profiles do not systematically differ in any way, hence the the choice of probability function has no effect on the SB values and thus no effect on density constraints obtained from them.

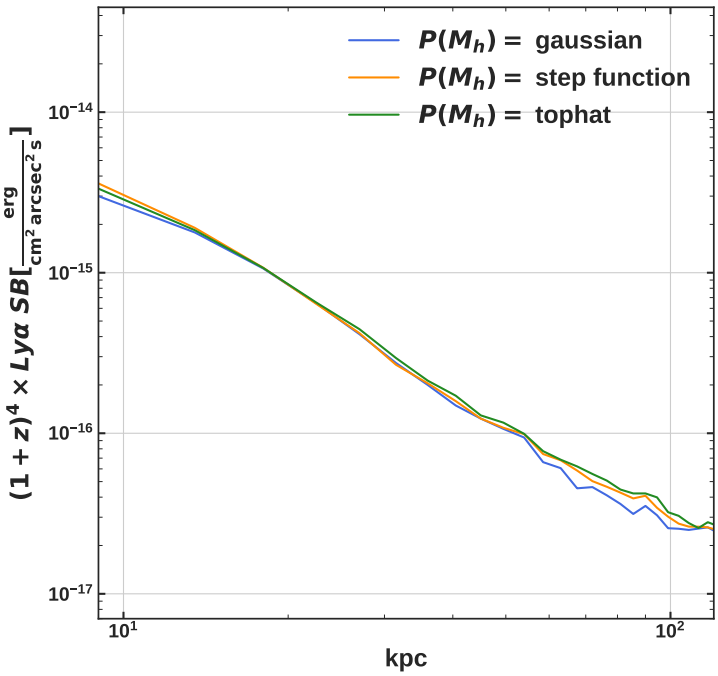

Figure F.7: The average SB profiles of Lyα nebulae hosted by haloes with mass ranges described by three different halo mass dependent probability functions. The average SB profile hosted by halos with a mass distribution described by a Gaussian centred on $10^{12.16\pm0.14}$ $M_\odot$ is plotted in blue, the average profile corresponding to a mass distribution described by a step function located at $10^{11.94}$ $M_\odot$ is plotted in yellow and that of a tophat function centred on $10^{12.16\pm0.14}$ $M_\odot$ is plotted in green.

G Effect of resolution on the SB profiles

To ensure that the density constraints obtained in Section 3.3.2 are not simply due to resolution effects, we compare the SB profiles of the Lyα nebulae analysed in this work at $z \sim 3$ to the SB profiles of Lyα nebulae in the higher resolution RECAL simulation. The subgrid physics implementation of the RECAL simulation is the same as that of the Ref EAGLE simulation used in this work (see **(alias?)** for details), with the relevant differences between the two simulations being their box sizes, 50 cMpc and 100 cMpc for the RECAL and Ref simulations respectively, and their mass resolution, where that of RECAL is higher by roughly a factor of eight. Figure G.8 reveals that increased resolution actually results in lower SB values, irrespective of the SF density threshold applied. This indicates that the SB values used in Section 3.3.2 are indeed upper limits and that comparing the observed Lyα nebulae to higher resolution simulations would not lead to a lower cold gas density estimate.

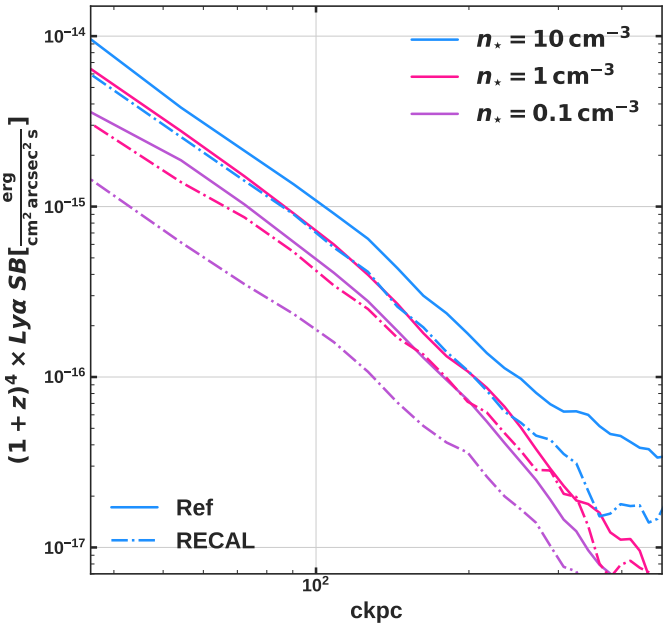

Figure G.8: The simulated Lyα SB profiles, corrected for redshift dimming, of the nebulae hosted by halos within the mass range $10^{12.03} - 10^{12.3}\mathrm{M}_\odot$ plotted with the different colours referring to the three SF density thresholds applied: $n_\star = 10\mathrm{cm}^{-3}$ (blue), $n_\star = 1\mathrm{cm}^{-3}$ (pink) and $n_\star = 0.1\mathrm{cm}^{-3}$ (purple). The SB profiles generated from the lower resolution Ref simulation are plotted with solid lines and those generated from the higher resolution RECAL simulation are plotted with dash dotted lines. The SB profiles of the Lyα nebulae generated from the higher resolution RECAL simulation are systematically lower, indicating the the SB values from the Ref simulation can safely be used as upper limits.

H Redshift evolution of the cold gas density

The simulated SB values evolve as SB $\propto (1+z)^{7.3}$, a rate higher than the theoretically expected SB $\propto (1+z)^5$. To verify that this deviation is caused by the cold gas density scaling at a rate higher than $n \propto (1+z)^3$ and not by a redshift evolution of the cold gas fraction and volume filling fraction we calculate the average cold gas density in the CGM of the haloes analysed in this work at $z \sim 3$, $z \sim 3.5$ and $z \sim 4$. As can be seen in Figure H.9, fitting reveals that the average cold gas density values scale as $n \propto (1+z)^{4.35}$, thereby confirming that the unexpectedly strong redshift scaling of the SB values is driven that of the cold gas.

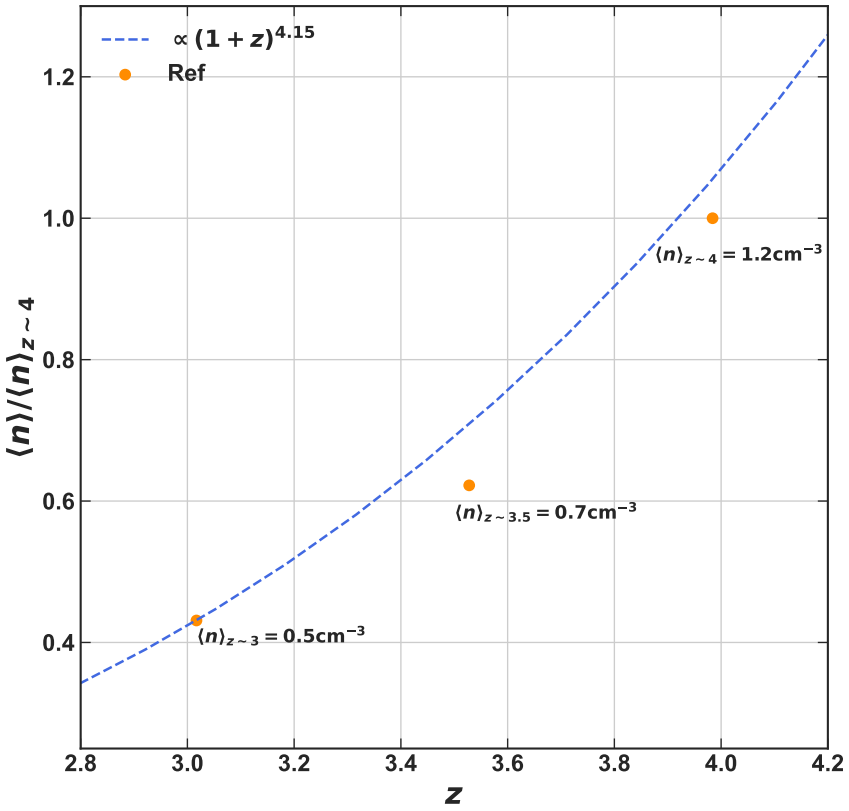

Figure H.9: The average cold gas density of the CGM of the haloes included in this analysis within the mass range $10^{12.03} - 10^{12.3}$ $M_\odot$ as a function of redshift. The average densities rescaled by that at $z \sim 4$ are indidcated with orange circles. The blue, dashed line indicates the best fit describing their redshift scaling.

I Density temperature diagram of the CGM

To asses whether the high density, cold gas clouds implied by the results in Section 3.3.2 are in pressure equilibrium with the hot CGM, it is necessary to obtain the typical densities and temperatures of said hot CGM. To this end, we generate the average density temperature diagram of the simulated CGM of the haloes within the mass range $10^{12.03} - 10^{12.3}$ $M_\odot$ at $z \sim 3.5$. For the purposes of this diagram, we define the CGM as beginning at a distance of 10 kpc from the halo centre and extending to the halo's virial radius. The density temperature diagram in Figure I.10, clearly shows the hot and cold phases of the CGM at $\sim 10^{6.5}$K and $\sim 10^{4.5}$ K respectively. The effective equation of state that the star forming gas is placed on in the EAGLE simulations is also apparent in the lower right quadrant of the plot.

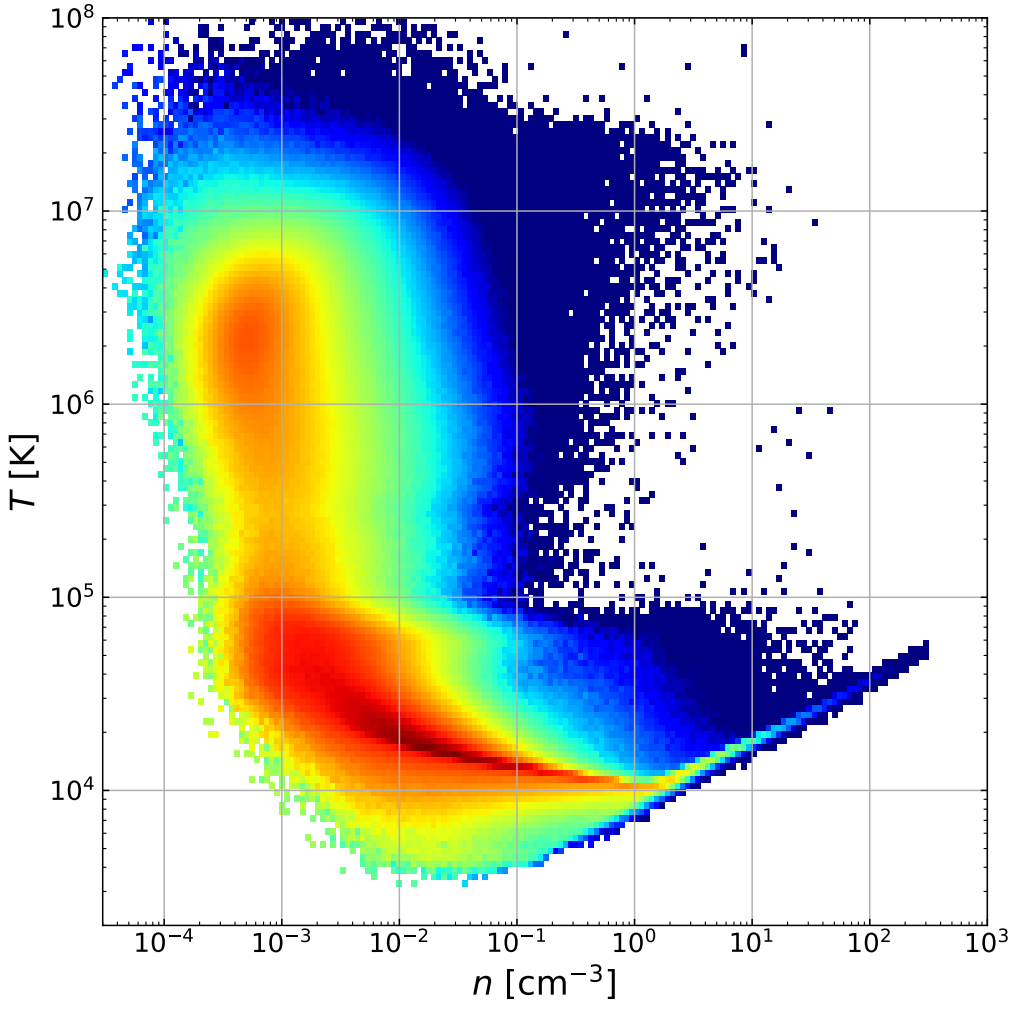

Figure I.10: Average density temperature diagram of the simulated CGM of the haloes within the mass range $10^{12.03} - 10^{12.3}$ $M_\odot$ at $z \sim 3.5$.

J Effect of the QSO opening angle on SB values

The mock observations analysed in this work are generated under the assumption of maximal fluorescence. This implies that the ionisation cone of the central quasar has an opening angle of 180°. Although the exact opening angle of high redshift, UV-bright quasars in currently still unknown, an angle of 180° is unlikely, making the simulated SB profile analysed in this work upper limits. To gauge the effect of the opening angle on the shape and values of the SB profiles, we generate mock observations for a range of opening angles and compare the resultant SB profiles in Figure J.11. For opening angles as low as 120°, the shape of the profiles remains almost unchanged and, while the SB values are lower, they are not significantly lower. For instance, the spread of SB values within a halo mass bin of ~ 0.3 dex, as shown in Figure 3.2, is comparable to the dimming caused by reducing the ionisation cone's angle by 60°. Opening angles below 90° lead to a slight steepening of the SB profile's shape and, as is to be expected, even lower SB values.

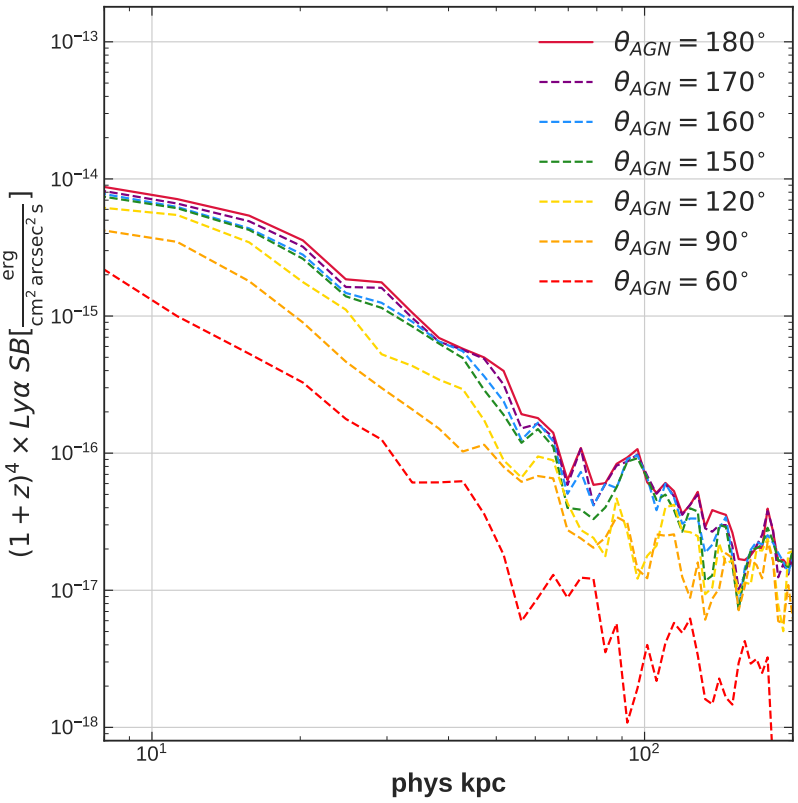

Figure J.11: The median SB profiles of Lyα nebulae hosted by haloes within the mass range $10^{12.03} - 10^{12.3}$ M$_\odot$ at $z \sim 3.5$, generated assuming a range of opening angles for the ionisation cones. The assumption of maximal fluorescence corresponds to an opening angle of 180° of the central quasar's ionisation cone. Unsurprisingly, lower opening angles result in lower SB values, but only opening angles below 90° result in a slight change of the SB profile's shape.

Publications

Published:

Resolving the physics of Quasar Lyα Nebulae (RePhyNe): I. Constraining Quasar host halo masses through Circumgalactic Medium kinematics
S. de Beer, S. Cantalupo, A. Travascio, G. Pezzulli, M. Galbiati, M. Fossati, M. Fumagalli, T. Lazeyras, A. Pensabene, T. Theuns, W. Wang
MNRAS, 526, 1850

Submitted:

ALMA survey of a massive node of the Cosmic Web at $z \sim 3$. I. Discovery of a large overdensity of CO emitters
A. Pensabene, S. Cantalupo, C. Cicone, R. Decarli, M. Galbiati, M. Ginolfi, S. de Beer, M. Fossati, M. Fumagalli, T. Lazeyras, G. Pezzulli, A. Travascio, W. Wang, J. Matthee, M. V. Maseda
eprint arXiv:2401.04765

To be submitted:

Resolving the physics of Quasar Lyα Nebulae (RePhyNe): II. High gas densities and turbulence are required to explain observed surface brightness levels at $z \geq 3$
S. de Beer, S. Cantalupo, A. Travascio, G. Pezzulli, M. Galbiati, M. Fossati, M. Fumagalli, T. Lazeyras, A. Pensabene, G. Quadri, T. Theuns, W. Wang

Bibliography

Adams M., et al., 2021, Technical Report LBNL-6616E, Chombo Software Package for AMR Applications - Design Document. Lawrence Berkeley National Laboratory

Agertz O., Teyssier R., Moore B., 2009, MNRAS, 397, L64

Aleksić J., et al., 2011, ApJ, 730, L8

Arnouts S., et al., 2007, A&A, 476, 137

Arrigoni Battaia F., Hennawi J. F., Prochaska J. X., Cantalupo S., 2015, ApJ, 809, 163

Arrigoni Battaia F., Hennawi J. F., Cantalupo S., Prochaska J. X., 2016, ApJ, 829, 3

Arrigoni Battaia F., Hennawi J. F., Prochaska J. X., Oñorbe J., Farina E. P., Cantalupo S., Lusso E., 2019a, MNRAS, 482, 3162

Arrigoni Battaia F., et al., 2019b, A&A, 631, A18

Augustin R., Péroux C., Hamanowicz A., Kulkarni V., Rahmani H., Zanella A., 2021, MNRAS, 505, 6195

Bacon R., et al., 2010, in McLean I. S., Ramsay S. K., Takami H., eds, Society of Photo-Optical Instrumentation Engineers (SPIE) Conference Series Vol. 7735, Ground-based and Airborne Instrumentation for Astronomy III. p. 773508, doi:10.1117/12.856027

Bacon R., et al., 2017, A&A, 608, A1

Bacon R., et al., 2021, A&A, 647, A107

Bahcall J. N., Salpeter E. E., 1965, ApJ, 142, 1677

Baldry I. K., Glazebrook K., Brinkmann J., Ivezić Ž., Lupton R. H., Nichol R. C., Szalay A. S., 2004, ApJ, 600, 681

Baldwin J. A., Burbidge E. M., Burbidge G. R., Hazard C., Robinson L. B., Wampler E. J., 1974, ApJ, 193, 513

Banerjee R., Vázquez-Semadeni E., Hennebelle P., Klessen R. S., 2009, MNRAS, 398, 1082

Basu S., Jones C. E., 2004, MNRAS, 347, L47

Basu S., Gil M., Auddy S., 2015, MNRAS, 449, 2413

Becker Tjus J., Hörbe M., Jaroschewski I., Reichherzer P., Rhode W., Schroller M., Schüssler F., 2022, Physics, 4, 473

Berezhko E. G., 2008, ApJ, 684, L69

Berger M. J., Oliger J., 1984, Journal of Computational Physics, 53, 484

Bertschinger E., 1985, ApJS, 58, 39

Bielby R., Crighton N. H. M., Fumagalli M., Morris S. L., Stott J. P., Tejos N., Cantalupo S., 2017, MNRAS, 468, 1373

Bigiel F., et al., 2011, ApJ, 730, L13

Birnboim Y., Dekel A., 2003, MNRAS, 345, 349

Blandford R., Meier D., Readhead A., 2019, ARA&A, 57, 467

Bolton J. S., Puchwein E., Sijacki D., Haehnelt M. G., Kim T.-S., Meiksin A., Regan J. A., Viel M., 2017, MNRAS, 464, 897

Bond J. R., Kofman L., Pogosyan D., 1996, Nature, 380, 603

Bordoloi R., et al., 2022, Nature, 606, 59

Borisova E., et al., 2016, ApJ, 831, 39

Brooks A. M., Governato F., Quinn T., Brook C. B., Wadsley J., 2009, ApJ, 694, 396

Buck T., Pfrommer C., Pakmor R., Grand R. J. J., Springel V., 2020, MNRAS, 497, 1712

Bunker A. J., Marleau F. R., Graham J. R., 1998, AJ, 116, 2086

Bunker A., Smith J., Spinrad H., Stern D., Warren S., 2003, Ap&SS, 284, 357

Butsky I. S., Fielding D. B., Hayward C. C., Hummels C. B., Quinn T. R., Werk J. K., 2020, ApJ, 903, 77

Cai Z., et al., 2017, ApJ, 837, 71

Cai Z., et al., 2018, ApJ, 861, L3

Cai Z., et al., 2019, ApJS, 245, 23

Cantalupo S., 2017, in Fox A., Davé R., eds, Astrophysics and Space Science Library Vol. 430, Gas Accretion onto Galaxies. p. 195 (arXiv:1612.00491), doi:10.1007/978-3-319-52512-9˙9

Cantalupo S., Porciani C., 2011, MNRAS, 411, 1678

Cantalupo S., Porciani C., Lilly S. J., Miniati F., 2005, ApJ, 628, 61

Cantalupo S., Porciani C., Lilly S. J., 2008, ApJ, 672, 48

Cantalupo S., Lilly S. J., Haehnelt M. G., 2012, MNRAS, 425, 1992

Cantalupo S., Arrigoni-Battaia F., Prochaska J. X., Hennawi J. F., Madau P., 2014, Nature, 506, 63

Cantalupo S., et al., 2019, MNRAS, 483, 5188

Carswell R. F., Strittmatter P. A., Williams R. E., Beaver E. A., Harms R., 1975, ApJ, 195, 269

Ceverino D., Klypin A., 2009, ApJ, 695, 292

Chen M. C., Chen H.-W., Gronke M., Rauch M., Broadhurst T., 2021, MNRAS, 504, 2629

Chen M. C., et al., 2023, MNRAS, 518, 2354

Childs H., et al., 2012, in , High Performance Visualization–Enabling Extreme-Scale Scientific Insight. pp 357–372, doi:10.1201/b12985

Churchill C. W., Nielsen N. M., Kacprzak G. G., Trujillo-Gomez S., 2013a, ApJ, 763, L42

Churchill C. W., Trujillo-Gomez S., Nielsen N. M., Kacprzak G. G., 2013b, ApJ, 779, 87

Cole S., et al., 2005, MNRAS, 362, 505

Coleman G., Carswell R. F., Strittmatter P. A., Williams R. E., Baldwin J., Robinson L. B., Wampler E. J., 1976, ApJ, 207, 1

Corlies L., Peeples M. S., Tumlinson J., O'Shea B. W., Lehner N., Howk J. C., O'Meara J. M., Smith B. D., 2020, ApJ, 896, 125

Costa T., Arrigoni Battaia F., Farina E. P., Keating L. C., Rosdahl J., Kimm T., 2022, MNRAS, 517, 1767

Crain R. A., Eke V. R., Frenk C. S., Jenkins A., McCarthy I. G., Navarro J. F., Pearce F. R., 2007, MNRAS, 377, 41

Crain R. A., et al., 2015, MNRAS, 450, 1937

Crighton N. H. M., Hennawi J. F., Simcoe R. A., Cooksey K. L., Murphy M. T., Fumagalli M., Prochaska J. X., Shanks T., 2015a, MNRAS, 446, 18

Crighton N. H. M., et al., 2015b, MNRAS, 452, 217

Daddi E., et al., 2010, ApJ, 713, 686

Daddi E., et al., 2021, A&A, 649, A78

Daddi E., et al., 2022, ApJ, 926, L21

Davé R., Thompson R., Hopkins P. F., 2016, MNRAS, 462, 3265

Davé R., Anglés-Alcázar D., Narayanan D., Li Q., Rafieferantsoa M. H., Appleby S., 2019, MNRAS, 486, 2827

Davies J. J., Pontzen A., Crain R. A., 2022, MNRAS, 515, 1430

Davies J. J., Pontzen A., Crain R. A., 2024, MNRAS, 527, 4705

Dawson K. S., et al., 2013, AJ, 145, 10

Dekel A., Birnboim Y., 2006, MNRAS, 368, 2

Dekel A., et al., 2009, Nature, 457, 451

Di Matteo T., Springel V., Hernquist L., 2005, Nature, 433, 604

Diemer B., Kravtsov A. V., 2014, ApJ, 789, 1

Dijkstra M., Haiman Z., Spaans M., 2006, ApJ, 649, 37

Drake A. B., Farina E. P., Neeleman M., Walter F., Venemans B., Banados E., Mazzucchelli C., Decarli R., 2019, ApJ, 881, 131

Drake A. B., et al., 2022, ApJ, 929, 86

Driver S. P., et al., 2011, MNRAS, 413, 971

Drory N., et al., 2009, ApJ, 707, 1595

Dutta R., et al., 2020, MNRAS, 499, 5022

Dutta R., et al., 2021, MNRAS, 508, 4573

EAGLE-Team 2017, The EAGLE simulations of galaxy formation: Public release of particle data (arXiv:1706.09899)

Eftekharzadeh S., et al., 2015, MNRAS, 453, 2779

Ellison S. L., Ibata R., Pettini M., Lewis G. F., Aracil B., Petitjean P., Srianand R., 2004, A&A, 414, 79

Ezhikode S. H., Gandhi P., Done C., Ward M., Dewangan G. C., Misra R., Philip N. S., 2017, MNRAS, 472, 3492

Fardal M. A., Katz N., Gardner J. P., Hernquist L., Weinberg D. H., Davé R., 2001, ApJ, 562, 605

Farina E. P., et al., 2017, ApJ, 848, 78

Farina E. P., et al., 2019, ApJ, 887, 196

Faucher-Giguère C.-A., Kereš D., Dijkstra M., Hernquist L., Zaldarriaga M., 2010, ApJ, 725, 633

Faucher-Giguère C.-A., Kereš D., Ma C.-P., 2011, MNRAS, 417, 2982

Ferland G. J., et al., 2013, Rev. Mex. Astron. Astrofis., 49, 137

Fernandez-Figueroa A., et al., 2022, MNRAS, 517, 2214

Field G. B., 1959, ApJ, 129, 525

Field G. B., 1965, ApJ, 142, 531

Fielding D. B., et al., 2020, ApJ, 903, 32

Fillmore J. A., Goldreich P., 1984, ApJ, 281, 1

Fischer T. C., Crenshaw D. M., Kraemer S. B., Schmitt H. R., 2013, ApJS, 209, 1

Font-Ribera A., et al., 2013, J. Cosmology Astropart. Phys., 2013, 018

Fossati M., et al., 2021, MNRAS, 503, 3044

Fumagalli M., O'Meara J. M., Prochaska J. X., Worseck G., 2013, ApJ, 775, 78

Fumagalli M., O'Meara J. M., Prochaska J. X., 2016, MNRAS, 455, 4100

Fumagalli M., et al., 2017, MNRAS, 471, 3686

Furlanetto S. R., Schaye J., Springel V., Hernquist L., 2003, ApJ, 599, L1

Furlanetto S. R., Schaye J., Springel V., Hernquist L., 2005, ApJ, 622, 7

Gallego S. G., et al., 2018, MNRAS, 475, 3854

García-Vergara C., Hennawi J. F., Barrientos L. F., Rix H.-W., 2017, ApJ, 848, 7

Genel S., et al., 2014, MNRAS, 445, 175

Genel S., et al., 2018, MNRAS, 474, 3976

Genzel R., et al., 2010, MNRAS, 407, 2091

Girichidis P., Naab T., Hanasz M., Walch S., 2018, MNRAS, 479, 3042

González Lobos V., et al., 2023, arXiv e-prints, p. arXiv:2308.15955

Gould A., Weinberg D. H., 1996, ApJ, 468, 462

Grcevich J., Putman M. E., 2009, ApJ, 696, 385

Gronke M., Bird S., 2017, ApJ, 835, 207

Gronke M., Oh S. P., 2018, MNRAS, 480, L111

Gronke M., Oh S. P., 2020, MNRAS, 492, 1970

Gronke M., Oh S. P., Ji S., Norman C., 2022, MNRAS, 511, 859

Gunn J. E., Gott J. Richard I., 1972, ApJ, 176, 1

Gunn J. E., Peterson B. A., 1965, ApJ, 142, 1633

Guo Y., et al., 2020, ApJ, 898, 26

Guzzo L., et al., 2014, A&A, 566, A108

Haiman Z., Rees M. J., 2001, ApJ, 556, 87

Haiman Z., Spaans M., Quataert E., 2000, ApJ, 537, L5

He W., et al., 2017, Publications of the Astronomical Society of Japan, 70

Hennawi J. F., Prochaska J. X., 2013, ApJ, 766, 58

Hennawi J. F., et al., 2006, ApJ, 651, 61

Hennawi J. F., Prochaska J. X., Cantalupo S., Arrigoni-Battaia F., 2015, Science, 348, 779

Hogan C. J., Weymann R. J., 1987, MNRAS, 225, 1P

Hopkins P. F., 2013, MNRAS, 428, 2840

Hopkins P. F., Kereš D., Oñorbe J., Faucher-Giguère C.-A., Quataert E., Murray N., Bullock J. S., 2014, MNRAS, 445, 581

Hopkins P. F., et al., 2018, MNRAS, 480, 800

Hopkins P. F., et al., 2020, MNRAS, 492, 3465

Howk J. C., Ribaudo J. S., Lehner N., Prochaska J. X., Chen H.-W., 2009, MNRAS, 396, 1875

Huchra J. P., et al., 2012, ApJS, 199, 26

Hui L., Gnedin N. Y., 1997, MNRAS, 292, 27

Hummels C. B., et al., 2019, ApJ, 882, 156

Huscher E., Oppenheimer B. D., Lonardi A., Crain R. A., Richings A. J., Schaye J., 2021, MNRAS, 500, 1476

Iapichino L., Schmidt W., Niemeyer J. C., Merklein J., 2011, MNRAS, 414, 2297

Jenkins A., et al., 1998, ApJ, 499, 20

Ji S., et al., 2020, MNRAS, 496, 4221

Jones D. H., et al., 2004, MNRAS, 355, 747

Joung M. R., Bryan G. L., Putman M. E., 2012a, ApJ, 745, 148

Joung M. R., Putman M. E., Bryan G. L., Fernández X., Peek J. E. G., 2012b, ApJ, 759, 137

Kauffmann G., et al., 2003, MNRAS, 341, 54

Kereš D., Katz N., Weinberg D. H., Davé R., 2005, MNRAS, 363, 2

Kereš D., Katz N., Fardal M., Davé R., Weinberg D. H., 2009, MNRAS, 395, 160

Kollmeier J. A., Zheng Z., Davé R., Gould A., Katz N., Miralda-Escudé J., Weinberg D. H., 2010, ApJ, 708, 1048

Kulier A., Padilla N., Schaye J., Crain R. A., Schaller M., Bower R. G., Theuns T., Paillas E., 2019, MNRAS, 482, 3261

Langen V., Cantalupo S., Steidel C. C., Chen Y., Pezzulli G., Gallego S. G., 2023, MNRAS, 519, 5099

Lau M. W., Prochaska J. X., Hennawi J. F., 2018, ApJ, 857, 126

Leclercq F., et al., 2017, A&A, 608, A8

Lehner N., Prochaska J. X., Kobulnicky H. A., Cooksey K. L., Howk J. C., Williger G. M., Cales S. L., 2009, ApJ, 694, 734

Leibler C. N., Cantalupo S., Holden B. P., Madau P., 2018, MNRAS, 480, 2094

Leroy A. K., et al., 2013, AJ, 146, 19

Li J., Shen Y., 2023, ApJ, 950, 122

Li M., Tonnesen S., 2020, ApJ, 898, 148

Liang C. J., Remming I., 2020, MNRAS, 491, 5056

Lochhaas C., Tumlinson J., O'Shea B. W., Peeples M. S., Smith B. D., Werk J. K., Augustin R., Simons R. C., 2021, ApJ, 922, 121

Lochhaas C., et al., 2023, ApJ, 948, 43

Lofthouse E. K., et al., 2020, MNRAS, 491, 2057

Lofthouse E. K., et al., 2023, MNRAS, 518, 305

Lopez S., et al., 2018, Nature, 554, 493

Lowenthal J. D., Hogan C. J., Leach R. W., Schmidt G. D., Foltz C. B., 1990, ApJ, 357, 3

Lusso E., Worseck G., Hennawi J. F., Prochaska J. X., Vignali C., Stern J., O'Meara J. M., 2015, MNRAS, 449, 4204

Mackenzie R., et al., 2021, MNRAS, 502, 494

Mandelker N., Padnos D., Dekel A., Birnboim Y., Burkert A., Krumholz M. R., Steinberg E., 2016, MNRAS, 463, 3921

Mandelker N., van Dokkum P. G., Brodie J. P., van den Bosch F. C., Ceverino D., 2018, ApJ, 861, 148

Mandelker N., Nagai D., Aung H., Dekel A., Padnos D., Birnboim Y., 2019a, MNRAS, 484, 1100

Mandelker N., van den Bosch F. C., Springel V., van de Voort F., 2019b, ApJ, 881, L20

Marino R. A., et al., 2018, ApJ, 859, 53

Marino R. A., et al., 2019, ApJ, 880, 47

Marri S., White S. D. M., 2003, MNRAS, 345, 561

Martin C., Moore A., Morrissey P., Matuszewski M., Rahman S., Adkins S., Epps H., 2010, in McLean I. S., Ramsay S. K., Takami H., eds, Society of Photo-Optical Instrumentation Engineers (SPIE) Conference Series Vol. 7735, Ground-based and Airborne Instrumentation for Astronomy III. p. 77350M, doi:10.1117/12.858227

Martin D. C., Chang D., Matuszewski M., Morrissey P., Rahman S., Moore A., Steidel C. C., 2014, ApJ, 786, 106

Martin D. C., et al., 2019, Nature Astronomy, 3, 822

Mathes N. L., Churchill C. W., Kacprzak G. G., Nielsen N. M., Trujillo-Gomez S., Charlton J., Muzahid S., 2014, ApJ, 792, 128

Matthews J. H., Bell A. R., Araudo A. T., Blundell K. M., 2019, in European Physical Journal Web of Conferences. p. 04002 (arXiv:1902.10382), doi:10.1051/epjconf/201921004002

McAlpine S., et al., 2016, Astronomy and Computing, 15, 72

McCarthy I. G., et al., 2010, MNRAS, 406, 822

McCarthy I. G., Schaye J., Bower R. G., Ponman T. J., Booth C. M., Dalla Vecchia C., Springel V., 2011, MNRAS, 412, 1965

McCourt M., O'Leary R. M., Madigan A.-M., Quataert E., 2015, MNRAS, 449, 2

McCourt M., Oh S. P., O'Leary R., Madigan A.-M., 2018, MNRAS, 473, 5407

Meiksin A. A., 2009, Reviews of Modern Physics, 81, 1405

Meiring J. D., Tripp T. M., Werk J. K., Howk J. C., Jenkins E. B., Prochaska J. X., Lehner N., Sembach K. R., 2013, ApJ, 767, 49

Mohapatra R., Federrath C., Sharma P., 2022, MNRAS, 514, 3139

Monier E. M., Turnshek D. A., Lupie O. L., 1998, ApJ, 496, 177

More S., Diemer B., Kravtsov A. V., 2015, ApJ, 810, 36

Morrissey P., et al., 2018, ApJ, 864, 93

Mortensen K., Keerthi Vasan G. C., Jones T., Faucher-Giguère C.-A., Sanders R. L., Ellis R. S., Leethochawalit N., Stark D. P., 2021, ApJ, 914, 92

Narayanan A., et al., 2011, ApJ, 730, 15

Narayanan A., Savage B. D., Wakker B. P., 2012, ApJ, 752, 65

Navarro J. F., Steinmetz M., 1997, ApJ, 478, 13

Navarro J. F., Frenk C. S., White S. D. M., 1996, ApJ, 462, 563

Navarro J. F., Frenk C. S., White S. D. M., 1997, ApJ, 490, 493

Nelson D., Genel S., Pillepich A., Vogelsberger M., Springel V., Hernquist L., 2016, MNRAS, 460, 2881

Nelson D., et al., 2020, MNRAS, 498, 2391

O'Sullivan D. B., Martin C., Matuszewski M., Hoadley K., Hamden E., Neill J. D., Lin Z., Parihar P., 2020, ApJ, 894, 3

Obreja A., Battaia F. A., Macciò A. V., Buck T., 2023, MNRAS,

Ocvirk P., Pichon C., Teyssier R., 2008, MNRAS, 390, 1326

Osterbrock D. E., Ferland G. J., 2006, Astrophysics of gaseous nebulae and active galactic nuclei

Owen E. R., Jin X., Wu K., Chan S., 2019, MNRAS, 484, 1645

Padnos D., Mandelker N., Birnboim Y., Dekel A., Krumholz M. R., Steinberg E., 2018, MNRAS, 477, 3293

Parrish I. J., McCourt M., Quataert E., Sharma P., 2012, MNRAS, 419, L29

Patrício V., et al., 2016, MNRAS, 456, 4191

Peacock J. A., et al., 2001, Nature, 410, 169

Pearce F. R., et al., 1999, ApJ, 521, L99

Peeples M. S., et al., 2019, ApJ, 873, 129

Penton S. V., Stocke J. T., Shull J. M., 2002, ApJ, 565, 720

Pezzulli G., Cantalupo S., 2019, MNRAS, 486, 1489

Pezzulli G., Fraternali F., Binney J., 2017, MNRAS, 467, 311

Pillepich A., et al., 2018, MNRAS, 473, 4077

Planck Collaboration et al., 2014, A&A, 571, A1

Pontzen A., Tremmel M., Roth N., Peiris H. V., Saintonge A., Volonteri M., Quinn T., Governato F., 2017, MNRAS, 465, 547

Prochaska J. X., Weiner B., Chen H. W., Mulchaey J., Cooksey K., 2011, ApJ, 740, 91

Prochaska J. X., et al., 2013, ApJ, 776, 136

Putman M. E., Zheng Y., Price-Whelan A. M., Grcevich J., Johnson A. C., Tollerud E., Peek J. E. G., 2021, ApJ, 913, 53

Rahmati A., Schaye J., Bower R. G., Crain R. A., Furlong M., Schaller M., Theuns T., 2015, MNRAS, 452, 2034

Ramesh R., Nelson D., 2023, arXiv e-prints, p. arXiv:2307.11143

Ramesh R., Nelson D., Pillepich A., 2023, MNRAS, 518, 5754

Rauch M., Sargent W. L. W., Barlow T. A., Carswell R. F., 2001, ApJ, 562, 76

Rauch M., et al., 2008, ApJ, 681, 856

Rees M. J., Ostriker J. P., 1977, MNRAS, 179, 541

Robinson T. G., Tadhunter C. N., Dyson J. E., 2002, MNRAS, 331, L13

Rosdahl J., Blaizot J., 2012, MNRAS, 423, 344

Ross N. P., et al., 2013, ApJ, 773, 14

Rubin K. H. R., Prochaska J. X., Koo D. C., Phillips A. C., Weiner B. J., 2010, ApJ, 712, 574

Rubin K. H. R., et al., 2018, ApJ, 859, 146

Rudie G. C., et al., 2012, ApJ, 750, 67

Sargent W. L. W., Young P. J., Boksenberg A., Tytler D., 1980, ApJS, 42, 41

Saro A., Borgani S., Tornatore L., Dolag K., Murante G., Biviano A., Calura F., Charlot S., 2006, MNRAS, 373, 397

Schaye J., et al., 2010, MNRAS, 402, 1536

Schaye J., et al., 2015, MNRAS, 446, 521

Schiminovich D., et al., 2010, MNRAS, 408, 919

Schmitt H. R., Kinney A. L., 1996, ApJ, 463, 498

Scoville N., et al., 2007, ApJS, 172, 150

Sharma P., Parrish I. J., Quataert E., 2010, ApJ, 720, 652

Shen Y., et al., 2007, AJ, 133, 2222

Shen Y., et al., 2009, ApJ, 697, 1656

Sijacki D., Springel V., Di Matteo T., Hernquist L., 2007, MNRAS, 380, 877

Silk J., 1977, ApJ, 211, 638

Silva M. B., Santos M. G., Gong Y., Cooray A., Bock J., 2013, ApJ, 763, 132

Silva M. B., Kooistra R., Zaroubi S., 2016, MNRAS, 462, 1961

Silva M., et al., 2018, MNRAS, 474, 3649

Smette A., Surdej J., Shaver P. A., Foltz C. B., Chaffee F. H., Weymann R. J., Williams R. E., Magain P., 1992, ApJ, 389, 39

Sorini D., Davé R., Anglés-Alcázar D., 2020, MNRAS, 499, 2760

Spitzer Lyman J., 1956, ApJ, 124, 20

Springel V., 2005, MNRAS, 364, 1105

Springel V., 2010, MNRAS, 401, 791

Springel V., Hernquist L., 2002, MNRAS, 333, 649

Springel V., Yoshida N., White S. D. M., 2001, New Astron., 6, 79

Springel V., et al., 2005, Nature, 435, 629

Springel V., Pakmor R., Zier O., Reinecke M., 2021, MNRAS, 506, 2871

Steidel C. C., Erb D. K., Shapley A. E., Pettini M., Reddy N., Bogosavljević M., Rudie G. C., Rakic O., 2010, ApJ, 717, 289

Steidel C. C., Bogosavljević M., Shapley A. E., Kollmeier J. A., Reddy N. A., Erb D. K., Pettini M., 2011, ApJ, 736, 160

Steidel C. C., et al., 2014, ApJ, 795, 165

Suresh J., Nelson D., Genel S., Rubin K. H. R., Hernquist L., 2019, MNRAS, 483, 4040

Tacconi L. J., et al., 2013, ApJ, 768, 74

Tang S., Wang Q. D., Lu Y., Mo H. J., 2009, MNRAS, 392, 77

Tejos N., et al., 2021, MNRAS, 507, 663

Teyssier R., Moore B., Martizzi D., Dubois Y., Mayer L., 2011, MNRAS, 414, 195

Timlin J. D., et al., 2018, ApJ, 859, 20

Tormen G., Bouchet F. R., White S. D. M., 1997, MNRAS, 286, 865

Trainor R. F., Steidel C. C., 2012, ApJ, 752, 39

Travascio A., et al., 2020, A&A, 635, A157

Tripp T. M., et al., 2011, Science, 334, 952

Tumlinson J., et al., 2011, Science, 334, 948

Tumlinson J., et al., 2013, ApJ, 777, 59

Turner M. L., Schaye J., Steidel C. C., Rudie G. C., Strom A. L., 2014, MNRAS, 445, 794

Umehata H., et al., 2019a, Science, 366, 97

Umehata H., et al., 2019b, Science, 366, 97

Vanzella E., et al., 2017, MNRAS, 465, 3803

Vazza F., Brunetti G., Kritsuk A., Wagner R., Gheller C., Norman M., 2009, A&A, 504, 33

Villar-Martín M., Binette L., Fosbury R. A. E., 1999, A&A, 346, 7

Vogelsberger M., et al., 2014a, MNRAS, 444, 1518

Vogelsberger M., et al., 2014b, Nature, 509, 177

Vossberg A.-C. E., Cantalupo S., Pezzulli G., 2019, MNRAS, 489, 2130

Wakker B. P., Savage B. D., 2009, ApJS, 182, 378

Wang L., Dutton A. A., Stinson G. S., Macciò A. V., Gutcke T., Kang X., 2017, MNRAS, 466, 4858

Weiner B. J., et al., 2009, ApJ, 692, 187

Wendland H., 1995, Advances in Computational Mathematics, 4, 389

Werk J. K., et al., 2014, ApJ, 792, 8

White S. D. M., Frenk C. S., 1991, ApJ, 379, 52

Wisotzki L., et al., 2016, A&A, 587, A98

Witstok J., Puchwein E., Kulkarni G., Smit R., Haehnelt M. G., 2021, A&A, 650, A98

Wright R. J., Lagos C. d. P., Power C., Correa C. A., 2021, MNRAS, 504, 5702

Yang Y., Zabludoff A., Tremonti C., Eisenstein D., Davé R., 2009, ApJ, 693, 1579

York D. G., et al., 2000, AJ, 120, 1579

Young P., Sargent W. L. W., Boksenberg A., 1982, ApJ, 252, 10

Zafar T., Popping A., Péroux C., 2013, A&A, 556, A140

Zahedy F. S., Chen H.-W., Rauch M., Wilson M. L., Zabludoff A., 2016, MNRAS, 458, 2423

Zahedy F. S., et al., 2021, MNRAS, 506, 877

Zeldovich I. B., Einasto J., Shandarin S. F., 1982, Nature, 300, 407

Zhang X.-G., 2023, MNRAS, 519, 4461

Zhang D., Davis S. W., Jiang Y.-F., Stone J. M., 2018, ApJ, 854, 110

Zwicky F., Herzog E., Wild P., Karpowicz M., Kowal C. T., 1961, Catalogue of galaxies and of clusters of galaxies, Vol. I

da Ângela J., et al., 2008, MNRAS, 383, 565

de Beer S., et al., 2023, MNRAS, 526, 1850

de Lapparent V., Geller M. J., Huchra J. P., 1986, ApJ, 302, L1

den Brok J. S., et al., 2020, MNRAS, 495, 1874

van de Voort F., Schaye J., Booth C. M., Haas M. R., Dalla Vecchia C., 2011a, MNRAS, 414, 2458

van de Voort F., Schaye J., Booth C. M., Dalla Vecchia C., 2011b, MNRAS, 415, 2782

Acknowledgements

The three years spent at Milano Bicocca have truly been an amazing opportunity and I would like to thank my supervisor Sebastiano Cantalupo for giving me the chance to work on such interesting research in a supportive and fun group environment. Sebastiano taught me how, with careful thought and consideration, an inordinate amount of information can be inferred from what, on the surface, seems to be not much to go on. I would also like the thank Gabriele Pezzulli for the many emails and conversations concerning the finer theoretical considerations of this work and for his patience and generosity when explaining these finer points to me. Each member of our group, namely Marta Galbiati, Titouan Lazeyras, Antonio Pensabene, Giada Quadri, Andrea Travascio and Weichen Wang offered help, support and made the three years spent in this group some of the most fun of my life, despite all our hard work. For this I would like to express my sincere and genuine thanks to them.

I would be remiss to not acknowledge all the love and support from my family, without which I would not be here today. I was always made to feel that my thoughts and opinions were worthwhile and that I could achieve anything I seriously pursued, apart from athletics and singing, which were just never going to be an option. Specifically, I would like to thank my mother for the steady supply of beskuit, my father for the many books and both of them for listening to me jabber on multiple times a week. Last, but certainly not least, I would like to thank my partner Leon for also listening to my jabbering, being there for me and for bringing humour to almost any situation.

List of activities

11/01/2021 - 05/03/2021	**Online workshop Fundamentals of Gaseous Halos** Kavli Institute for Theoretical Physics
04/2021 - 10/2021	**Co-supervisor of Master Thesis** "Constraining dark matter properties through Lyα emission from the IGM"
11/2021	**Python programming course** Attended lectures and obtained credits.
03/2022	**Open access - an introduction** Attended lectures and obtained credits.
04/2022	**Cosmology & fundamental physics** Attended lectures and obtained credits.
05/2022 - 02/2023	**Co-supervisor of Bachelor Thesis** "The kinematical alignment between galactic disks and accreting cold gas from cosmic web filaments"
12/09/2022 - 16/09/2022	**Conference "What matter(s) around galaxies 2022"** Attended conference and gave talk.
11/2022 - 04/2023	**Co-supervisor of Bachelor Thesis** "How does AGN feedback affect the balance of inflowing/outflowing gas in haloes?"
01/2023	**Literature review: How to make a good bibliography** Attended lectures and obtained credits.
20/03/2023 - 24/03/2023	**52nd Saas-Fee advanced course** The CGM across cosmic time: An observational and modelling challenge Attended and presented poster.

05/2023	**Accretion discs astrophysics** Attended lectures and obtained credits.
21/06/2023 - 23/06/2023	**Machine learning INFN Hackathon**
07/08/2023 - 11/08/2023	**2023 Santa Cruz Galaxy Workshop** Attended conference and gave talk.
14/08/2023 - 18/08/2023	Met with collaborators in Caltech & UC San Diego
09/2023	**Deep learning for physicists** Attended lectures and obtained credits.